Development of Rapid Methods for Relaxation Time Mapping and Motion Estimation Using Magnetic Resonance Imaging

Dissertation

zur Erlangung des Doktorgrades der Naturwissenschaften

der Fakultät Physik der Technischen Universität Dortmund

vorgelegt von

Syed Irtiza Ali Gilani

September 2008

Abstract

Recent technological developments in the field of magnetic resonance imaging have resulted in advanced techniques that can reduce the total time to acquire images. For applications such as relaxation time mapping, which enables improved visualisation of *in vivo* structures, rapid imaging techniques are highly desirable. TAPIR is a Look-Locker-based sequence for high-resolution, multislice T_1 relaxation time mapping. Despite the high accuracy and precision of TAPIR, an improvement in the *k*-space sampling trajectory is desired to acquire data in clinically acceptable times. In this thesis, a new trajectory, termed line-sharing, is introduced for TAPIR that can potentially reduce the acquisition time by 40 %. Additionally, the line-sharing method was compared with the GRAPPA parallel imaging method. These methods were employed to reconstruct time-point images from the data acquired on a 4T high-field MR research scanner. Multislice, multipoint *in vivo* results obtained using these methods are presented. Despite improvement in acquisition speed, through line-sharing, for example, motion remains a problem and artefact-free data cannot always be obtained. Therefore, in this thesis, a rapid technique is introduced to estimate in-plane motion. The presented technique is based on calculating the in-plane motion parameters, i.e., translation and rotation, by registering the low-resolution MR images. The rotation estimation method is based on the pseudo-polar FFT, where the Fourier domain is composed of frequencies that reside in an oversampled set of non-angularly, equi-spaced points. The essence of the method is that unlike other Fourier-based registration schemes, the employed approach does not require any interpolation to calculate the pseudo-polar FFT grid coordinates. Translation parameters are estimated by the phase correlation method. However, instead of two-dimensional analysis of the phase correlation matrix, a low complexity subspace identification of the phase correlation matrix is employed. This method is beneficial because it offers sub-pixel displacement estimation without interpolation, increased robustness to noise and limited computational complexity. Owing to all these advantages, the proposed technique is very suitable for the real-time implementation to solve the motion correction problem.

Acknowledgements

Finally, I would like to thank my parents and sisters for their encouragement throughout my educational period and especially while I was living abroad.

CONTENTS

LIST OF FIGURES

LIST OF TABLES

LIST OF ABBREVIATIONS

ACS	Auto-Calibration Signal
ADF	Angular Difference Function
BOLD	Blood Oxygenation Level Dependent
DTPA	Diethylenetriaminepentaacetic Acid
ETL	Echo Train Length
EPI	Echo Planar Imaging
FFT	Fast Fourier Transform
FLASH	Fast Low Angle Shot
fMRI	Functional Magnetic Resonance Imaging
FOV	Field-of-View
GRAPPA	Generalised Autocalibrating Partially Parallel Acquisitions
IE	Inversion Efficiency
IR	Inversion Recovery
LL	Look Locker
MRI	Magnetic Resonance Imaging
NMR	Nuclear Magnetic Resonance
PPFT	Pseudo-Polar Fourier Transform
ROI	Region-of-Interest
PROPELLER	Periodically Rotated Overlapping Parallel Lines with Enhanced Reconstruction
PSF	Point Spread Function
ROI	Region-of-Interest
SENSE	Sensitivity Encoding
SMASH	Simultaneous Acqusition of Spatial Harmonics
SNR	Signal-to-Noise Ratio
SOS	Sum-of-Squares
SR	Saturation Recovery
STE	Stimulated Echoes
SVD	Singular Value Decomposition
TAPIR	T_1 Mapping with Partial Inversion Recovery
TAPIR-IE	TAPIR Inversion Efficiency
TE	Time to Echo
TI	Time to Inversion
TR	Repetition Time

Chapter 1
Introduction

In 1973 a new technique emerged in the domain of nuclear magnetic resonance (NMR) applications and was termed magnetic resonance imaging (MRI). This magnetic field gradient enhanced NMR method enables the spatial localisation of resonating spins [1]. Numerous technological advancements make high quality MR images highly valuable for clinical diagnoses. The inherent non-invasiveness of MRI provides an edge over other state-of-the-art medical imaging modalities. Therefore, the clinical diagnostic method of choice nowadays is MRI when financial constraints do not play a determining role. In addition, the ability to directly manipulate MR image contrast through varying different physical properties of the resonating spins is extremely advantageous.

Signal intensity and contrast of MR images are dependent on several parameters. A change in each parameter produces a so-called "weighting" in the corresponding image. Hence, the influence of proton density, diffusion, spin-lattice relaxation and spin-spin relaxation can be observed in the weighted images through manipulation of the respective parameters.

The transverse relaxation rate, T_2, longitudinal relaxation rate, T_1, and the proton density, ρ, mainly determine the contrast in MR images. Specifically, the greater the differences in the T_1 and T_2 relaxation times, the higher the contrast in MR images. Thus, T_1-weighted images or T_2-weighted images can be obtained by properly selecting the MRI acquisition protocol parameters. Similarly, ρ-weighted images can be obtained by minimising T_1 and T_2 effects.

Optimisation of the MRI acquisition protocol parameters to generate the ideal weighting in the images is often limited by the acceptable acquisition times and the desired signal-to-noise ratio (SNR). In clinical practice, shorter acquisition times are

preferred and thus the T_2 weighting interferes with the T_1 weighting and vice-verse. Hence, conventional MRI generates contrast that is affected by complex mechanisms. This problem is solved if parametric maps of, for example, the proton density, the relaxation times, or the diffusion coefficients are reconstructed. A series of weighted images can be obtained followed by the data fitting to an appropriate signal model and thus a parametric map is reconstructed.

Brain imaging using MRI has become a valuable instrument for studying functional and structural relationships in the human brain. Image resolution enhancement through improved SNR and through advanced imaging hardware plays a central focus in modern MRI acquisition techniques. Various signal and contrast enhancement mechanisms have been employed in order to improve visualisation of different organs and tissues using MRI. In the following, first a modification to a rapid relaxation rate mapping method, known as TAPIR (T_1 mapping with Partial Inversion Recovery) [2], is introduced and after that a rapid method to detect motion occurring between different MR measurements is introduced.

1.1 Rapid Relaxation Rate Mapping

Measurement of the spin-lattice relaxation time constant, T_1, can provide important insights into pathological processes in the human brain such as multiple sclerosis or hepatic encephalopathy [3]. Acquisition times, however, tend to be long and therefore reductions through a time-efficient k-space sampling trajectory is desirable. Traditional techniques to perform T_1 mapping often suffer from disadvantages such as longer scan times, hardware imperfections and the need to acquire images with different inversion times. TAPIR, a Look-Locker based multislice, multishot sequence for rapid T_1 mapping is capable of *in vivo* quantification with high spatial resolution by interleaving the slices and time-points. TAPIR eliminates problems such as longer scan times and inadequate SNR. In particular, it eliminates dead times (times when no measurement is performed) and repetitive measurements with different inversion times are not required.

In this work a k-space sampling trajectory termed "line-sharing" is introduced to acquire T_1-weighted time-point images using the TAPIR sequence. In the proposed scheme, every other high-frequency k-space phase encode line of each time-point is skipped, but still preserving a complete central portion of k-space – the keyhole. Subsequent reconstruction of the images is preceded by interpolation of the corresponding high-frequency phase-encode lines acquired in the neighbouring time-points. That is, if image n is under consideration then phase encode lines from image n-1 and $n+1$ are interpolated to reconstruct the missing phase encode lines in image n. It is a well known fact that the bulk image intensity largely resides near the centre of k-space, whilst edge information is encoded in the periphery of k-space. In principle, the idea of line-sharing is based on sharing certain parts of the edge information between the time-points, whilst completely sampling the keyhole preserves the signal intensity. The objective of this work is to accelerate TAPIR using a multi-channel, line-sharing method which acquires sufficient k-space data for high quality T_1 mapping. Additionally, it is noted here that this method is generally applicable to relaxation time mapping.

Conventional parallel imaging methods such as GRAPPA (Generalised Autocalibrating Partially Parallel Acquisitions) [4], for example, provide another alternative to acquire the time-point images rapidly and reconstruct afterwards. Furthermore, given the acquisition of a keyhole, the line-sharing method is fully compatible with parallel imaging whereby a further reduction in the number of peripheral k-space lines could be achieved by using line-sharing and parallel imaging.

1.2 Rapid In-Plane Motion Estimation

Changes in blood flow, volume, oxygenation and other physiological factors are related to brain activity. fMRI (Functional MRI) is a state-of-the-art technique to measure brain activation non-invasively and it is based on the BOLD (Blood Oxygenation Level Dependent) contrast mechanism. EPI (Echo Planar Imaging) is the most common acquisition method to measure the BOLD signal and allows for a rapid sampling of the elicited response.

In order to satisfy some statistical constraints required for a robust detection of the BOLD signal, EPI measurements are repeated and therefore motion between different measurements can be a serious source of image artefacts. Hence, the correction of motion artefacts remains an important problem in MRI. In order to compensate for motion artefacts, accurate determination of the motion parameters is an essential prerequisite. Motion parameters can be determined from low-resolution images, termed navigator images that are coregistered. Several MRI acquisition methods employ spatial correlation techniques to coregister the navigator images. In this work, a new technique is proposed to estimate the in-plane motion parameters; this technique calculates rotation using the PPFT (Pseudo-Polar Fourier Transform) and translation using the phase correlation matrix of the navigator images. An angular difference function is defined as the integral of the difference function of navigator images in the pseudo-polar Fourier domain along the radial axis [5]. In particular, the applicability of an ADF (Angular Difference Function) for rotation estimation of navigator images is demonstrated. The significance of this method for MRI is that it does not require interpolation to calculate the pseudo-polar grid and it is fast. For in-plane translation estimation, an approach is suggested that uses dimensionality reduction of the two dimensional phase correlation matrix of the navigator images [6]. This rapid method affords substantial robustness to noise due to the use of the singular value decomposition (SVD) of the phase correlation matrix.

1.3 Scope and Structure of the Thesis

The focus of the work presented in this thesis is the application of new post-processing techniques to magnetic resonance images. Although these new techniques are rather different from the methodological point-of-view, they are linked by the common theme of 'rapid imaging techniques' and the requirement motion artefacts be adequately addressed therein.

Chapters 2 provide an introduction to the basic theoretical concepts of nuclear magnetic resonance and magnetic resonance imaging required for the understanding of the following chapters. In particular, the physical principles of nuclear magnetic

resonance and some pulse sequences are reviewed to provide a basis for understanding the imaging methods used in this thesis.

Chapter 3 is dedicated to techniques for rapid *in vivo* mapping of the longitudinal relaxation time, T_1, using TAPIR. Reconstruction of time-point images is performed through line-sharing, GRAPPA and line-shared-GRAPPA. In addition, the effects of line-sharing and GRAPPA on the optimisation of the number of time-points used for T_1 mapping has been analysed.

Chapter 4 describes the application of a state-of-the-art method for in-plane motion estimation. The chapter investigates the accuracy and precision of the method as applied to EPI images.

Chapter 5 demonstrates the phased-array processing methods applied to the multi-coil T_1-weighted time-point images to reconstruct T_1 maps using line-sharing. The emphasis here is placed on removing the possible ghost artefacts in the line-shared images in the case of shorter T_1 relaxation times.

Conclusions and discussions of future directions have been placed at the end of each thesis chapter. The overall "Outlook", Chapter 6, brings together the seemingly divergent topics presented in the thesis chapters; the ubiquity of motion artefacts also plagues rapid relaxation mapping methods. Furthermore, in view of the current trend towards higher static magnetic field in MRI, and the concomitant increase in absolute effect of motion artefacts at these higher fields, the relevance of the work presented here is briefly discussed for MRI at higher field strengths, for example, 9.4T.

1.4 References

1. Lauterbur PC. Image formation by induced local interactions: examples employing nuclear magnetic resonance. Nature 1973; 242;190–191.

2. Shah NJ, Zaitsev M, Steinhoff S, Zilles K. A new method for fast multislice T_1 mapping. NeuroImage 2001;14:1175–1185.

3. Shah NJ, Neeb H, Zaitsev M, Steinhoff S, Kircheis G, Amunts K, Häussinger D, Zilles K. Quantitative T_1 mapping of hepatic encephalopathy using magnetic resonance imaging. Hepatology 2003;38:1219–1226.

4. Griswold MA, Jakob PM, Heidemann RM, Nittka M, Jellus V, Wang J, Kiefer B, Haase A. Generalized autocalibrating partially parallel acquisitions. Magn Reson Med 2002;47: 1202–1210.

5. Keller Y, Shkolnisky Y, Averbuch A. The angular difference function and its application to image registration. IEEE Transactions On Pattern Analysis and Machine Intelligence 2005;27:969–976.

6. Hoge WS. A subspace identification extension to the phase correlation method. IEEE Transactions On Medical Imaging 2003;22:277–280.

Chapter 2
Physical Principles of MRI

Nuclear magnetic resonance is a physical phenomenon based upon quantum mechanical angular momentum, or spin, of the atomic nucleus. The description of NMR was first given by Isidor Rabi in 1938 [1]. Originally, NMR was used for molecular beams but in 1946 Felix Bloch [2] and Edward Purcell [3] developed NMR for liquids and solids. Nowadays, NMR is a manifold technique that is employed for the investigation of chemical composition and the molecular structure of proteins, for example.

The fundamental concepts of the NMR phenomenon and the physical principles of magnetic resonance imaging are reviewed in this chapter. Specifically, topics discussed in this chapter include the description of spin (a physical property of nuclear particles such as electrons, protons and neutrons) from the perspective of both classical and quantum mechanics, the classical Bloch equations, relaxation phenomenon, NMR signal formation, magnetisation evolution and spatial encoding, MR image formation and, finally, some basic MRI methods are described. The technical aspects elaborated here will serve as a basis for the understanding of subsequent chapters.

2.1 Nuclei in Magnetic Fields

In 1922, Stern and Gerlach [4] observed that the negatively charged electrons possess angular momentum, or spin. It was demonstrated that a beam of neutral silver atoms, passing through a perpendicular magnetic field, splits vertically into two beams, which implied a quantised aspect of angular momentum. In 1928, Dirac [5] described atomic nuclei on the basis of quantum mechanical theory and anticipated the property of intrinsic angular momentum, or spin. The phenomenon of NMR is based upon the

interaction of spin and magnetic field. Initially, methods to perform NMR experiments were based on sweeping the magnetic field to excite an extensive range of frequencies. Later, Ernst and Anderson [6] introduced the pulsed NMR technique in 1966.

MRI is an enhancement of NMR to visualize physical, chemical and biological substances. MRI of the human body is determined by the behaviour of specific nuclei to be imaged under the influence of magnetic fields. The water content of soft tissue in the human body is between approximately 60% and 80%. Thus, the hydrogen nucleus, a positively charged proton, is an abundant constituent of soft tissues in the human body and the most useful nuclei for MRI.

The classical and the quantum mechanical formalism of the nuclear spin are presented in the following sections. Although a precise and accurate description of NMR can only be given using a quantum mechanical model, the semi-classical model is sufficient for the description of modern MRI applications.

2.1.1 Classical Description of Spin

Spin is angular momentum intrinsic to a nuclear particle, e.g., proton. According to classical mechanics, a proton having spin can be conceptualized as a small charged body rotating around its own axis. Considering the motion of the charged body as a circular electric current loop, there is a magnetic field induced by such an electric current loop. According to the right hand rule, the induced magnetic field is directed along the axis of rotation. Therefore, the proton may be regarded as a dipole with a north and a south magnetic pole along its spin axis. A vector directed from the north to the south magnetic pole is called a magnetic dipole moment, denoted by μ; this is depicted in Figure 2.1. The magnetic dipole moment, or simply magnetic moment, provides a measure of the orientation and magnitude of the induced magnetic field.
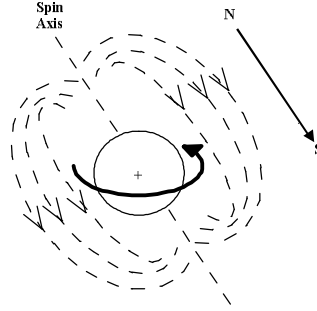
FIG. 2.1. A charged body spinning about its axis induces a magnetic field directed from the north to the south pole.

2.1.2 Quantum Mechanical Description of Spin

The description of spin on the grounds of the angular momentum of a classical rigid body is not adequate and, therefore, a spin operator, **I**, is used to describe the spin according to quantum mechanics. Let I_x, I_y and I_z be the three components of the spin operator **I** along x, y and z axes, respectively, and $\hbar$ is Plank's constant divided by 2π, and then the following relationships hold:

$$[I_z, I_x] = i\hbar I_y$$
$$[I_y, I_z] = i\hbar I_x \qquad (2.1)$$
$$[I_x, I_y] = i\hbar I_z$$

The non-commutative relationships given in equation (2.1) show that the individual components of the spin operator **I** cannot be measured simultaneously. Nonetheless, another operator $\mathbf{I}^2$ may be represented as:

$$\mathbf{I}^2 = I_x^2 + I_y^2 + I_z^2 \qquad (2.2)$$

This operator commutes with the components of **I**:

$$\left[\mathbf{I}^2, I_x\right] = \left[\mathbf{I}^2, I_y\right] = \left[\mathbf{I}^2, I_z\right] = 0 \qquad (2.3)$$

Thus, equation (2.3) implies that $\mathbf{I}^2$ and any of the components of $\mathbf{I}$ can be measured simultaneously. Conventionally, only the z component, I_z, is measured. According to the 'eigenvalue' formalism of quantum mechanics, the process of measuring the observables, such as $\mathbf{I}^2$ and I_z, can be denoted by:

$$\mathbf{I}^2\left|s_I\right\rangle = \hbar^2 I(I+1)\left|s_I\right\rangle \tag{2.4}$$

$$I_z\left|s_I\right\rangle = \hbar s_I\left|s_I\right\rangle \tag{2.5}$$

$$s_I = -I, -I+1, ..., I$$

where $\left|s_I\right\rangle$ are the eigenstates of $\mathbf{I}^2$ and I_z, $I(I+1)$ are the eigenvalues of $\mathbf{I}^2$ and s_I are the eigenvalues of I_z. I is a spin quantum number. The spin quantum number, I, can take only positive integer or half-integer values e.g., 0, 1/2, 1, 3/2, 2… I can be equal to 1/2, 3/2, 5/2 … if the atom has odd mass number; 1, 2, 3, 4… if the atom has even mass number but the atomic number is odd; and 0 if both the atomic number and the mass number are even.

Nuclei with a non-zero spin possess a magnetic dipole moment, $\boldsymbol{\mu}$. The relationship between the magnetic moment of a nucleus and its spin is:

$$\boldsymbol{\mu} = \gamma \hbar \mathbf{I} \tag{2.6}$$

where γ is a gyromagnetic ratio. The gyromagnetic ratio of a particle is the ratio of its magnetic moment to its angular momentum, given as:

$$\gamma = \frac{g\,e}{2m} \tag{2.7}$$

where e is a charge of electron, m is a mass of proton and g is a nuclear *Landé* factor. The *Landé* factor describes the difference between the nuclear magnetic moment and its angular momentum.

Consider a nucleus with a non-zero spin in a magnetic field **B**. The energy operator, E, for this simple system is given by:

$$E = -\boldsymbol{\mu} \cdot \mathbf{B} \tag{2.8}$$

where the magnetic field **B** is given by:

$$\mathbf{B} = B_0 \mathbf{k} \tag{2.9}$$

Hence, the potential energy of the magnetic moment in the spin-up state ($I = +1/2$) can be written as:

$$E = -\gamma \hbar B_0 I_z \tag{2.10}$$

The evolution of a quantum mechanical system is described by the linear time-dependent Schrödinger differential equation:

$$i\hbar \frac{\partial}{\partial t} \left| \Psi(\mathbf{r}, t) \right\rangle = H \left| \Psi(\mathbf{r}, t) \right\rangle \tag{2.11}$$

where H is the Hamiltonian operator (energy operator) and the state vector or wave function $\left| \Psi(\mathbf{r}, t) \right\rangle$ is time dependent. Assuming the Hamiltonian is time-independent, the related time-independent Schrödinger differential equation can be formulated as:

$$\left| \Psi(\mathbf{r}, t) \right\rangle = \left| \psi(\mathbf{r}) \right\rangle e^{-\frac{iEt}{\hbar}} \tag{2.12}$$

A time independent stationary form of the Schrödinger equation enables the energy levels of the quantum system to be found according to:

$$H \left| \psi(\mathbf{r}) \right\rangle = E \left| \psi(\mathbf{r}) \right\rangle \tag{2.13}$$

where E denotes the eigenvalues of the Hamiltonian operator and the time-independent part of the stationary states is represented by $|\psi(\mathbf{r})\rangle$. Assuming $\mathbf{B}_0$ is oriented along z-axis and using equation (2.10), the Hamiltonian operator can be written as:

$$H = -\gamma\hbar B_0 I_z \qquad (2.14)$$

It is evident from equation (2.14) that the Hamiltonian is proportional to the projection operator of the spin onto z-axis i.e., I_z. Therefore, the eigenvectors and eigenvalues of the Hamiltonian are proportional to those of I_z. Since I_z has $2I+1$ eigenvalues, $-I,-I+1,\ldots,I$, it follows that the allowed energy levels of the system are given by:

$$E_{s_I} = -\gamma\hbar B_0 I_z s_I \qquad (2.15)$$

where $s_I=-I,-I+1,\ldots,I$. equation (2.15) describes an energy level characteristic of a spin system composed of equidistant energy levels. In the absence of an externally applied magnetic field, the net magnetic moment is zero. When a strong static magnetic field is applied, the basis energy level is split into different non-degenrate sub-levels by the action of Hamiltonian as shown in Figure 2.2. In the case of $I=1/2$, the energy difference, ΔE, between two possible states is:

$$\Delta E = \gamma\hbar B_0 \qquad (2.16)$$

In an equilibrium state, the number of spins in different energy levels are slightly different. The difference is approximately 6 protons per million at room temperature. The exact ratio is given by the Boltzmann distribution:

$$\frac{N_-}{N_+} = e^{-\frac{\Delta E}{kT}} \qquad (2.17)$$

where N_- and N_+ are the number of spins in antiparallel and parallel states, respectively, k is the Boltzmann constant, T represents the temperature in Kelvin and ΔE is the energy difference.
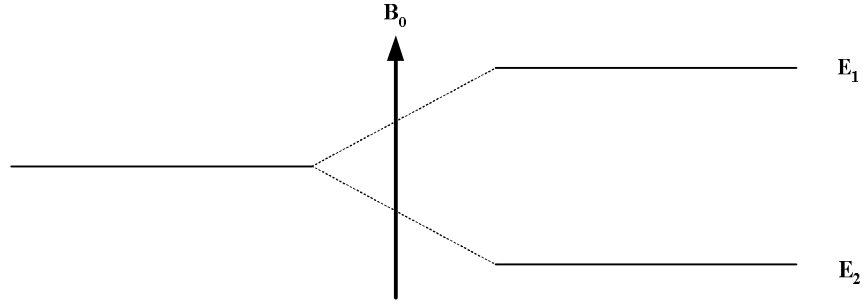
FIG. 2.2. Applying a magnetic field $\mathbf{B}_0$ creates different energy levels. For example, in the case of $I=1/2$, two energy levels are created, denoted as E_1 and E_2. Here, the basis energy level splits into two non-degenerate sub-levels. Each level corresponds to one of the two permitted values of s_I. For nuclei with $I>1/2$, the separation between successive levels is constant.

Each nucleus in an ensemble occupies a particular spin state. The ensemble can be described in terms of a linear combination of eigenstates as:

$$\left| \Psi(\mathbf{r},t) \right\rangle = \sum_{s_I=-I}^{I} C_{s_I} \left| s_I \right\rangle \tag{2.18}$$

where C_{s_I} represents the eigenvalues corresponding to the eigenstates $\left| s_I \right\rangle$. The time dependent average measured magnetic moment of the ensemble can be expressed as an expectation value of $\boldsymbol{\mu}$:

$$\left\langle \boldsymbol{\mu} \right\rangle = \left\langle \Psi(\mathbf{r},t) \left| \boldsymbol{\mu} \right| \Psi(\mathbf{r},t) \right\rangle = \gamma V \sum_{s_I=-I}^{I} \sum_{s_I'=-I}^{I} C_{s_I'}^* C_{s_I}^* \psi_{s_I'}^\dagger \mathbf{I} \, \psi_{s_I} e^{-\frac{i(E_{s_I'}-E_{s_I})t}{h}} \tag{2.19}$$

where V denotes the volume of the ensemble. For the case of a spin system with spin number equal 1/2, the expectation values of the magnetic moment components can be expressed as follows:

$$\langle \mu_x \rangle = \frac{1}{2}\hbar\gamma V \left(C^*_{+\frac{1}{2}}C_{-\frac{1}{2}}e^{-i\omega_0 t} + C^*_{-\frac{1}{2}}C_{+\frac{1}{2}}e^{i\omega_0 t} \right) = \hbar\gamma V \, \text{Re}\left(C^*_{-\frac{1}{2}}C_{+\frac{1}{2}}e^{-i\omega_0 t} \right)$$

$$\langle \mu_y \rangle = \frac{1}{2}\hbar\gamma V \left(-iC^*_{+\frac{1}{2}}C_{-\frac{1}{2}}e^{-i\omega_0 t} + iC^*_{-\frac{1}{2}}C_{+\frac{1}{2}}e^{i\omega_0 t} \right) = \hbar\gamma V \, \text{Re}\left(iC^*_{-\frac{1}{2}}C_{+\frac{1}{2}}e^{-i\omega_0 t} \right) \qquad (2.20)$$

$$\langle \mu_z \rangle = \frac{1}{2}\hbar\gamma V \left(C^*_{+\frac{1}{2}}C_{+\frac{1}{2}} - C^*_{-\frac{1}{2}}C_{-\frac{1}{2}} \right)$$

Considering the following assumptions:

$$C_{+\frac{1}{2}} = \frac{1}{\sqrt{V}}cos\beta \, e^{-i\delta_+}$$

$$C_{-\frac{1}{2}} = \frac{1}{\sqrt{V}}sin\beta \, e^{-i\delta_-} \qquad (2.21)$$

$$\delta_- - \delta_+ = \phi$$

$$\beta = \frac{\theta}{2}$$

Using equations (2.21), equation (2.20) can be re-written in the following form:

$$\langle \mu_x \rangle = \frac{1}{2}\hbar\gamma \sin\theta \cos(\phi - \omega_0 t)$$

$$\langle \mu_y \rangle = \frac{1}{2}\hbar\gamma \sin\theta \sin(\phi - \omega_0 t) \qquad (2.22)$$

$$\langle \mu_z \rangle = \frac{1}{2}\hbar\gamma \cos\theta$$

Although derived from the quantum mechanical basis, equation (2.22) is considered as a semi-classical description. It will be shown in section (2.2.1) that equation (2.22) leads to the similarity of the quantum mechanical expectation value of a spin under the influence of a time-dependent magnetic field and the magnetic moment precession under similar conditions in terms of classical mechanics.

2.2 Classical Description of Spin Dynamics

Significant concepts regarding the nuclear spin were established in the last section. The major aspect presented was the ability to describe the nuclear spin polarisation and precession within a semi-classical framework. According to the semi-classical formalism, the phenomenon of NMR is characterized by the motion of the magnetic moment vector. In an ensemble, each magnetic moment vector has a vertical component along the longitudinal direction and a horizontal component in the transverse plane. The vector sum of all horizontal components is zero and the vector sum of all vertical components is not zero due to excess spins in the spin-up state. Thus, the sum of these vertical components results in a single vector called the magnetisation vector, $\mathbf{M}$. Assuming the orientation of $\mathbf{M}$ is along $\mathbf{B}_0$, the magnetic dipole moment per unit volume V, or magnetisation vector $\mathbf{M}$, may be described as:

$$\mathbf{M} = \sum_V \mathbf{\mu} \tag{2.23}$$

An important distinction pertaining to the motion of the magnetisation vector, $\mathbf{M}$, includes the different dynamics of the component of $\mathbf{M}$ parallel to an applied magnetic field, and the component which is transverse to the field. The transverse component precesses at the Larmor frequency, while the longitudinal component undergoes relaxation to the equilibrium value (the details are explained in the next sections).

In this section, a mathematical formulation of spin dynamics and influence of the radiofrequency fields on the spin system are considered in turn, with attention to different frame of references.

2.2.1 The Bloch Equation

In 1946, Felix Bloch introduced a phenomenological equation, known as the Bloch equation, to describe the dynamic evolution of magnetisation in a spin ensemble. The Bloch equation may be written in vector form as:

$$\frac{d\mathbf{M}}{dt} = \mathbf{M} \times \gamma\mathbf{B} - \frac{(M_0 - M_z)\mathbf{k}}{T_1} - \frac{(M_x\mathbf{i} - M_y\mathbf{j})}{T_2} \tag{2.24}$$

where $\mathbf{i}$, $\mathbf{j}$, and $\mathbf{k}$ are unit vectors for x, y, and z axes respectively, M_x, M_y and M_z are components of the magnetisation vector $\mathbf{M}$, M_0 is an equilibrium magnetisation due to $\mathbf{B}_0$, $\mathbf{B}$ is a net magnetic field, T_1 is a longitudinal (spin-lattice) relaxation time constant and T_2 is a transverse (spin-spin) relaxation time constant. Ignoring the relaxation factors and integrating equation (2.24) results in the following set of equations:

$$M_x(t) = M_x(0)\cos\omega_0 t + M_y(0)\sin\omega_0 t$$
$$M_y(t) = -M_x(0)\sin\omega_0 t + M_y(0)\cos\omega_0 t \tag{2.25}$$
$$M_z(t) = M_z(0)$$

This set of equations is equivalent to equation (2.22) and provides the analogy between the quantum mechanical and semi-classical description of the magnetic moment precession through the Bloch equation.

2.2.2 Influence of Radiofrequency Fields on Spin Dynamics

A time-independent main magnetic field, $\mathbf{B}_0$, is usually aligned parallel to z-axis. A second magnetic field, $\mathbf{B}_1$, is applied to displace the magnetisation vector, $\mathbf{M}$, from the main magnetic field direction. The $\mathbf{B}_1$ field is at right angles to the $\mathbf{B}_0$ field and it rotates about $\mathbf{B}_0$ at frequency ω_0.

In the laboratory frame of reference, the circularly polarized radiofrequency $\mathbf{B}_1$ field is time-dependent and can be represented as:

$$\mathbf{B}_1(t) = B_1(t)\cos\omega_0 t\ \mathbf{i} - B_1(t)\sin\omega_0 t\ \mathbf{j} \tag{2.26}$$

The combined effect of the static and circularly polarized fields can be represented as:

$$\mathbf{B}_1(t) = B_1(t)\cos\omega_0 t\ \mathbf{i} - B_1(t)\sin\omega_0 t\ \mathbf{j} + B_0\ \mathbf{k} \tag{2.27}$$

The transition of the spins from the equilibrium state to non-equilibrium state following the radiofrequency pulse is called excitation. Excited spin system absorbs energy and there are more spins excited to the higher energy state than spins going to the lower energy state. The observed NMR signal corresponds to the energy of the emitted photons as the spins go from the higher to lower energy state.

It is known that the spins transit from the lower energy state to the higher energy state by absorption of a photon. The energy of the absorbed photon must precisely match the energy difference between the lower and higher energy states. Since the energy of a photon is related to its frequency, thus only a photon with the specific frequency (known as Larmor frequency) can cause transition of the spin to the higher energy state. Therefore, the energy of the radiofrequency pulse, hf, is given by:

$$hf = \gamma \hbar B_0 \tag{2.28}$$

It is to be noted from equation (2.28) that in order to cause resonance, the necessary condition is that the frequency of the applied radiofrequency pulse, f, should be equal to the Larmor precessional frequency of spins, ω_0, in the main magnetic field.

A rotating frame of reference is formed when the transverse plane of the laboratory frame of reference rotates about z-axis with an angular frequency, for instance, denoted as ω_{rf}. The $\mathbf{B}_1$ field can be represented in the rotating frame of reference according to the following relation:

$$\begin{bmatrix} B_{1x}'(t) \\ B_{1y}'(t) \\ B_{1z}'(t) \end{bmatrix} = \begin{bmatrix} \cos\omega_{rf}t & -\sin\omega_{rf}t & 0 \\ \sin\omega_{rf}t & \cos\omega_{rf}t & 0 \\ 0 & 0 & 1 \end{bmatrix} \begin{bmatrix} B_1(t)\cos\omega_0 t \\ -B_1(t)\sin\omega_0 t \\ 0 \end{bmatrix} \tag{2.29}$$

where $B_{1x}'(t)$, $B_{1y}'(t)$ and $B_{1z}'(t)$ are the components of $\mathbf{B}_1$ field along x, y and z axes, respectively, in the rotating frame of reference and ω_0 is the Larmor frequency. The on-resonance condition implies that the angular frequency of the rotating frame of

reference equals the carrier frequency of the $\mathbf{B}_1$ field, i.e., $\omega_{rf} = \omega_0$, therefore, the equation (2.29) becomes:

$$\begin{bmatrix} B'_{1x}(t) \\ B'_{1y}(t) \\ B'_{1z}(t) \end{bmatrix} = \begin{bmatrix} B_1(t) \\ 0 \\ 0 \end{bmatrix} \qquad (2.30)$$

The magnetisation vector, $\mathbf{M}$, in the laboratory frame of reference, spirals down in the transverse plane and in the rotating frame of reference, an equivalent magnetisation vector, $\mathbf{M_r}$, tips down in the transverse plane, as illustrated in Figure 2.3. An angle, α, known as flip angle, by which $\mathbf{M_r}$ tips in a particular direction is equal to the time integral of the angular frequency, ω_{rf}, over the radiofrequency pulse duration. Ignoring relaxation and diffusion factors, the Bloch equation in the laboratory frame of reference can be represented as:

$$\frac{d\mathbf{M}}{dt} = \mathbf{M} \times \gamma \left(B_1(t) \cos \omega_0 t \; \mathbf{i} - B_1(t) \sin \omega_0 t \; \mathbf{j} + B_0 \; \mathbf{k} \right) \qquad (2.31)$$

Using equation (2.29), the Bloch equation transforms to:

$$\frac{d\mathbf{M_r}}{dt} = \mathbf{M_r} \times \gamma \left(B_1(t) \cos(\omega_{rf} - \omega_0)t \; \mathbf{i}' - B_1(t) \sin(\omega_{rf} - \omega_0)t \; \mathbf{j}' + (B_0 - \frac{\omega_0}{\gamma}) \mathbf{k}' \right) \qquad (2.32)$$

where $\mathbf{i}'$, $\mathbf{j}'$, and $\mathbf{k}'$ are unit vectors in the rotating frame of reference, the effective magnetic field is represented inside the brackets and $\mathbf{M_r}$ precesses about the effective magnetic field in the rotating frame of reference.

(a)   **(b)**
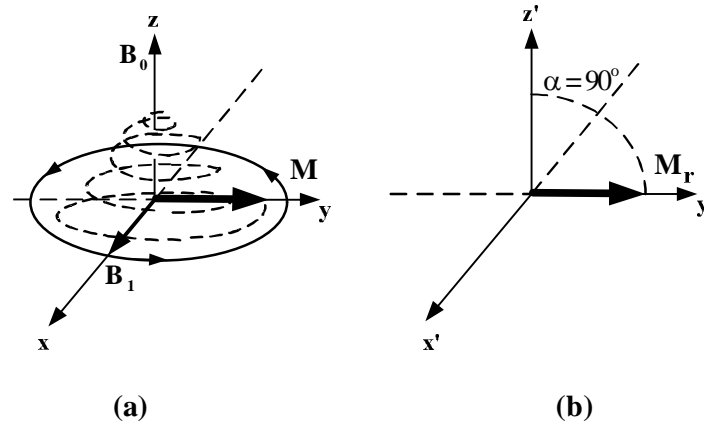
FIG. 2.3. An effect of 90° radiofrequency field, perpendicular to the main magnetic field $\mathbf{B}_0$, applied to a spin system. **(a)**: Visualization in the laboratory frame of reference. **(b)**: Visualization in the rotating frame of reference.

2.2.3 Spin Lattice Relaxation

After excitation, the system of spins returns to its equilibrium by emitting the absorbed energy as the spins return to the lower energy state. This phenomenon of returning to equilibrium is called relaxation. During relaxation, energy exchange occurs between the spins and the surrounding tissue, i.e., "lattice". The result is the exponential recovery of the longitudinal magnetisation, M_z, to the equilibrium magnetisation, M_0. This process, termed spin-lattice relaxation, is denoted using a time constant T_1. The behaviour of M_z is modelled by a term of the Bloch equation:

$$\frac{dM_z}{dt} = -\frac{(M_z - M_0)}{T_1} \tag{2.33}$$

The solution to this equation can be given as:

$$M_z(t) = M_0 - \left(M_0 - M_z(0)\right)e^{-\frac{t}{T_1}} \tag{2.34}$$

This solution describes the exponential recovery of M_z from the perturbed value $M_z(0)$ to the equilibrium value M_0 with the time constant T_1. The spin-lattice relaxation

mechanism is depicted in Figure 2.4. Longitudinal magnetisation recovery can be classified into two types: saturation recovery (SR) and inversion recovery (IR).

The evolution of longitudinal magnetisation in response to a saturation pulse, i.e., a 90° radiofrequency pulse followed by spoiling of the transverse magnetisation, is given by:

$$M_z(t) = M_0 \left(1 - e^{-\frac{t}{T_1}} \right) \tag{2.35}$$

Ideally, the resultant longitudinal magnetisation is zero after applying a 90° pulse because it tips the total magnetisation vector, **M**, into the transverse plane.

Inverted longitudinal magnetisation by an inversion pulse, i.e., 180° radiofrequency pulse, evolves according to:

$$M_z(t) = M_0 \left(1 - 2e^{-\frac{t}{T_1}} \right) \tag{2.36}$$

After longitudinal magnetisation inversion by the 180° pulse, the longitudinal magnetisation recovers during a time delay called inversion recovery time. Then a 90° pulse rotates the recovered magnetisation in the transverse plane and the resulting NMR signal is sampled. The inversion time is a crucial factor in determining the limits of the longitudinal magnetisation relaxation. A long inversion time allows the magnetisation to recover more towards the equilibrium value.
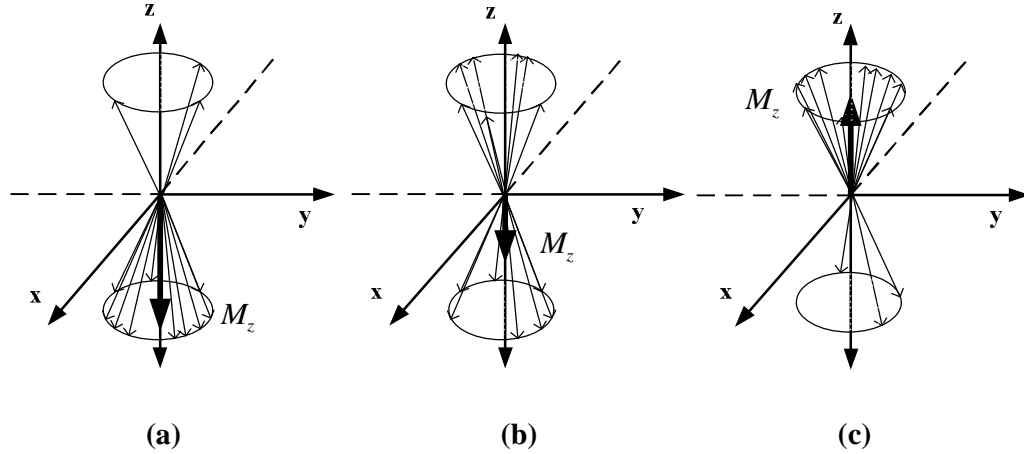
FIG. 2.4. Inversion recovery of the net longitudinal magnetisation vector, M_z, along z-axis. **(a)**: An inversion radiofrequency pulse excites all excess spin-up dipoles into spin-down state. The vectors along z-axis represent the spin-down dipoles. A few vectors in spin-up state depict quantum mechanical phenomenon and imperfection of the radiofrequency pulse. **(b)**: Relaxation of the spins to the spin-up state. **(c)**: Most of the spins have relaxed to the spin-up state.

2.2.4 Spin-Spin Relaxation

In an ensemble of spins, the cumulative magnetic field experienced by a spin is affected by the individual magnetic fields of the other spins. The field experienced by a spin is enhanced resulting in rapid precession if the magnetic fields of the surrounding spins are directed along $\mathbf{B}_0$. Hence, the net magnetisation decays away due to an augmentive phase loss among the spins. This process is termed spin-spin relaxation, T_2, and is illustrated in Figure 2.5.

A term of the Bloch equation describing the spin-spin relaxation is given as:

$$\frac{d\mathbf{M}_{xy}}{dt} = -\frac{\mathbf{M}_{xy}}{T_2} \tag{2.37}$$

where $\mathbf{M}_{xy} = M_x\mathbf{i} + M_y\mathbf{j}$ and T_2 is a spin-spin relaxation constant. During spin-spin relaxation, the phase coherent state of the spins following excitation is annihilated. The resulting exponential behaviour of the decaying transverse magnetisation can be described as a solution to equation (2.37):

$$\mathbf{M}_{xy}(t) = \mathbf{M}_{xy}(0)\, e^{-\frac{t}{T_2}} \qquad (2.38)$$

The actual time constant, T_2^*, with which the transverse magnetisation decays, is significantly shorter than the spin-spin relaxation time constant T_2. There is additional spin dephasing due to local magnetic field inhomogenities at the nucleus. The probable causes of such field inhomogenities are magnetic field gradients arising from boundaries between tissues with different magnetic susceptibilities, manufacturing imperfections, and metal in the sample. It results in different precessional frequencies of the spins and therefore the net transverse magnetisation decays away rapidly. The net transverse relaxation time constant, T_2^*, can be expressed as:

$$\frac{1}{T_2^*} = \frac{1}{T_2} + \frac{1}{T_2'} \qquad (2.39)$$

where T_2' is the time constant due to additional spin dephasing.

(a)   **(b)**   **(c)**
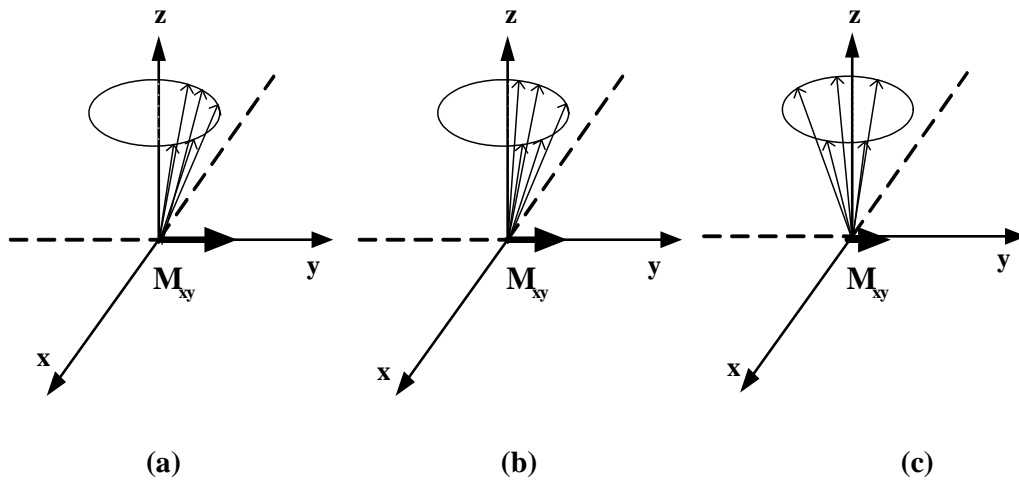
FIG. 2.5. The transverse magnetisation relaxation process depicted following a 90° radiofrequency pulse. Only the spin-up dipoles are illustrated. **(a)**: The precessing spins are initially phase coherent. $\mathbf{M}_{xy}$ is the net transverse magnetisation. **(b)**: Random variations in the precessional frequencies of the spins cause dephasing between them. Thereafter, the magnitude of $\mathbf{M}_{xy}$ is reduced compared to its value following the radiofrequency pulse. **(c)**: Further reduction in magnitude of $\mathbf{M}_{xy}$ due to dephasing process.

2.3 FID Signal

Following a 90° radiofrequency pulse, the net transverse magnetisation vector, $\mathbf{M_{xy}}$, precesses about $\mathbf{B}_0$ at the Larmor frequency. Faraday's law states that a time-varying magnetic field will induce a voltage in a coil placed perpendicular to the direction of the magnetic field. Mathematically, it may be represented as:

$$S = -\frac{\partial}{\partial t}\Phi(t) \tag{2.40}$$

where S is the induced voltage and $\Phi(t)$ is the magnetic flux. Therefore, $\mathbf{M_{xy}}$ induces an alternating voltage in a receiving radiofrequency coil and the receiver coil is designed to detect the changing flux in the transverse direction. The principle of reciprocity dictates that if a unit current flows in the coil, it will produce a magnetic field $\mathbf{B}_{1r}(\mathbf{r})$ and, in the opposite direction, a field $\mathbf{B}_{1r}(\mathbf{r})$ will induce a unit current in the coil. The total magnetic flux through the coil is then given by:

$$\Phi(t) = \int \mathbf{B}_{1r}(\mathbf{r}).\mathbf{M}(\mathbf{r},t)\, d\mathbf{r} \tag{2.41}$$

Since the plane of the coil is parallel to the z component of the magnetization, M_z can be ignored. Hence, the magnitude of the induced voltage, S, depends on the precessional frequency ω_0, the magnitude of $\mathbf{M_{xy}}$, transverse receive magnetic field $\mathbf{B}_{1r}$ and the sample volume, V:

$$S \propto \int_V \frac{\partial}{\partial t}\left(\mathbf{B}_{1r}(\mathbf{r}).\mathbf{M}(\mathbf{r},t)\right) d\mathbf{r} \propto \mathbf{M_{xy}}\, \gamma B_0\, e^{-\frac{t}{T_2}} \cos(\omega_0 t + \phi\,) \tag{2.42}$$

where $\mathbf{M_{xy}}$ is the net transverse magnetisation in complex notation, i.e., $\mathbf{M_{xy}} = M_x + i\, M_y$, $\mathbf{B}_{1r}$ is the magnetic field produced at spatial position $\mathbf{r}$ per unit current in the coil directed in the transverse direction and ϕ is an angle of orientation of the receiving radiofrequency coil. The received signal is in the form of a decaying exponential modulated with the Larmor frequency, ω_0. This signal can be demodulated in frequency

by ω_0 using the phase-sensitive detection method. The phase sensitive detection transforms the signal into a rotating frame of reference. Such a method can be employed using quadrature radiofrequency coils to improve sensitivity. Such coils are sensitive to the time-dependent magnetic fields along x and y axes. The real channel samples the signal component that is in-phase with a reference signal. The imaginary channel samples the signal component which is 90° out of phase with another reference signal. Both reference signals oscillate with the Larmor frequency but are offset in phase by 90° relative to each other. The resulting samples of the signal are considered as the real and imaginary components. The SNR of the signal is improved by $\sqrt{2}$ in the case quadrature coils are used.

2.4 Spatial Encoding of Magnetisation

MRI is a primary modality to image the structure of an underlying sample based upon the principles of NMR signal formation. This technique was invented, independently, by Lauterbur [7] and Mansfield [8] in 1973. The emitted NMR radiofrequency signal is influenced by the application of magnetic gradient fields and thus information to produce an MR image is obtained. The interplay between the static and gradient magnetic fields paves the way to distinguish NMR signals commencing from different spatial locations within a sample.

This section includes the description of gradient fields generating a range of resonant frequencies, the k-space formalism, slice selection and phase encoding mechanisms and finally the MRI signal formation is given.

2.4.1 Magnetic Field Gradients

Generally, a magnetic field gradient can be expressed in the form of a vector:

$$\mathbf{G} = G_x\mathbf{i} + G_y\mathbf{j} + G_z\mathbf{k} \qquad (2.43)$$

A static gradient is a nonuniform magnetic field, which is in the same direction as the main magnetic field but with amplitude that varies with position. For example, a z gradient, G_z, is the slope in the z direction of the z component of the applied field:

$$G_z = \frac{dB_z}{dz} \tag{2.44}$$

After applying a gradient in some direction, for instance the z direction, variation in the angular frequency of the spins can be described as:

$$\omega(z) = \gamma(B_0 + G_z z) \tag{2.45}$$

This equation emphasizes the linear relationship between the positions of the spins along z-axis and their Larmor frequencies following the application of gradient G_z.

A resultant magnetic field, $\mathbf{B}(\mathbf{r})$, is a gradient having a slope in a direction dependent on the relative amplitudes of G_x, G_y and G_z. The resultant field can be represented as:

$$\mathbf{B}(\mathbf{r}) = (B_0 + G_x x + G_y y + G_z z)\mathbf{k} \tag{2.46}$$
$$\mathbf{B}(\mathbf{r}) = (B_0 + \mathbf{G} \cdot \mathbf{r})\mathbf{k}$$

Similarly, a time-varying resultant magnetic field can be given by:

$$\mathbf{B}(\mathbf{r},t) = (B_0 + \mathbf{G}(t) \cdot \mathbf{r})\mathbf{k} \tag{2.47}$$

The space- and time-dependent phase accumulated due to the applied gradient after an initial radiofrequency pulse is:

$$\phi(\mathbf{r},t) = \int_0^t \omega(\mathbf{r},\tau)\,d\tau$$
$$= \gamma E(\mathbf{r})t + \omega_c + \gamma \int_0^t \mathbf{G}(\tau) \cdot \mathbf{r}\,d\tau \tag{2.48}$$

The first two terms in the summation given in equation (2.48) correspond to the constant phase accumulation with time from the inhomogeneity and the chemical shift, respectively, while the third term is the phase accumulated due to the applied gradient.

2.4.2 *k*-Space

The acquired MR signal is the 1D Fourier transform of the projection of the 2D magnetisation weighted with a phase encoding factor along the *y* direction. The phase encoding factor varies with the *y* position and corresponds to the spatial frequency k_y. The precessional frequencies of the spins in every voxel within the selected plane to be imaged are assigned according to the phase-encoding and the frequency-encoding gradients. The phase-encoding gradient, G_y, warps the phases of the spins before the signal is acquired. In principle, the area under the G_y gradient waveform determines the amount of phase warping. The MR signal is represented according to a space formalism called *k*-space and the coordinates of the *k*-space are described as integrals of the gradient amplitudes over their duration times:

$$k_x = \gamma \int G_x \, dt$$

$$k_y = \gamma \int G_y \, dt \qquad (2.49)$$

$$k_z = \gamma \int G_z \, dt$$

where k_x, k_y and k_z represents the spatial frequencies in the *k*-space. The direction in which spatial encoding of the MR signal is performed by regulating the precessional frequencies of the spin isochromats is called the frequency-encoding direction, whereas the direction in which spatial information is encoded by modulating the phase angles of the spin isochromats is called the phase-encoding direction. The MR signal is sampled during the frequency-encoding period. The velocity of *k*-space traversal depends upon the amplitude of the gradient and the direction depends on the direction of the gradient.

2.4.3 The Signal from the Object

Considering a magnetic field gradient $\mathbf{G} = G_z\mathbf{k}$, a radiofrequency field $\mathbf{B_1}(t) = B_1(t)\mathbf{i}$ and ignoring relaxation effects, the Bloch equation in the component representation becomes:

$$\frac{dM_x}{dt} = \gamma M_y G_z z$$
$$\frac{dM_y}{dt} = \gamma(M_z B_1(t) - M_z G_z z) \qquad (2.50)$$
$$\frac{dM_z}{dt} = \gamma M_y B_1(t)$$

Equation (2.50) can be transformed to another system of reference rotating around x-axis at an angular frequency $\gamma G_z z$. Thus, at $t=0$, equation (2.50) can be re-written as:

$$\frac{dM_{xc}}{dt} = \gamma M_{zc} B_1(t) \sin(G_z zt)$$
$$\frac{dM_{yc}}{dt} = \gamma M_{zc} B_1(t) \cos(G_z zt) \qquad (2.51)$$
$$\frac{dM_{zc}}{dt} = M_{xc} B_{yc} - M_{yc} B_{xc}$$

where M_{xc}, M_{yc} and M_{zc} are the magnetisation vector components in the new frame of reference. According to the small flip angle approximation, i.e., $\dfrac{dM_{zc}}{dt} = 0$ ($M_{zc} \approx M_0$), and introducing another notation as $M_{\perp c} = M_{xc} + i M_{yc}$, equation (2.51) transforms into:

$$\frac{dM_{\perp c}}{dt} = i\gamma M_0 B_1(t)e^{i\gamma G_z zt} \qquad (2.52)$$

Converting equation (2.52) back to the rotating frame of reference, its solution can be given as:

$$M_\perp(\xi, z) = iM_0 e^{-i\gamma G_z z\xi} \int_0^\xi B_1(t)\, e^{i\gamma G_z zt}\, dt \tag{2.53}$$

where ξ represents the duration of the radiofrequency pulse and z denotes the spatial position along z-axis.

2.4.4 Slice Selection

In the process of slice selection, the spins in a single plane are excited separately from the rest of the volume to be imaged. Slice selection is performed by a narrowband radiofrequency pulse and a linearly varying field gradient. In particular, the magnetic field strength is varied linearly by the field gradient from the centre of the magnet to either side. Consequently, the bandwidth of the radiofrequency pulse corresponds to the resonance frequencies of the spins of the selected slice. The slice thickness is inversely proportional to the steepness of the gradient and directly proportional to the bandwidth of the radiofrequency pulse. Due to the linearly varying gradient, the spins outside the selected area precess at different frequencies than the spins inside the selected area. They are therefore unaffected by the radiofrequency pulse.

Mathematically, slice-selection can be represented as integral over the slice width:

$$M(x, y) = \int_{z_0 - \frac{\Delta z}{2}}^{z_0 + \frac{\Delta z}{2}} M_\perp(\mathbf{r})\, dz \tag{2.54}$$

where $M_\perp$ is the magnetisation given in equation (2.54) as a function of spatial position $\mathbf{r}$, z_0 is the centre of slice and Δz is the slice thickness. The received MRI signal, demodulated at frequency ω_0, can be represented as:

$$S(k_x, k_y) = \int_x \int_y M(x, y) e^{-i\gamma \int_0^t \mathbf{G}(\tau).\mathbf{r}\, d\tau}\, dy\, dx \tag{2.55}$$

It is apparent from equation (2.55) that in order to reconstruct the spatial distribution of magnetisation, that is, the spin density denoted as $M(x, y)$, a 2D inverse Fourier transform is applied to the received MRI signal $S(k_x, k_y)$.

It is noteworthy to consider that after the spins have been tipped into the transverse plane and they start precessing about the effective magnetic field with their Larmor frequencies, the phase differences accumulate between the spins with time. A complete spread of phases over the slice destroys the MR signal. This process is called dephasing. It is a deterministic process. The dephasing amount is equal to the product of bandwidth and duration of the slice selection gradient. To rephase the spins, a rephasing gradient is used which is opposite in polarity to the slice selection gradient and its time duration and bandwidth product amounts to nullify the dephasing factor. This process is termed rephasing.

2.4.5 Phase Encoding

Following the slice selection radiofrequency pulse, a y-gradient, G_y, is turned on for a time t_y during the rephasing lobe of the slice selection gradient. During this interval, the k-space trajectory moves along k_y axis and then moves in the direction according to the x gradient (or frequency-encode gradient). A change in the amplitude of G_y leads to a different line in the k-space.

2.5 Echo Formation

2.5.1 Gradient Echo and Spin Echo

Disentangling the phase effects due to the field inhomogenities and chemical shifts result in a phenomenon called the spin echo. On the other hand, disentangling the phase effects due to applied gradients result in a phenomenon called the gradient echo.

During the generation of a gradient echo, a gradient field perturbs the homogeneity of the field and systematically dephases the spins. A signal is observed just after turning the gradient on but it decays very quickly as the spins dephase. After time, τ, the gradient is reversed. The phases, dephased during the time $t=0$ to $t=\tau$, start to rephase and a gradient echo is formed when spins regain coherence at $t=2\tau$, called echo time, T_E. When the gradient echo is produced, the cumulative area of the gradient waveform equals zero. This phenomenon is demonstrated in Figure 2.6.
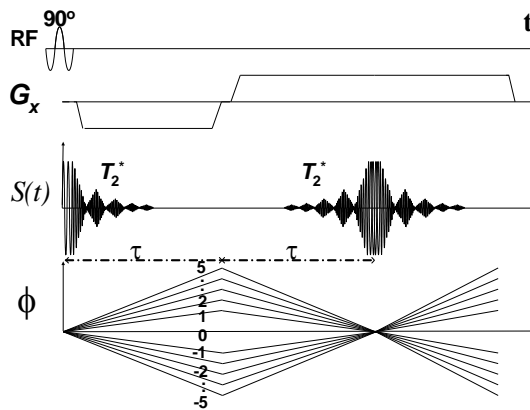
FIG. 2.6. Gradient echo formation is shown. Phase variation of spins at positions -5,-4, 0, 5, is shown by $\phi(t)$. Spins at 1, 2, 5 precess faster than the spins at positions -1, -2, -5 from time $t=0$ to $t=\tau$ and vice verse during the time $t=\tau$ to $t=2\tau$. A gradient echo is formed when all spins regain coherence corresponding to the restoration of aggregate transverse magnetisation at $t=2\tau$. The spins dephase again after $t=2\tau$.

During the formation of a spin echo, the factors of chemical shifts and gradient fields can be neglected and the spins are assumed to experience phase distortions only from the main field inhomogenities following a 90° radiofrequency pulse. After dephasing during a certain time interval, τ, a 180° radiofrequency pulse is applied. This pulse reverses the phases of the dephased spins. After some time, the rephasing spins regain coherence and a spin echo is formed at $t=2\tau=T_E$ (Figure 2.7). The loss of phase coherence encountered from the random field fluctuations, determines the amplitude of the spin echo.
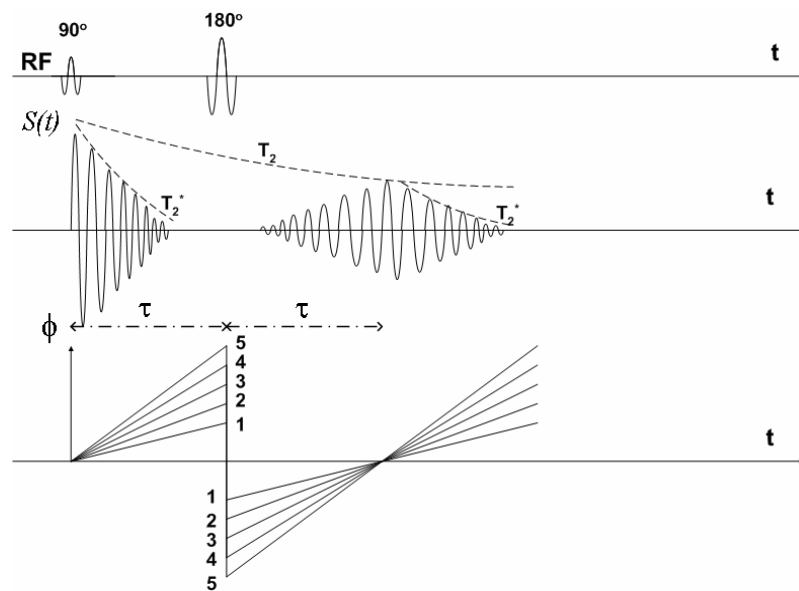
FIG. 2.7. Formation of a spin echo. An exponentially decaying signal after a 90° radiofrequency pulse depicts a T_2^* decay. Dispersive phase variation of spins at different positions is shown by $\phi(t)$. Following a 180° refocusing radiofrequency pulse at $t=\tau$, the phases are reversed and most of the transverse magnetisation is vanished. After refocusing, at $t=2\tau$, spins gain coherence and a spin echo is produced. The signal amplitude, $S(t)$, of the spin echo is determined by T_2 of the sample.

2.6 Rapid Imaging Techniques

Signal intensity variations present in the MR images manifest differences in biophysical properties of the spin system. For instance, pathological differences between different biological tissues affect the relaxation rates, resonant offsets or flow, and attribute to contrast variation in the images. Having been excited according to the specific regime, the MR signal from the volume is weighted with relaxation constants,

such as T_1, T_2, or T_2^*, diffusion or perfusion factors. For the purpose of SNR enhancement by averaging, successive radiofrequency pulses are employed, separated in time, T_R (known as the repetition time). However, although the factors described above determine the effective voxel intensity, equally consequential are the pulse sequence parameters, such as echo time, T_E, repetition time, T_R, and flip angle, α. The magnetisation pertaining to the steady-state, reached following a number of radiofrequency pulses, is given by:

$$S \propto M_0 \left(\frac{1 - e^{\frac{T_R}{T_1}}}{1 - (\cos\alpha)e^{\frac{T_R}{T_1}}} \right) \sin\alpha \, e^{-\frac{T_E}{T_2^*}} \qquad (2.56)$$

In particular, the SNR can be maximised by setting the flip angle α equal to 90°, whereas the spin-density weighted image can be obtained by minimizing T_1 and T_2^* decay with respect to T_R and T_E, respectively. Increasing T_R up to $5T_1$ allows longitudinal magnetisation to recover completely and thus T_1 weighting is minimised. On the other hand, decreasing T_R contributes to suppress longitudinal relaxation between consecutive excitations and consequently the signal amplitude is weighted with the T_1 recovery of the sample.

Because T_2^* is sensitive to tissue morphology and local field inhomogenities it is a suitable parameter for the functional studies. Furthermore, T_2 / T_2^* weighting is accomplished by reduction in T_E and addition in T_R, which in turn eliminate T_1 weighting.

The time available for spatial sampling in MRI is limited by the transverse relaxation time (transverse relaxation times of biological tissues range between 10 and 1000 ms). Demands such as high spatial resolution and high signal-to-noise ratio constrain adequate sampling for the image reconstruction following a single excitation. Multiple radiofrequency excitations are required to complete sufficient k-space sampling or to perform signal averaging. Consequently, the time frame for each

repetitive excitation should allow for adequate longitudinal relaxation to avoid saturation. In order to achieve the best possible SNR in a subsequent shot, it is necessary to wait about $5T_1$ for full longitudinal recovery. In the case of *in vivo* imaging, where typical T_1 values range between few hundreds of milliseconds and 5 seconds, this requirement renders the acquisition times intolerable for patients and volunteers. As such, TR is usually much less than $5T_1$. High temporal resolution is another factor to consider for developing rapid techniques for the applications such as BOLD.

2.6.1 Fast, Low Angle Shot (FLASH)

A method based on the generation of a gradient echo with reduced *TR* and low flip angle was proposed by Haase [9] in 1986. The amplitude depressed by the short *TR* can be compensated if a low flip angle radiofrequency pulse is used. The residual transverse magnetisation is avoided by including additional long duration gradients, called spoilers. Another method to avoid unwanted phase coherences is to employ phase cycling of the radiofrequency pulses. It is instructive to mention that the gradient echo sequence is sensitive to the magnetic field inhomogenities and susceptibilities.

A diagram of the FLASH sequence is presented in Figure 2.8a; *k*-space sampling is performed at the nodes of the equi-distanced Cartesian grid shown in Figure 2.8b. Having been excited by an *α*-pulse and following the slice selective gradients in *z*-direction, the spins start precessing with the same phase and the *k*-space trajectory corresponds to the origin. The combination of the read dephase gradient, G_x, and the phase encode gradient, G_y, moves the *k*-space trajectory to the lower left corner, as shown in Figure 2.8b. Following the application of phase encode gradient, the polarity of the G_x gradient is reversed. The net phase change produced by the frequency-encode gradients is zero at the echo time T_E because the phase change during the dephase gradient segment is cancelled by the opposite phase change during the rephase gradient segment. Factors other than gradients, such as sample-based magnetic susceptibility, influence the phase changes through the entire echo formation process. Thus, the net dephasing cannot be atoned by only the rephasing gradient segment, effectively reducing the MR signal. The echo is sampled during the positive lobe of the G_x

gradient, which results in the acquisition of a single line of k-space. The interval between points on a single line is determined by the dwell time of the analog-to-digital converter and the amplitude of G_x. The spoiler gradients are shown at the end of the acquisition to dephase any residual magnetisation. Such a regime is repeated with the amplitude of G_y incremented to advance the k-space trajectory to the next line starting from origin.

(a)   **(b)**
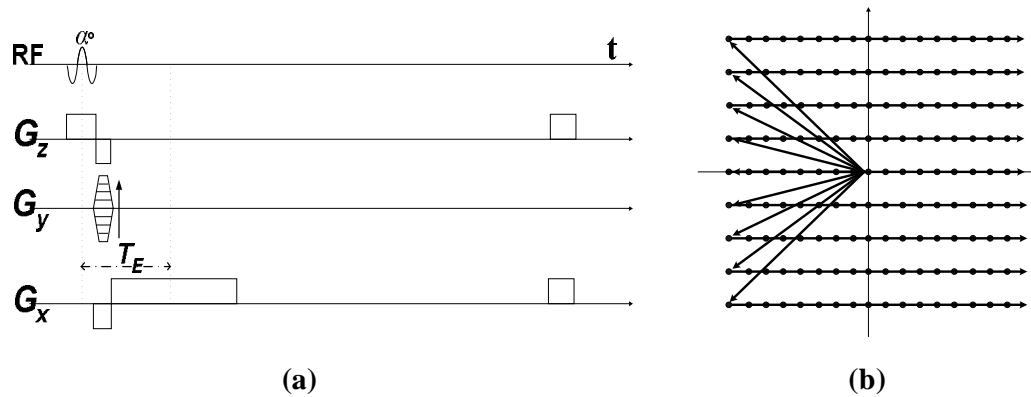
FIG. 2.8. Pulse sequence diagram of FLASH is shown in **(a)** and the corresponding k-space trajectory for traditional imaging is shown in **(b)**. After radiofrequency excitation, the position in k-space is moved to the bottom left corner determined by the phase-encoding gradient, G_y, and frequency-encoding gradient, G_x. The gradient echo occurs at $t=T_E$ and then the next k-space traversal starts again from the origin.

T_1 weighted imaging can be accomplished with the gradient echo sequence. For that purpose, a 180° radiofrequency pulse is applied before the gradient echo sequence to invert the longitudinal magnetisation. An inversion delay, TI, between the 180° radiofrequency pulse and 90° radiofrequency pulse of the gradient echo sequence, allows the longitudinal magnetisation to recover following inversion. The inversion delay ascribes a range of contrasts to images depending on T_1 of the tissues, for example, rapidly relaxing tissues appear darker and vice versa at a particular time instance during the course of magnetisation recovery. When the recovering magnetisation equals zero, it corresponds to null image intensity of the relevant tissue.

2.6.2 Echo Planar Imaging (EPI)

Echo planar imaging (EPI) is a rapid imaging method invented by Mansfield [10] in 1977. Unlike the sampling strategy of repeating an excitation-sampling combination over every k-space line, EPI enables the entire k-space acquisition following a single radiofrequency excitation. A schematic of a generic EPI pulse sequence is shown in Figure 2.9. An initial pair of frequency-encoding and phase-encoding gradients leads the k-space trajectory from origin to the first k-space line in the lower left k-space corner. Then, successive oscillatory frequency-encoding gradients are applied to generate the train of echoes. The positive and negative gradient lobes result in alternating directions of traversing the k-space lines and the blipped phase-encoding gradients advance the k-space trajectory from one line to another in the phase-encoding direction. The centre of every echo ideally coincides with the point $k_x=0$. Although every gradient traversal forms its own echo, only the echo that coincides with the k-space centre is considered to calculate the echo time, T_E.

The effect of an intrinsic decay owing to T_2^* relaxation constrains EPI-based sampling strategies. T_2^* relaxation contributes to MR signal dropout across the entire image. The overall signal dropout is determined by the amount of signal lost to T_2^* relaxation at the time of traversing the k-space centre. Image distortion in the phase-encoding direction and strong local susceptibility induced signal drop-out are other limiting factors for the EPI based acquisitions. Geometric distortions occur due to the fact that the phase evolution of spins continues as the different lines of k-space are collected. The low bandwidth in the phase-encoding direction makes EPI more susceptible to the off-resonance artefacts. Background susceptibility differences, imperfect gradient bipolar pulses or any gradient-induced eddy currents can cause mismatches between the odd and even lines of k-space. Such k-space errors lead to the FOV/2 Nyquist ghosts.
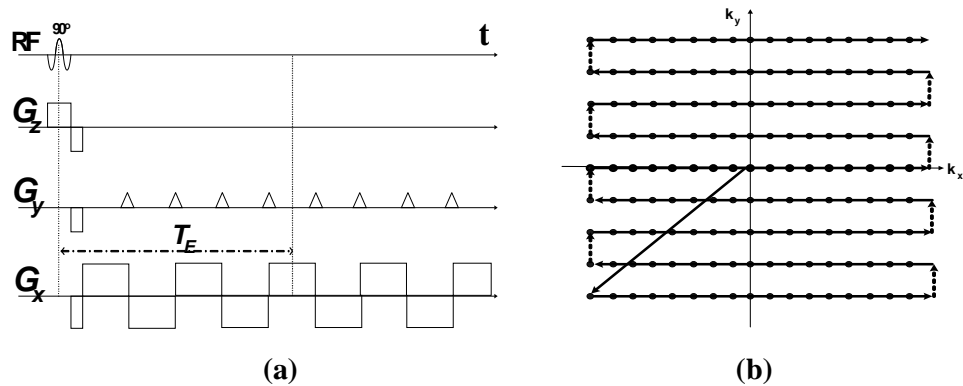
FIG. 2.9. A generic echo planar imaging sequence is depicted in **(a)** along with the corresponding k-space trajectory in **(b).** Multiple gradient echoes are acquired by employing rapid 'blipped' phase-encoding gradients and read gradient reversals. The blipped phase-encoding scheme consists of an initial dephasing gradient lobe followed by a series of small blips acquiring the gradient echoes on separate *k*-space lines.

2.7 References

1. Rabi II, Zacharias JR, Millman S, Kusch P. A new method of measuring nuclear magnetic moment. Phys. Rev. 1938;53;318-318.

2. Bloch F, Hansen WW, Packard ME. Nuclear induction. Phys Rev 1946;69:127.

3. Purcell EM, Torrey HC, Pound RV. Resonance adsorbtion by nuclear moments in solid. Phys Rev 1946;69:37-8.

4. Stern O, Gerlach W. Über die Richtungsquantelung im Magnetfeld. Ann Phy Leipzig 1924;74:673-99.

5. Dirac PAM. The principles of quantum mechanics. 4 ed. Oxford: Clarendon Press; 1993. 314 p.

6. Ernst RR, Anderson WA. Application of Fourier transform spectroscopy to magnetic resonance. Rev Sci Instru 1966;37:93-102.

7. Lauterbur PC. Image formation by induced local interactions: examples employing nuclear magnetic resonance. Nature 1973; 242;190–191.

8. Mansfield P, Grannel PK. NMR diffraction in solids. J Phys C: Solid State Phys 1973; 6:L422-L426.

9. Haase A, Frahm J, Matthaei D, Hanicke W, Merboldt KD. FLASH imaging. Rapid NMR imaging using low flip-angle pulses. J Magn Reson 1986;67:258-66.

10. Mansfield P. Multi-planar image formation using NMR spin-echoes. J Phys C 1977;10:L55-8.

Chapter 3

Optimisation of a Rapid Relaxation Rate Mapping Method

3.1 Introduction

Measurement of the spin-lattice relaxation time constant, T_1, can provide important insights into pathological processes in the human brain such as multiple sclerosis [1] or hepatic encephalopathy [2]. Acquisition times, however, tend to be long and therefore reductions in acquisition times are desirable to attain routine clinical objectives. In addition to rapid acquisition, many other factors, for example, high sensitivity, high isotropic resolution and high T_1 contrast determine the selection of the T_1 mapping method.

Over the past few decades, a wide range of rapid T_1 mapping methods have been published. Conventionally, T_1 relaxation rates are calculated using either the inversion recovery (IR) or the saturation recovery (SR) methods. These methods sample the T_1 recovery curve at multiple time-points. In order to increase the time-point sampling efficiency, "one-shot" methods have been proposed. Given that the magnetisation is in an equilibrium state, one-shot methods employ successive small flip angle radiofrequency pulses to continuously tip down the longitudinal magnetisation into the transverse plane in each excitation and thereby sample different time-points on the T_1 recovery curve. The signal-to-noise ratio is the limiting factor for such techniques. However, the one-shot Look-Locker method (LL), proposed in [3], eliminates the need to wait for the establishment of equilibrium magnetisation before the application of successive radiofrequency pulses. Stimulated echoes (STE) based one-shot methods have also been proposed, but they are somewhat less accurate than the SR, IR and LL methods [4]. In general, comparatively, the SNR is better in the case of basic the SR or IR methods, with the advantage that the LL-based approaches accomplish T_1 mapping in

a rapid time. In addition, the LL method remains less influenced by T_2 ; it is, however, affected by magnetic field inhomogeneities.

In order to achieve faster acquisition, a few EPI-based T_1 mapping methods have been introduced [5], [6]. The Look-Locker EPI (LL-EPI) method is capable of producing T_1 maps with high spatial and temporal resolution. Unfortunately, however, the IR-EPI approach suffers from problems of distortion, signal loss, etc.

Another set of sequences based on FLASH have been proposed for T_1 mapping. The IR snapshot-FLASH method samples the T_1 recovery curve at multiple time-points following an inversion radiofrequency pulse [7]. As it is a single, slice-by-slice acquisition strategy, achieving high spatial resolution necessarily reduces temporal resolution. Furthermore, to increase temporal resolution, segmented k-space acquisition schemes have been used [8], [9]. However, the acquisition time of a single-slice *in vivo* T_1 map remains at about 4 min. In addition, the time after the inversion pulse, termed TI (Inversion Time), also adds to the total acquisition time. Despite losing the dynamic range of the recovery data, the saturation-recovery approach [10] circumvents the need to wait for a full recovery of the magnetisation resulting in rapid acquisition of time-points. An improved LL-based T_1 mapping technique by obtaining a single slice image at multiple time-points following an inversion pulse has been reported [11], [12]. A multislice and multipoint T_1 mapping using a FLASH-based sequence has been demonstrated at 4.1T [13].

TAPIR (T_1 mapping with Partial Inversion Recovery) is a Look-Locker based multishot sequence for fast multislice T_1 imaging [14], [15]. TAPIR is capable of multipoint *in vivo* imaging with high spatial resolution (1 mm in-plane) by interleaving slices and time-points. The apparent temporal resolution is enhanced by virtue of the multishot acquisition as compared to the IR-EPI technique, the snapshot FLASH method, or the segmented snapshot FLASH technique. TAPIR also minimises the dead time needed to allow the full longitudinal magnetisation recovery. Another method for rapid T_1 mapping in clinically acceptable time has been presented [16]. It obtains multiple samples for curve-fitting through spiral acquisition with one radiofrequency pulse train without waiting for full longitudinal magnetisation recovery. A method to generate the T_1 maps from shifted spin echoes and stimulated echoes has been proposed

[17], but multipoint methods are preferred to this method in order to achieve high precision, accuracy and temporal resolution for multislice T_1 mapping. Another full-brain T_1 mapping scheme based on a multislice inversion recovery fast spin echo imaging using a time efficient slice ordering technique is reported [18]. Even though it performs better in the case of inhomogenous fields, the echo train length (ETL) dependence, low temporal resolution and interslice interference effects constitute potential restrictions.

The accuracy, precision and temporal resolution of TAPIR for measuring T_1 are high, but a reduction in the acquisition time is required. In this thesis, a novel k-space acquisition scheme, called line-sharing, is proposed for TAPIR. The objective is to devise a methodology to accelerate sampling of the T_1 recovery curve employed by TAPIR without compromising the temporal and the spatial resolution. In particular, the line-sharing method addresses the issue of acquiring sufficient k-space data required for high quality T_1 mapping using TAPIR. According to the proposed scheme, the central k-space region, termed a "keyhole", is sampled in full and the high-frequency k-space region in the phase-encode direction is undersampled. To circumscribe the possible fold-over artefacts due to the undersampling, the high-frequency phase-encode lines can be reconstructed through linear interpolation as described in the methods section. In the past, a keyhole-based method for the partial k-space acquisition has been employed to expedite the acquisition of serial images [19]. Another keyhole technique was described [20] which emphasizes replacement of the complete high-frequency phase-encode region with the corresponding region of a reference k-space in the case of $T_{1\rho}$ mapping.

Rapid acquisition of time points along the T_1 recovery curve through line-sharing in the interleaved slice and time-points regime can be a useful approach. The apparent temporal resolution of TAPIR, determined by the number of slices, can be increased by acquiring extra time-points, as shown in Figure 3.1. Hence, it should be possible to further improve the accuracy of TAPIR.

It has been described previously that the performance of TAPIR is dependent on the careful selection of the optimal sequence parameters for a specific experimental regime [21]. The optimised values of parameters such as repetition time, TR, flip-angle, α, and the preparation delay, τ, are used in this work in order to evaluate the systematic

errors introduced by the rapid line-sharing acquisition scheme for TAPIR. Analysis of another parameter to be optimised, i.e., the number of time points to be line-shared along the T_1 recovery curve in order to attain optimal performance, is also introduced here. Furthermore, sampling of the T_1 recovery curve can be accelerated by using parallel imaging methods such as GRAPPA (Generalised Autocalibrating Partially Parallel Acquisitions) [24], for instance. Combining GRAPPA with line-sharing can potentially further accelerate the process of image acquisition by line-shared, parallel imaging for T_1 mapping.

(a) Standard TAPIR scheme

(b) Time saving through line-sharing

(c) Acquisition of extra slices

(d) Acquisition of extra time-points
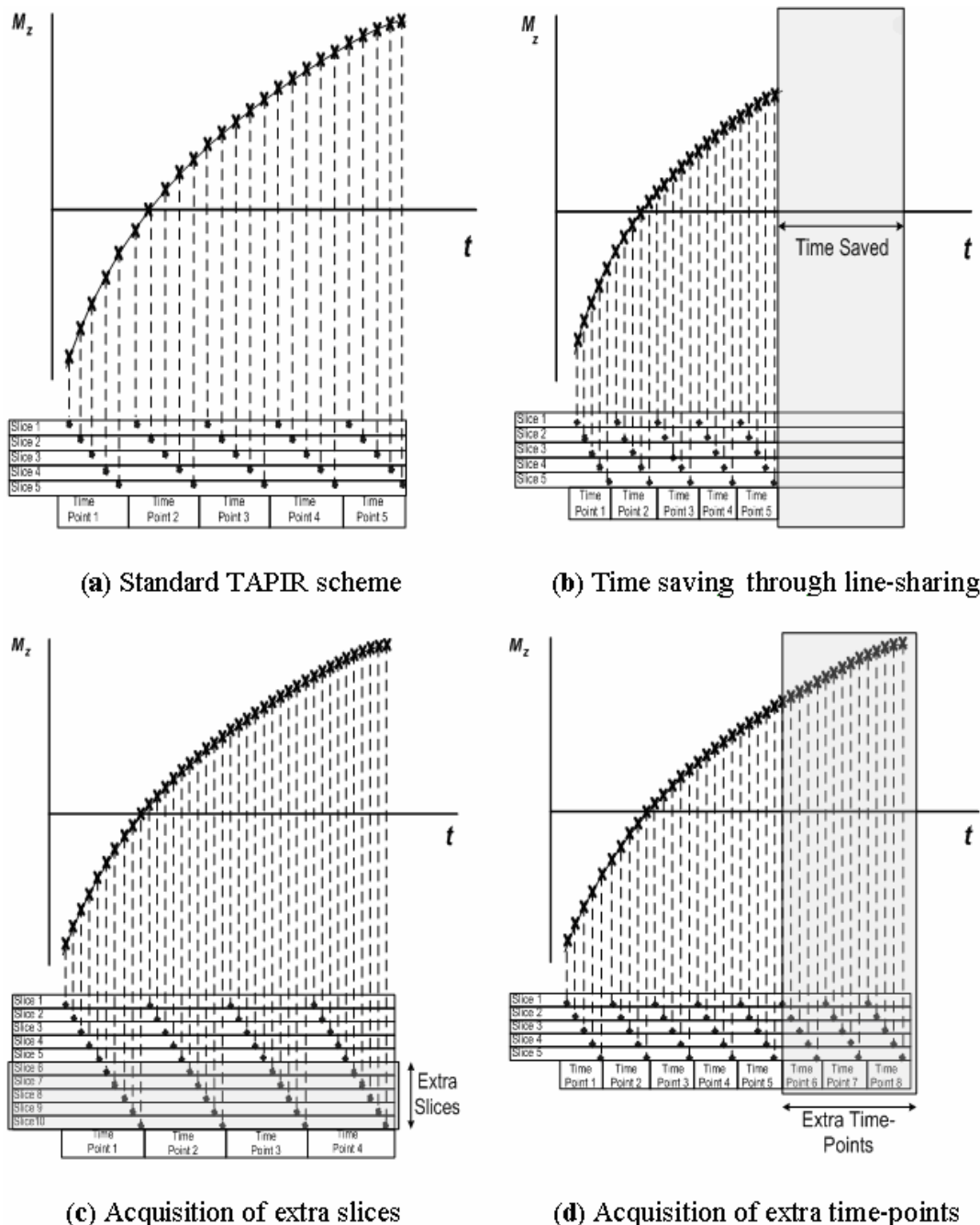
FIG. 3.1. (a) A schematic representation of multi-slice sampling along the T_1 recovery curve using standard TAPIR. Acquisition of multiple interleaved slices and line-shared time-points during T_1 recovery curve is shown. **(b)** A line-sharing based sampling scheme proposed for TAPIR which facilitates a more rapid acquisition as compared to **(a)** and the time saving that can be achieved is illustrated. **(c)** In addition, a further increase in the number of slices can be achieved by reducing the number of sampled time-points in a fixed time frame. **(d)** Rapid acquisition affords an increase in the number of time-points along the T_1 recovery curve keeping the number of slices fixed in a fixed time frame.

3.2 Theory

3.2.1 The Signal Model

The TAPIR sequence comprises two components, a non-selective [90°-delay-180°] magnetisation-preparation module and a Look-Locker acquisition module which in turn incorporates the repetitive application of the slice-selective α pulses. A series of low-flip angle α pulses, applied to a given slice, influences the longitudinal magnetisation attained in the steady-state, the value of which is given by:

$$m_{\infty} = \frac{1 - e^{-\frac{TR}{T_1}}}{1 - cos(\alpha) \, e^{-\frac{TR}{T_1}}} \qquad (3.1)$$

where T_1 is the longitudinal relaxation time and TR is the time between α pulses applied to a given slice. Subsequently, the value of the longitudinal magnetisation is normalized to its thermal equilibrium value.

The generated longitudinal magnetisation can be expressed through the magnetisation prepared following the excitations by a 90° pulse and a 180° inversion pulse separated by the time period τ, i.e.,

$$m_z = 1 - e^{-\frac{t_n}{T_1}} (1 + C (1 - e^{-\frac{\tau}{T_1}})) \qquad (3.2)$$

where t_n is the time between the inversion pulse and the first time point acquisition of slice n and the inversion pulse efficiency is represented by C which is defined as the negative ratio of the longitudinal magnetisation following inversion to the initial longitudinal magnetisation (which would exist in the absence of inversion pulse).

A Look-Locker based method relates the longitudinal magnetisation evolution from the initial value, m_z, to the steady-state value, m_{∞}, according to the following relation:

$$m = m_\infty - (m_\infty - m_z)e^{-\frac{t_p}{T_1^*}} \qquad (3.3a)$$

where T_1^* is:

$$\frac{1}{T_1^*} = \frac{1}{T_1} - \frac{ln\left(cos\left(a\right)\right)}{n \cdot TR} \qquad (3.3b)$$

Sampling along the T_1 recovery curve is given as follows:

$$t_p(n) = t_n + (n-1)TR \qquad (3.4)$$

where n is a slice index, $n=1, 2,...., N$, N is the total number of slices, and p represents the time-point index, $p=1, 2,...., N_p$, N_p equals total number of time-points to be sampled. Subsequently, the signal intensity, S, can be given by the following expression:

$$S(x, y, t_p) = M_0(x, y, t_p) \sin\alpha \left(m_\infty(x, y, t_p) - \left(m_\infty(x, y, t_p) - m_1(x, y, t_p)\right)e^{-\frac{t_p}{T_1^*(x,y,t_p)}} \right) \qquad (3.5)$$

where x and y represents the spatial coordinates and t_p represents time-point.

3.2.2 Optimisation

The signal model in equation (3.5) introduces the dependence of the sampling of the evolving magnetisation on the number of slices to be sampled. Optimization of the multi-parameter function for TAPIR has been described in [21]. The underlying interleaved sampling strategy limits the temporal resolution of the longitudinal magnetisation. The number of points sampled during signal evolution is an influential parameter to be optimised. Rapid sampling of the evolving magnetisation would reduce the potential increment in inter-time-point distance resulting from an increase in the number of slices to be acquired. Based on this fact, it becomes necessary to devise a

rapid acquisition strategy to enable an accurate and precise measurement of the longitudinal magnetisation under these given conditions.

Uniform temporal sampling of the evolving longitudinal magnetisation for each slice is utilised in the TAPIR acquisition scheme. Previously, full k-space sampling was performed at each time-point. Therefore, it is advantageous to consider k-space sampling at each time-point in a manner that is somehow decimated. Hence, sampling in such a manner would allow for the rapid sampling of the longitudinal magnetisation. Additionally, by considering only a certain number of time-points for T_1 mapping, this work extends the previously optimised model of TAPIR to include the acquisition of more slices owing to rapid acquisition.

In order to provide an alternative to optimise the temporal dimension of the TAPIR model, it is appropriate to compare the performance of the line-sharing method with a parallel imaging method such as GRAPPA, for instance, which can also potentially improve the acquisition speed. Assuming the same measurement parameters, receiver bandwidth, spatial resolution and voxel size, a direct comparison of the reconstructed T_1 values should give an indication of the method performance.

3.2.3 Line-Sharing

In MRI applications, the SNR relevance of k-space lines decreases with increasing phase-encode number since these outer lines contain mainly information about spatial resolution. The method of obtaining the minimal k-space data for T_1 mapping using the line-sharing scheme relies on the fact that the keyhole contributes maximally to the SNR in the reconstructed image. Figure 3.2 shows a schematic of the line-sharing method.
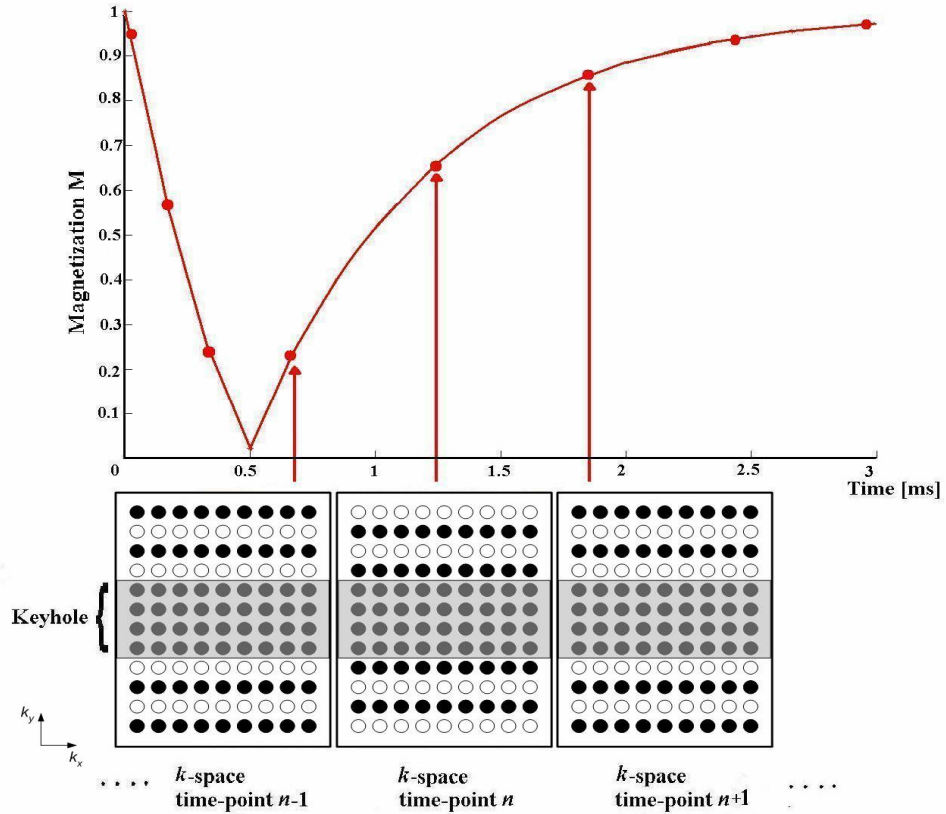
FIG. 3.2. A schematic representation of the line-shared sampling scheme along the T_1 recovery curve. Acquisition of the line-shared time-points is shown. The skipped phase-encode lines are shown as white circles, whereas the acquired phase-encode lines are shown as black circles at time-points *n*-1, *n,* and *n*+1. The keyhole acquired at every time-point is shown as the grey-shaded region.

During the course of line-sharing, the high-frequency region of *k*-space is undersampled by omitting every second line while fully sampling the keyhole which comprises one-eighth of the full *k*-space. As multiple time-points on the T_1 relaxation curve are sampled in TAPIR, omission of lines is performed in an interleaved way. For odd *time-points* (1, 3, …), even *lines* (2, 4, …) of *k*-space are omitted whereas that scheme is reversed for even time-points i.e., lines 1,3,5, .. are sampled for the first acquired time-point on the relaxation curve while lines 2, 4, 6, .. are acquired for the second time-point. For each time-point, except the first and the last, the complex valued *k*-space data for the omitted lines are linearly interpolated using the complex-valued data of the corresponding lines from the preceding time-point and the succeeding time-point, as shown in Figure 3.2. If D_p represents complex data for a missing line at a time-

point t_p, D_{p-1} represents complex data at a time-point t_{p-1}, and D_{p+1} represents complex data at a time-point t_{p+1}, then:

$$D_p(k_x, k_y, t_p) = \frac{D_{p-1}(k_x, k_y, t_{p-1}) + D_{p+1}(k_x, k_y, t_{p+1})}{2} \tag{3.6}$$

The omitted lines of the last time-point are substituted from the corresponding lines of the second last time-point. Correspondingly, omitted lines at the first time-point are substituted from the corresponding lines of the second time-point. In the case of reception using a phased array receive coil, line-sharing can be applied to data acquired in each channel of the coil.

In addition to basic line-sharing, this method can be applied to more than one skipped phase-encode line, as demonstrated in Figure 3.3.
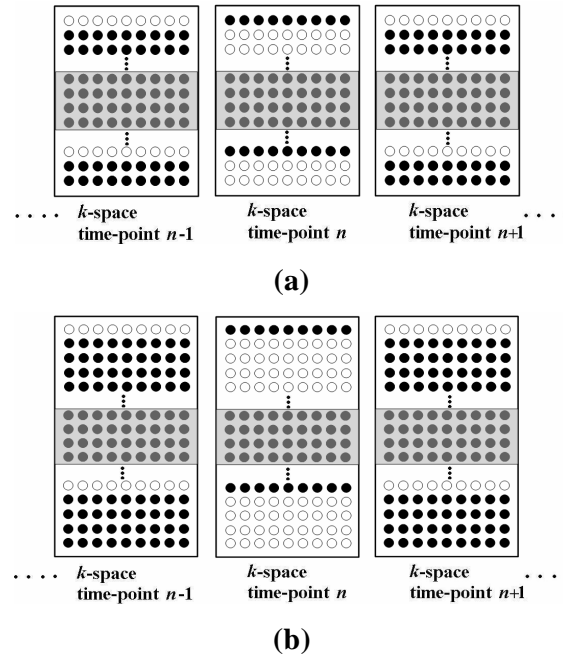
FIG. 3.3. A schematic representation of the line-sharing based sampling scheme along the T_1 recovery curve where the line-sharing factor in **(a)** is 2 and in **(b)** is 4. In **(a)**, 2 phase-encode lines and in **(b)**, 4 phase-encode lines, as shown in the depicted pattern, are linearly interpolated using the correspondingly acquired phase-encode lines in the neighbouring time-points. The skipped phase-encode lines are shown as white circles, whereas the acquired phase-encode lines are shown as black circles at the time-points n-1, n and n+1. The keyhole acquired at every time-point is shown as the grey-shaded region.

3.2.4 GRAPPA

In the parallel imaging methods such as AUTO SMASH, a line of acquired *k*-space in each channel of a phased array coil is fitted to the sum of the additionally acquired *k*-space lines, called auto-calibration signal (ACS) lines, where each ACS is acquired in each channel. The obtained coefficients are used as weights to reconstruct the missing *k*-space data. Acquiring additional ACS lines implies multiple fits for each missing line in the method termed VD AUTO SMASH and this moderates the noise and coil profile imperfection effects [22], [23]. Such data-driven methods, which are independent of explicit coil sensitivity information, employ a data fitting method to find weights from the acquired data to reconstruct the missing data. Instead of line-sharing, the parallel imaging methods could accelerate acquisition of the required number of time-points. GRAPPA is based on a reconstruction similar to VD AUTO SMASH with an additional application of a block-wise fitting process [24]. In GRAPPA, first uncombined images are reconstructed for each coil and then a sum-of-squares image is calculated. However, data from multiple lines acquired in each coil are used to fit the ACS lines in a single coil. Specifically, the number of lines used to reconstruct a single line is termed a block. Consequently, the weights to generate all missing lines in a coil can be obtained by block-wise fitting. Let the missing lines of the *k*-space of a single time-point be represented as $D_{n,p}$, then the linear system of equations is written as:

$$D_{n,p}(k_x, k_y - d\Delta k_y, t_p) = \sum_{c=1}^{N} \sum_{b=0}^{B} w(n,b,c,d) \, D_{c,p}(k_x, k_y - bA\Delta k_y, t_p) \tag{3.7}$$
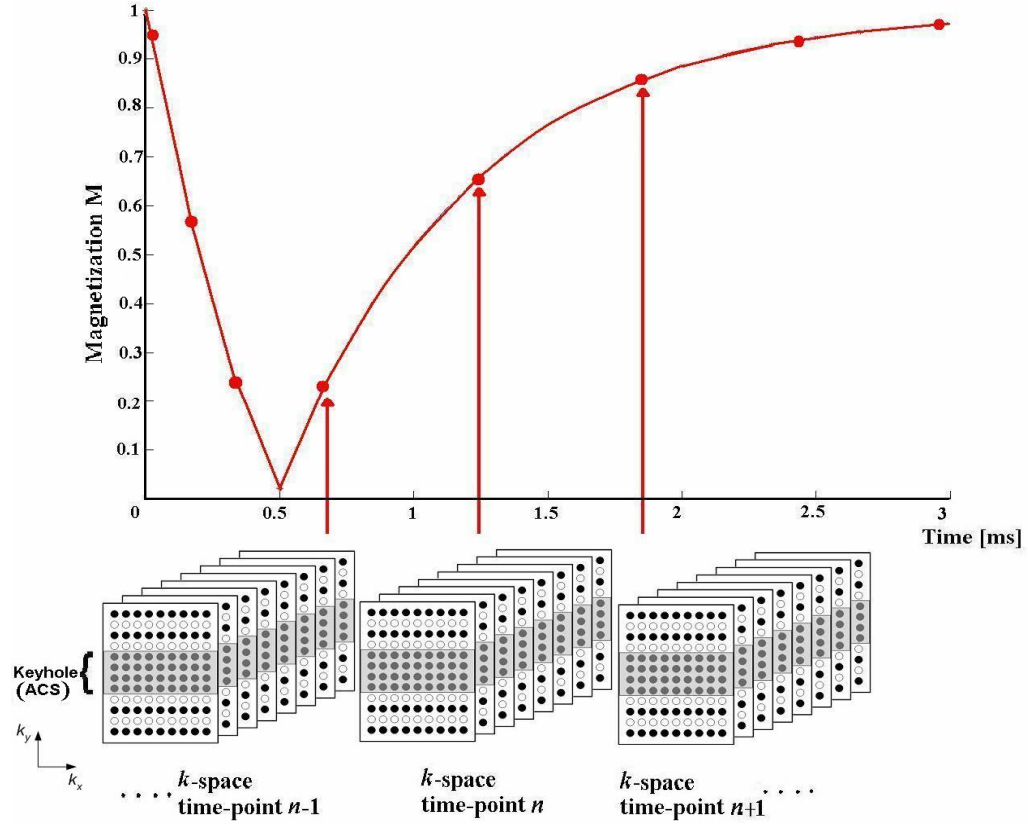
FIG. 3.4. A schematic representation of the GRAPPA algorithm for reconstruction of the missing *k*-space data acquired in each of 8-channel phased array coil along the T_1 recovery curve. The black circles represent the acquired lines and white circles represent the skipped lines. The grey circles depict the auto-calibration signal (ACS) lines acquired in each coil.

where *n* specifies the coil index, $d\Delta k_y$ signifies the shift in the phase encode, t_p represents the time-point, *c* is the coil index, and *b* refers to the block index, one block is composed of one acquired line and *A*-1 missing lines from each coil, and *w* represents the unknown weights for the reconstruction of missing lines. Hence, following the calculation of weights, the missing data can be synthesised by applying the weights to the data acquired in different coils. Furthermore, a sum of squares reconstruction can be used to combine the coil images. This process of calculating the missing *k*-space lines can be repeated for each time-point acquired along the T_1 recovery curve. Hence, the GRAPPA reconstruction strategy calculates the full *k*-space data in each coil, and then reconstructs the time-point image, as shown in Figure 3.4.

3.2.5 Line-Shared-GRAPPA

In the line-shared-GRAPPA technique, shown in Figure. 3.5, the k-space undersampling factor is two-fold as compared to the basic line-sharing scheme. At each time-point, one of the skipped phase-encode lines is reconstructed through line-sharing. Following line-sharing, the other missing phase-encode lines can be reconstructed through GRAPPA. In other words, considering that the reduction factor for GRAPPA is 2, every other phase-encode line is line-shared. As in the case of GRAPPA, the ACS lines can be selected from the keyhole data. Hence, the acquisition time for each time-point can be further reduced by employing the line-shared-GRAPPA method.
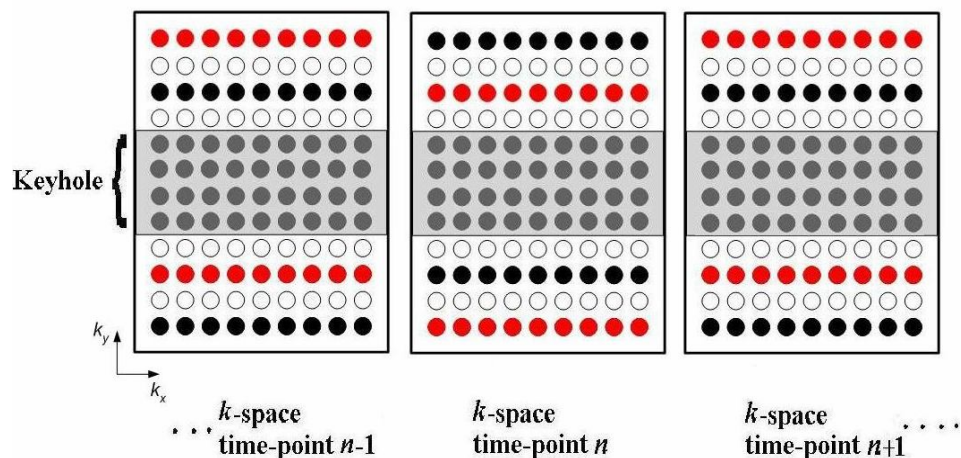
FIG. 3.5. A schematic representation of the line-shared-GRAPPA algorithm. The black circles represent the acquired lines and the white and the red circles represent the skipped lines. Line-sharing is applied on the phase-encode lines represented as red circles afterwards. Following line-sharing, the data that are still missing are reconstructed through GRAPPA.

3.3 Methods

3.3.1 Pulse Sequence

In TAPIR, a 90° nonslice-selective pulse is applied and sufficient longitudinal relaxation is allowed to take place during the long delay period, τ. Thereafter, a 180° nonslice-selective inversion pulse is applied and any residual transverse magnetisation is immediately spoiled by means of a large spoiler gradient as shown in Figure. 3.6. Following application of the 90° and 180° hard pulses, a slice-selective low flip-angle pulse (α-pulse) is applied. The magnetisation is then repeatedly sampled by means of multiple α-pulses for multiple slices. Following the application of each α-pulse, a gradient echo is recorded for each slice. Following the acquisition of multiple slices, the whole procedure for the same k-space line is repeated starting at slice 1; this loop ensures the acquisition of multiple time-points. The whole sequence is then repeated for the next set of lines.

The inhomogenous $\mathbf{B}_1$ field generated by the transmitter coil, off-resonance effects on the radiofrequency inversion pulse, imperfection of the inversion pulse and relaxation effects during the inversion pulse influence the precise and accurate calculation of the T_1 relaxation times. Due to the inhomogeneous $\mathbf{B}_1$ field produced by the transmitter coil, the inversion of the magnetisation by the 180° hard pulse can be incomplete and unwanted transverse magnetisation results. The TAPIR-based T_1 mapping method takes into consideration a measure of the (in)efficiency of the inversion pulse using the TAPIR-IE (TAPIR with Inversion Efficiency) sequence and thereafter including the negative ratio of the longitudinal magnetisation following inversion to the initial longitudinal magnetisation (which would exist in the absence of 180° hard pulse), in the fitting routine. The ratio ranges between 0 and 1 (or 0-100%). If incomplete inversion is not taken into account in the T_1 measurement then it results in the introduction of systematic errors [21]. The TAPIR-IE sequence is an addition to the original TAPIR sequence for measuring the inversion efficiency of the 180° pulse. This sequence can be depicted as:

90°-τ-$\{180^{o}$-spoil-$180^{o}\}$-spoil-multi-slice acquisition

The TAPIR-IE sequence was repeated twice for each phase-encode line, once with and once without the combination of the two 180° pulses enclosed in the parentheses. Two separate images were reconstructed for each slice following data reordering. The pixel intensity ratios of these two sets of images were subsequently used during the fitting of the TAPIR dataset to obtain inversion efficiency maps where the latter were used to correct the T_1 maps for inversion pulse imperfections.
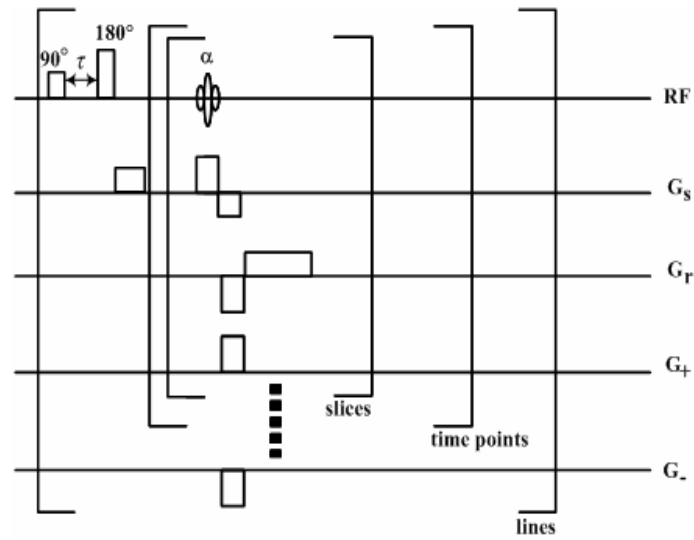
FIG. 3.6. The TAPIR sequence diagram. The separation of the 90°-180° pulses is not shown to scale. Following the application of a nonselective 90° pulse, the transverse magnetisation thus created dephases during the long delay period, τ. After this delay time, a nonselective 180° pulse inverts all recovered magnetisation and any residual transverse magnetisation is spoiled by means of a large crusher gradient. The inverted magnetisation is sampled in the following way: the most peripheral line in k-space is acquired by the application of a single slice-selective α-pulse. The α-pulse excitation module is repeated for the next slice, but again for the same line in k-space. Following the acquisition of n slices, the whole procedure, for the same k-space line, is repeated starting at slice 1; this loop ensures the acquisition of multiple time-points. Following acquisition of the required number of time-points and slices 90°-180° pulse combination is applied and the next line is acquired in an identical manner. The maximum and minimum values of the phase-encoding gradient are denoted by G_+ and G_-, G_s is the slice select gradient, and G_r is read gradient.

3.3.2 *In Vivo* Experiments

In vivo data of a healthy volunteer were acquired on a 4T system using TAPIR. The sequence parameters were: TR=20 ms, TE=2.5 ms, BW=700 Hz/Px, τ=2000 ms, α=26°, TI=10 ms, 5 slices, 500% slice gap, slice thickness=2 mm, FOV=256 mm x 256 mm, EPI factor=1 and time-points=20. The matrix size was 256x256. An 8-channel phased-array receive coil was used and the *in vivo* raw data were acquired from each of the 8 channels.

The inversion efficiency of the TAPIR sequence was corrected using a separate inversion (in)efficiency (IE) measurement using TAPIR-IE, with similar parameters as in the TAPIR sequence except for the resolution, which was set to the matrix size of 64 in the read-out direction. The voxel size was 4x4x2 mm³ for the IE mapping measurement. Two separate images, one with and one without the application of two inversion pulses in the IE mapping sequence, were produced for each slice. The pixel intensity ratios of these two sets of images were used in the accurate and precise calculation of T_1 maps using an in-house tool based on the Levenberg-Marquardt algorithm.

3.3.3 Data Processing and T_1 Mapping

For each time-point along the T_1 recovery curve, raw data were acquired from each channel of the 8-channel phased array coil. Thereafter, the multi-channel line-sharing method was applied to the *k*-space data acquired in each channel. The line-shared data from each channel were Fourier transformed resulting in the reconstruction of the so-called line-shared images. The keyhole region contained 32 phase-encode lines. For each time-point, the line-shared images from each of the phased array receiver coils were combined by using the sum-of-squares algorithm. Those were used to calculate the line-shared T_1 map. In addition, the original T_1 map was reconstructed using the original data without line-sharing for comparison. All T_1 maps were obtained using an in-house tool based on the Levenberg-Marquardt algorithm. In addition, line-sharing with sharing factor 2 and 4 was implemented using the same procedure. Using the same obtained raw data, GRAPPA calculations were performed with the block size of 4 and ACS lines were selected from the 32 lines in the keyhole regions mentioned in

the theory section. Further, the line-shared-GRAPPA method was implemented using the same parameters. The GRAPPA method was applied using the freely available MATLAB toolbox [25]. T_1 maps using GRAPPA processed time-point images were calculated in the usual way.

3.4 Results

Assuming the signal to be in steady-state, computer simulations were performed to investigate the effect of line-sharing and GRAPPA on a single time-point image. A simulated time-series of a T_1-weighted homogenous phantom was obtained using MATLAB and the corresponding k-spaces of size 64x64 were obtained by performing Fourier transformation on the time-series. To simulate the effect of turning-off the phase-encode gradient, the central k-space line was used in place of all the phase-encode lines. Afterwards, line-sharing was performed on the simulated k-spaces. A Fourier transformation of the selected k-space points depicting the intensity values along the phase-encode direction lead to a simulated point-spread function (PSF). Ideally, it should approximately be a delta function as there was no effect of phase-encoding. These calculations were repeated for three different T_1 relaxation rates, i.e., T_1=500 ms, 750 ms and 1600 ms. The simulated PSFs for line-sharing are shown in Figure 3.7 (a). In the case of PSF simulations for GRAPPA, 8-channel images were obtained by multiplying a single T_1-weighted image of homogenous phantom with 8 different simulated coil sensitivity profiles. The coil sensitivity profiles were simulated using the method described in [25]. Afterwards, the k-spaces with phase-encoding turned off were simulated in the similar fashion as in the case of line-sharing. Following the same procedure as in the case of line-sharing, the simulated PSF was obtained for GRAPPA and it should also ideally approximate a delta function, as shown in Figure 3.7 (b).

(a)

(b)
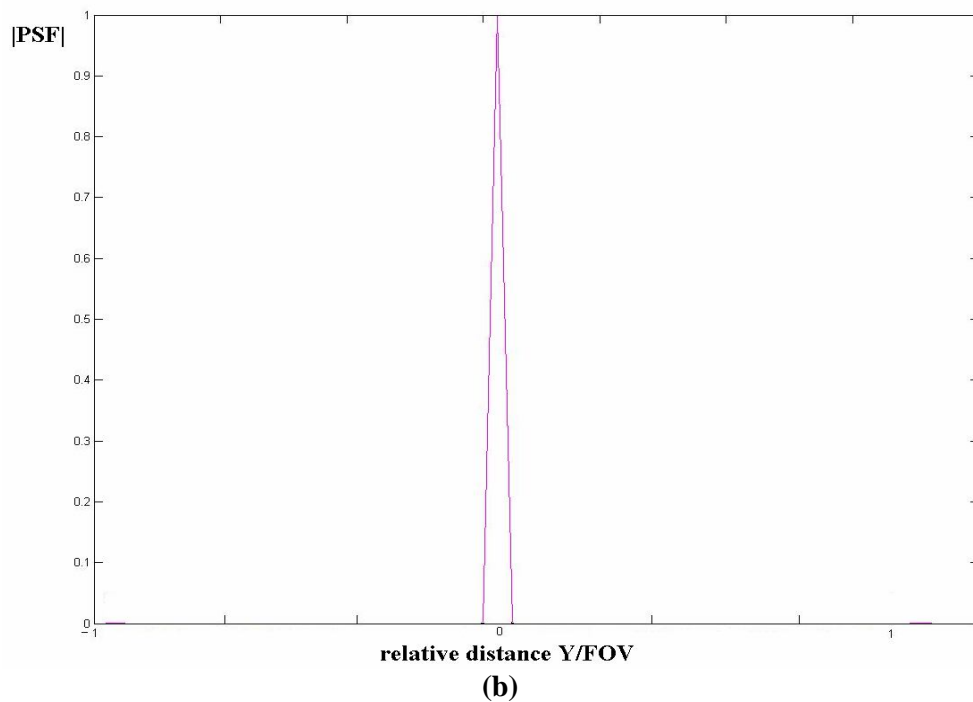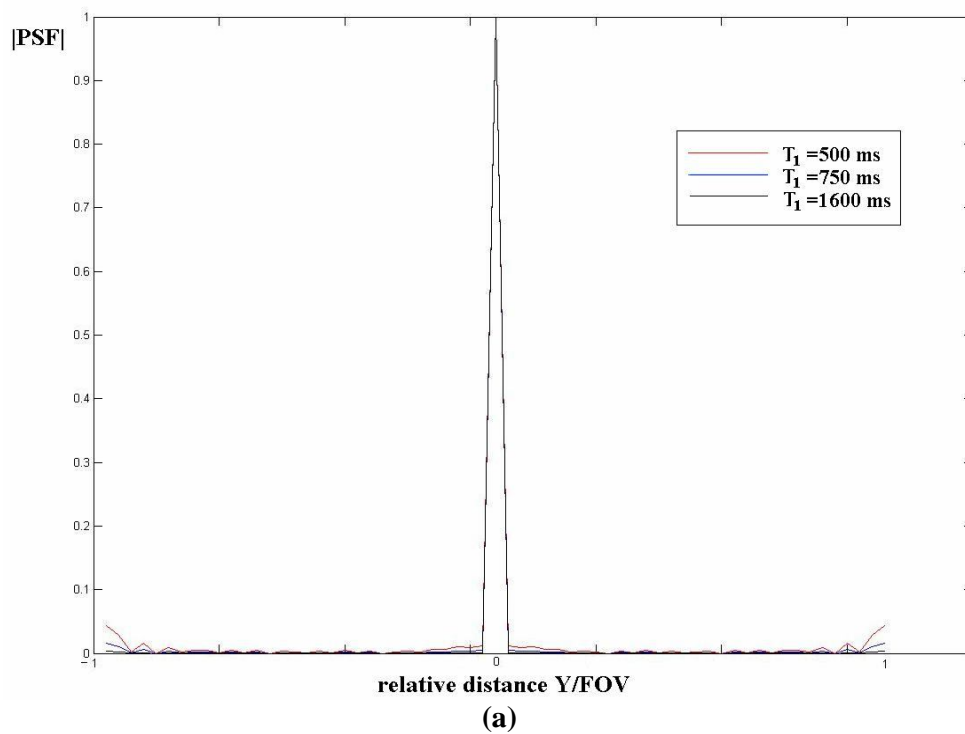
FIG. 3.7. (a) The magnitude of the simulated point spread functions (PSFs) calculated for line-sharing in the case of three different relaxation rates 500 ms, 750 ms and 1600 ms. It is evident that in the case of higher T_1, the PSF is approximately a delta function. Spectral leakage can be observed in the case of lower T_1s. **(b)** The magnitude of the simulated point spread function (PSF) calculated for GRAPPA in the case of a single coil is shown (PSF is same for the rest of the coils in the array).

Measurement on a human volunteer was performed to test the variation of the T_1 calculations using line-sharing, GRAPPA, line-shared-GRAPPA and other described variations. Figure 3.8, Figure 3.9 and Figure 3.10 show representative line-shared, GRAPPA and line-shared-GRAPPA based *in vivo* T_1 maps of five slices through the human brain of volunteer, respectively.
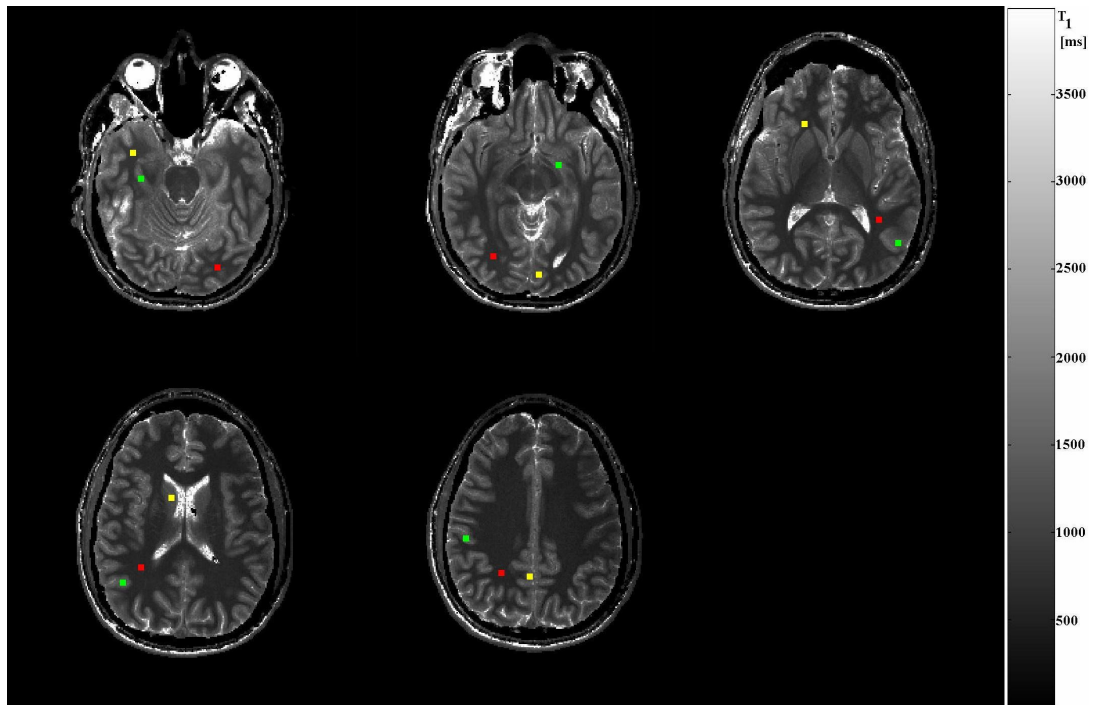
FIG. 3.8. *Line-sharing* applied to TAPIR data acquired with parameters: TR=20 ms, TE=2.5 ms, BW=700 Hz/Px, τ=2000 ms, α=26°, TI=10 ms, 5 slices, 500% slice gap, slice thickness=2 mm, FOV=256 mm x 256 mm, EPI factor=1 and time-points=20, matrix size=256x256. T_1 maps of five slices through the brain of a healthy volunteer are depicted. Three different regions-of-interest are depicted in red (ROI 1), yellow (ROI 2) and green (ROI 3) in each T_1 map.
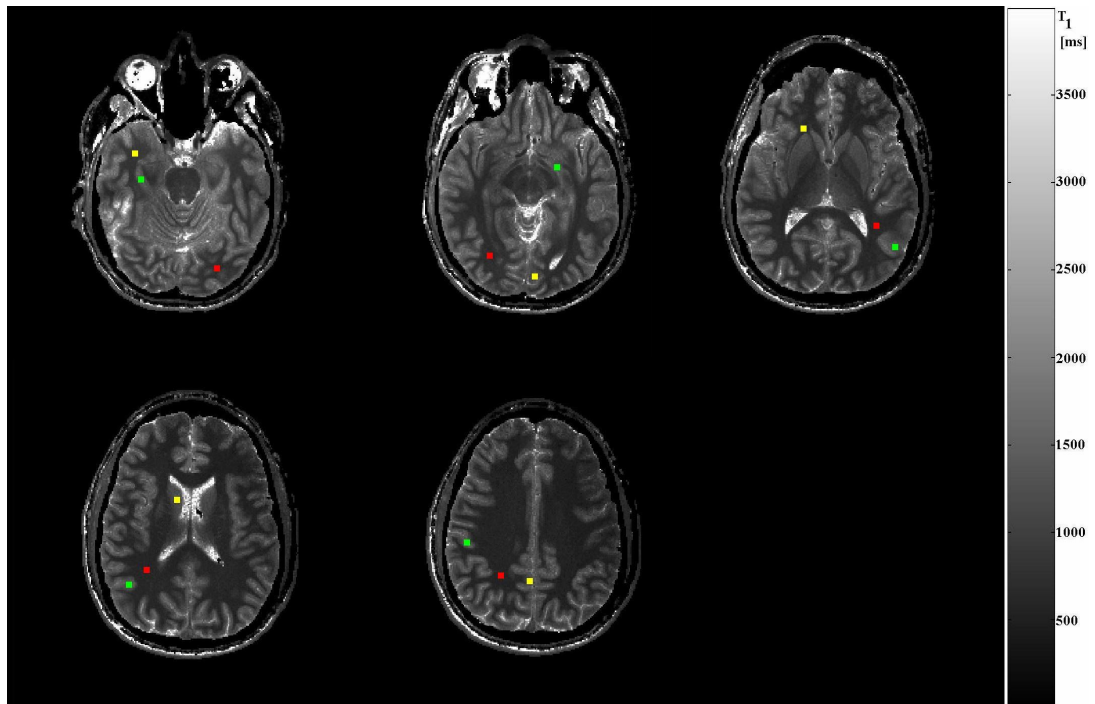
FIG. 3.9. *GRAPPA* applied to TAPIR data acquired with parameters: TR=20 ms, TE=2.5 ms, BW=700 Hz/Px, τ=2000 ms, α=26°, TI=10 ms, 5 slices, 500% slice gap, slice thickness=2 mm, FOV=256 mm x 256 mm, EPI factor=1 and time-points=20, matrix size=256x256. T_1 maps of five slices through the brain of a healthy volunteer are depicted. Three different regions-of-interest are depicted in red (ROI 1), yellow (ROI 2) and green (ROI 3) in each T_1 map.
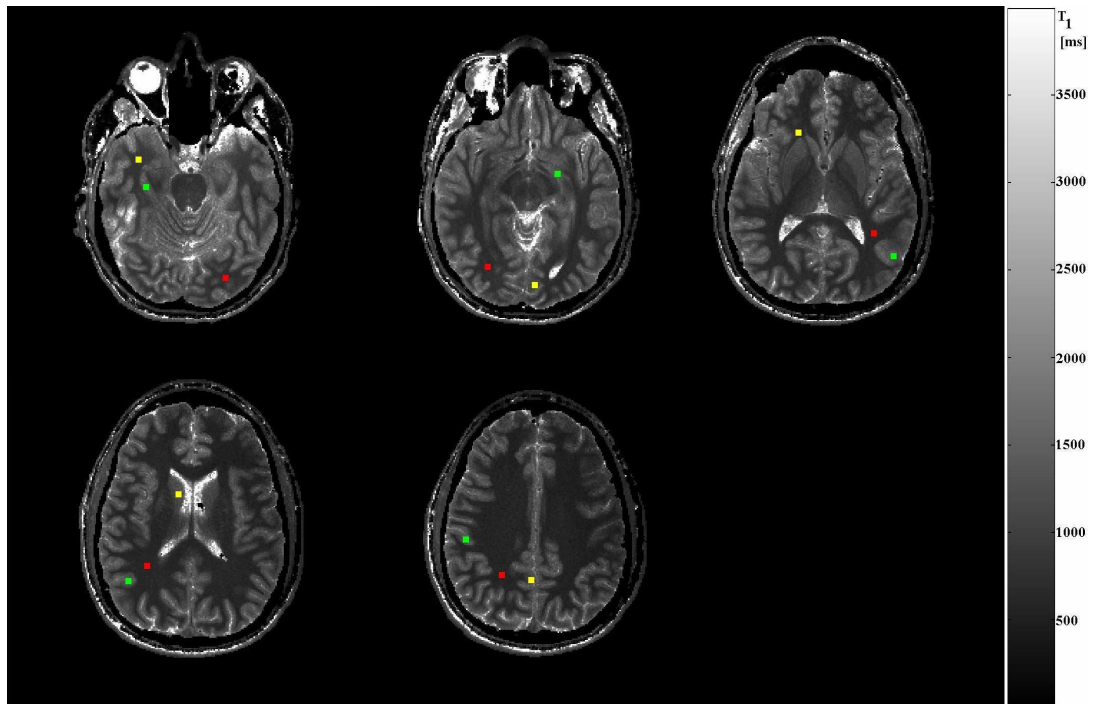
FIG. 3.10. *Line-shared-GRAPPA* applied to TAPIR data acquired with parameters: TR=20 ms, TE=2.5 ms, BW=700 Hz/Px, τ=2000 ms, α=26°, TI=10 ms, 5 slices, 500% slice gap, slice thickness=2 mm, FOV=256 mm x 256 mm, EPI factor=1 and time-points=20, matrix size=256x256. T_1 maps of five slices through the brain of a healthy volunteer are depicted. Three different regions-of-interest are depicted in red (ROI 1), yellow (ROI 2) and green (ROI 3) in each T_1 map.

In Table 3.1, the relative error in T_1 values for the specific tissue types resulting from the line-shared TAPIR method and GRAPPA is given. The original, full TAPIR-based calculations are considered as a reference. It is instructive to compare the performance of the GRAPPA-based T_1 calculations with that of the line-sharing scheme. It is explicitly noted here that the *same* raw data sets were used for T_1 calculations and performance comparison.

For the specific tissue types, i.e., different selected T_1 ranges, mean values of regions with a size of 4x4 voxels of T_1 map of each slice, were calculated. These regions-of-interest (ROIs) are referred as ROI 1, ROI 2, and ROI 3. Table 3.1 depicts the variance of the averaged T_1 values for different ROIs, relevant for *in vivo* T_1 mapping of the human brain using both proposed schemes.

For regions with T_1 less than 1000 ms and between 1000 ms and 2000 ms, the results in Table 3.1 demonstrate good agreement between the reference, the original TAPIR mapped values and those obtained from the line-shared TAPIR mapping. The errors in the T_1 values resulting from both line-sharing and GRAPPA remain below 3%. Hence, both approaches perform well.

Table 3.1. A comparison of the calculated T_1 values for different regions-of-interest in the human brain, denoted as ROI 1, ROI 2, and ROI 3. Each ROI is an average over 4x4 pixels per tissue type. The average T_1 values and percentage differences between the T_1 values obtained from the line-sharing scheme and the basic TAPIR method, fitting 20 time-points along the T_1 recovery curve, are given. For comparison, the average values and the percentage differences between the values obtained from GRAPPA and full TAPIR are also given.

		TAPIR T_1	Line-sharing T_1	% error	GRAPPA T_1	% Error
Slice 1	ROI 1	755±27.60	753.50±34.91	0.19	751.62±43.65	0.44
	ROI 2	873.68±35.05	870.31±45.09	0.38	880.62±41.80	0.79
	ROI 3	1347.62±60.80	1383.81±81.0	2.6	1351.93±74.14	0.31
Slice 2	ROI 1	737.06±34.16	745.87±33.18	1.19	728.56±50.42	1.15
	ROI 2	1108.56±76.06	1107.62±87.09	0.08	1108.50±83.04	0
	ROI 3	1405.62±54.06	1415.37±69.97	0.69	1393.81±104.96	0.84
Slice 3	ROI 1	656±40.643	666±46.59	1.52	668±45.57	1.82
	ROI 2	736.37±48.43	734.87±55.89	0.20	746.81±62.58	1.41
	ROI 3	1305.93±67.50	1303.56±88.47	0.18	1308.25±91.32	0.20
Slice 4	ROI 1	632.62±14.32	630.93±23.82	0.26	638.12±29.27	0.86
	ROI 2	1116.18±50.67	1132.25±71.74	1.43	1114.81±58.28	0.12
	ROI 3	1339.31±69.13	1334.87±82.11	0.33	1330.18±77.66	0.68
Slice 5	ROI 1	583.56±24.38	594.25±28.79	1.83	598.18±34.45	2.50
	ROI 2	1142.56±97.61	1137.43±95.35	0.44	1140.37±101.39	0.19
	ROI 3	1275.81±136.81	1283.87±142.12	0.63	1276.18±140.57	0.02

Table 3.2. A comparison of the relative error of the calculated T_1 values for line-shared-GRAPPA, line-sharing with a factor of 2 and 4, for the same regions-of-interest as in Table 3.1.

		Line-shared GRAPPA T_1	% error	Line-sharing factor-2 T_1	% error	Line-sharing factor-4 T_1	% error
Slice 1	ROI 1	740.93±45.53	1.98	754.87±29.66	0.14	750.06±35.24	0.77
	ROI 2	890.43±59.86	1.91	874.06±38.13	0.04	868.12±55.78	0.63
	ROI 3	1352.06±70.87	0.32	1366.93±79.70	1.43	1386.93±78.03	2.9
Slice 2	ROI 1	733.31±50.75	0.50	730.50±37.61	0.89	737.81±33.43	0.1
	ROI 2	1102.56±86.10	0.54	1106.06±75.93	0.22	1125.06±79.63	1.48
	ROI 3	1394.31±111.94	0.80	1404±65.25	0.11	1422.31±85.43	1.16
Slice 3	ROI 1	657.31±53.51	0.19	664.81±38.96	1.34	654.37±45.96	0.24
	ROI 2	737±70.54	0.08	742±55.20	0.76	705±56.94	4.26
	ROI 3	1327.25±110.00	1.63	1313.50±86.71	0.57	1300.43±84.85	0.42
Slice 4	ROI 1	643.87±32.61	1.77	637.25±18.00	0.73	638.75±20.75	0.96
	ROI 2	1133±88.79	1.50	1124.43±77.58	0.73	1115.75±65.21	0.03
	ROI 3	1349.25±82.39	0.74	1363.43±76.72	1.80	1358.50±72.66	1.43
Slice 5	ROI 1	596.06±37.71	2.14	591.40±27.64	1.34	597.60±29.59	2.40
	ROI 2	1118.68±110.30	2.09	1152.55±90.22	0.87	1146.11±80.32	0.31
	ROI 3	1307.50±142.43	2.48	1275.22±84.81	0	1275.77±91.33	0

In order to simulate the optimisation scenario depicted in Figure. 3.1(c), i.e., the number of slices can be increased in a TAPIR based acquisition at the cost of a decrease in time-points, selected time-points are used in the line-shared and GRAPPA based T_1 calculations. Table 3.3 shows the relative error for the case where every other time-point is used among the 20 sequentially acquired time points. Table 3.4 shows the relative error for the case where every third time-point is used among the 20 sequentially acquired time-points. It is important to note that the reference T_1 values are also different as compared to Table 3.1 for the same ROIs because the accuracy of TAPIR decreases with a decrease in the number of time-points [21], but this change depicts the systematic error due to the reduction in the number of time-points used for the simulation of the optimisation scenario.

Table 3.3. A comparison of the calculated T_1 values for different regions-of-interest in the human brain, denoted as ROI 1, ROI 2, and ROI 3. Each ROI is an average over 4x4 pixels per tissue type. The average T_1 values and percentage differences between the T_1 values obtained from the line-sharing scheme and the basic TAPIR method, considering 10 time-points (after dropping every other time-point to consider optimization) along the T_1 recovery curve, are given. For comparison, the average values and the percentage differences between the values obtained from GRAPPA and full TAPIR are also given.

		TAPIR T_1 (drop 1)	GRAPPA T_1 (drop 1)	% error	Line-sharing T_1 (drop 1)	% error
Slice 1	ROI 1	806.62±64.95	807±78.84	0.14	815.31±50.62	1.07
	ROI 2	956.43±33.91	965.25±78.49	0.92	964.81±56.47	0.87
	ROI 3	1416.81±111.78	1439.93±142.34	1.63	1498.81±160.16	5.78
Slice 2	ROI 1	757.87±37.63	775.5±68.76	2.37	779.25±42.40	2.82
	ROI 2	1155.68±96.90	1155±135.406	0	1167.12±103.00	0.98
	ROI 3	1515.87±91.28	1487.063±239.2	1.84	1533.25±97.82	1.14
Slice 3	ROI 1	649.31±46.71	657.750±74.098	1.29	675.25±54.01	3.99
	ROI 2	688.12±61.64	695.68±77.75	1.09	729.18±68.70	5.96
	ROI 3	1330.25±113.26	1291.87±213.29	2.88	1350±152.49	1.48
Slice 4	ROI 1	637.43±25.31	635.56±42.71	0.29	637.81±30.59	0
	ROI 2	1151.81±72.04	1146.50±94.43	0.46	1159.75±100.80	0.68
	ROI 3	1355.43±82.80	1345.68±111.64	0.71	1393±90.97	2.7
Slice 5	ROI 1	573.87±37.08	573.12±37.19	0.13	590.40±50.60	2.88
	ROI 2	1147.50±111.22	1120.66±115.42	2.33	1181.33±121.54	2.94
	ROI 3	1313.62±152.12	1391.88±176.25	5.95	1371.66±222.61	4.43

Table 3.4. A comparison of the calculated T_1 values for different regions-of-interest in the human brain, denoted as ROI 1, ROI 2, and ROI 3. Each ROI is an average over 4x4 pixels per tissue type. The average T_1 values and percentage differences between the T_1 values obtained from the line-sharing scheme and the basic TAPIR method, considering 7 time-points (after dropping every two time-points to consider optimization) along the T_1 recovery curve, are given. For comparison, the average values and the percentage differences between the values obtained from GRAPPA and full TAPIR are also given.

		TAPIR T_1 (drop 2)	GRAPPA T_1 (drop 2)	% error	Line-sharing T_1 (drop 2)	% error
Slice 1	ROI 1	838.81±59.27	850.31±97.60	1.37	850±63.70	1.37
	ROI 2	1029.43±70.14	1042±88.75	1.22	1014.06±83.63	1.51
	ROI 3	1530.25±137.09	1490.56±148.49	2.59	1694.68±250.89	10.7
Slice 2	ROI 1	839.31±49.14	855.37±77.32	1.91	841.43±69.75	0.25
	ROI 2	1212.43±115.97	1215.12±155.92	0.22	1220.06±164.03	0.62
	ROI 3	1623.18±111.95	1508±163.29	7.09	1648.81±139.44	1.57
Slice 3	ROI 1	725±42.22	687.06±62.00	5.24	704.56±47.29	2.89
	ROI 2	808.50±52.66	775.18±61.47	4.12	762.37±50.67	5.70
	ROI 3	1544.87±161.55	1340.31±216.08	13.2	1363.56±150.47	11.73
Slice 4	ROI 1	683.43±30.48	687.56±45.65	0.60	679.93±49.09	0.51
	ROI 2	1150.81±87.37	1158.87±105.19	0.70	1155.06±106.57	0.36
	ROI 3	1487±132.81	1465.37±172.97	1.45	1490.93±141.83	0.26
Slice 5	ROI 1	624.68±32.03	633.52±36.34	1.41	636.84±37.52	1.94
	ROI 2	1123.55±99.33	1145.22±73.37	1.92	1136.11±66.79	1.11
	ROI 3	1280.66±123.22	1318.77±117.97	2.97	1364.77±184.72	6.56

3.5 Discussion

The proposed line-sharing trajectory inherently samples the centre of k-space densely at each time-point such that the centre of k-space, the keyhole, satisfies the Nyquist sampling rate, whilst the rest of k-space is sparsely sampled. Thereafter, the skipped k-space lines are linearly interpolated by using the preceding and succeeding time-points. This method has the potential to reduce the total acquisition time by 40%. As the additional systematic error for most brain tissue (i.e. grey and white matter) remains significantly below 2-3%, the proposed line-sharing approach offers the possibility to significantly reduce the measurement time without introducing additional significant error components. In principle, the line-sharing method is applicable to relaxation time mapping techniques be they T_1, T_2, or T_2*.

GRAPPA-enhanced T_1 mapping is another approach for reducing the acquisition time and the results are shown in Table 3.1. Furthermore, given the acquisition of a keyhole, the line-sharing method is fully compatible additionally with parallel imaging whereby a further reduction in the number of peripheral lines could be achieved, as confirmed by the results shown in Table 3.2. In the case of line-sharing with factors of 2 and 4, the relative errors remain below 5%, whereas line-shared-GRAPPA has shown better performance because the relative errors remain below 2.5%, as shown in Table 3.2. On the other hand, simulations to analyse optimisation of the time-points and slices has shown relative errors below 4-6% for most of the cases of tissue types with T_1 values around 1000 ms and more than 6% in a few cases of tissue types with T_1 values around 1500 ms or more, as shown in Table 3.3 and Table 3.4.

The line-sharing method is proposed to accelerate the process of data acquisition for T_1 mapping using TAPIR. Keyhole-based methods have been used in past to increase the temporal resolution in cardiac cine imaging [26], functional MRI [27], and perfusion studies [28]. In particular, the line-sharing method is able to deal with some problems that arose in the previous keyhole-based techniques when a large number of phase-encode lines are skipped to achieve higher acceleration. First, if all the truncated k-space phase-encode lines are copied from a reference k-space, a blurring effect on the reconstructed images is produced [20]. The implicit advantage in the line-sharing method is that there is no apparent loss in the high-frequencies of the reconstructed

image and no apparent blurring effect. This is because the temporal separation of the data that are shared between the time-points is very small (100 ms). Another problem is that if the skipped k-space lines are replaced by the lines from a single reference k-space [20], this leads to an inaccurate calculation of the missing data. There is variation between the k-space data acquired at different time-points due to T_1-weighting. Line-sharing alleviates this problem because the method provides improved calculation of the missing data by interpolating the preceding and succeeding time-points.

The difference between the original time-point and line-shared time point can be thought of as an addition of the systematic error to the corresponding missing k-space lines. This k-space error is projected onto the reconstructed time-point image by the Fourier transform. According to the Parseval's theorem, the error energy in the reconstructed time-point image is proportional to the error energy in the corresponding k-space. Consequently, the error energy present in the reconstructed time-point images affects the line-shared T_1 map. The relative error values signify the artefact energy present in the line-shared T_1 maps. It is important to note that further increase in the keyhole size can suppress the error energy.

TAPIR is superior to IR snapshot-FLASH and IR-EPI in terms of higher sampling density along the recovery curve. Line-sharing facilitates the advantage of further increase in sampling in the fixed time frame allowed to sample the recovery curve. Furthermore, a finer sampling density of the recovery curve results in a sharper point spread function and a concomitant reduction in image blurring. If, however, the error between the shared lines in k-space is high enough to distort the point spread function, it will lead to ghost artefacts and image blurring. Faster relaxing recovery curves are more prone to produce errors in line-sharing. The precision of the method for T_1 mapping is expected to increase with increasing field (longer T_1), where the interval of highest variation – and thus highest error for interpolation - on the relaxation curves is sampled with a larger number of points. This latter issue is a particular strength of the line-sharing approach for TAPIR.

3.6   Conclusions

The method to acquire data rapidly for the TAPIR sequence presented here has resulted in the T_1 maps of acceptable quality (relative errors remain below 3%), without losing spatial and temporal resolution. With regard to medical applications (human brain imaging with a τ of 2 sec, for instance) a typical acquisition time of the TAPIR sequence can be further reduced by up to 40% using the line-sharing approach. Implementation of the line-shared TAPIR sequence on a state-of-the-art scanner would deliver whole-brain coverage in clinically acceptable times. In addition to that, the concept of sharing the k-space lines can be extended to sharing the k-space bands and combining line-sharing with the parallel imaging.

3.7   References

1. Vrenken H, Geurts JJ, Knol DL, Noor van Dijk L, Dattola V, Jasperse B, A. van Schijndel RA, Polman CH, Castelijns JA, Barkhof F, Pouwels PJW. Whole-brain T_1 mapping in multiple sclerosis: Global changes of normal-appearing gray and white matter. Radiology 2006;240:811–820.

2. Shah NJ, Neeb H, Zaitsev M, Steinhoff S, Kircheis G, Amunts K, Häussinger D, Zilles K. Quantitative T_1 mapping of hepatic encephalopathy using magnetic resonance imaging. Hepatology 2003;38:1219–1226.

3. Look DC, Locker DR. Time saving in measurement of NMR and EPR relaxation times. Rev. Sci. Instr. 1970;41: 250-251.

4. Crawley AP, Henkelman RM. A comparison of one-shot and recovery methods in T_1 imaging. Magn Reson Med 1988;7:23–34.

5. Ordidge RJ, Gibbs P, Chapman B, Stehling MK, and Mansfield P. High-speed multislice T_1 mapping using inversion recovery echo planar imaging. Magn Reson Med 1990;16: 238–245.

6. Gowland P, Mansfield P. Accurate measurement of T_1 *in vivo* in less than 3 seconds using echo-planar imaging. Magn Reson Med 1993. 30: 351-354.

7. Haase A. Snapshot FLASH MRI. Application to T_1, T_2, and chemical-shift imaging. Magn Reson Med 1990;13:77–89.

8. Hardy PA. Measuring T_1 with a segmented Look Locker technique. Proc SMRM 1997;5:2064.

9. Lee JH. PURR-TURBO: A novel pulse sequence for longitudinal relaxographic imaging. Magn Reson Med 2000;43:773–777.

10. Markley JL, Horsley WJ, Klein MP. Spin-lattice relaxation measurements in slowly relaxing complex spectra. J. Chem Phys 1971;55:3604–3605.

11. Brix G, Schad LR, Deimling M, Lorenz WJ. Fast and precise T_1 imaging using a TOMROP sequence. Magn Reson Imag 1990;8:351–356.

12. Pickup S, Wood AKW, Kundel HL. A Novel method for analysis of TOMROP data. J Magn Reson Imag 2004;19:508–512.

13. Mason GF, Chu WJ, and Hetherington HP. A general approach to error estimation and optimised experiment design, applied to multislice imaging of T_1 in human brain at 4.1T. J Magn Reson 1997;126:18–29.

14. Shah NJ, Steinhoff S, Zaitsev M. Pulse train, nuclear magnetic resonance tomograph and imaging method. US-Patent: 6,803,762 B2, Oct. 12, 2004.

15. Shah NJ, Zaitsev M, Steinhoff S, Zilles K. A new method for fast multislice T_1 mapping. NeuroImage 2001;14:1175–1185.

16. Hsu JJ, Glover GH. Rapid MRI method for mapping the longitudinal relaxation time. J Magn Reson 2006;181:98–106.

17. Ropele S, Bammer R, Stollberger R, Fazekas F. T_1 maps from shifted spin echoes and stimulated echoes. Magn Reson Med 2001;46: 1242-1245.

18. Zhu DC, DP Richard. Full-brain T_1 mapping through inversion recovery fast spin echo imaging with time-efficient slice ordering. Magn Reson Imag 2005;54:725–731.

19. Van Vaals JJ, Brummer ME, Dixon WT. "Keyhole" method for accelerating imaging of contrast agent uptake. J Magn Reson Imag 1993;3:671–675.

20. Wheaton AJ, Borthakur A, and Reddy R. Application of the keyhole technique to T_{1p} relaxation mapping. J Magn Reson Imag 2003;18:745–749.

21. Zaitsev M, Steinhoff S, Shah NJ. Error reduction and parameter optimization of the TAPIR method for fast T_1 mapping. Magn Reson Med 2003;49: 1121-1132.

22. Jakob PM, MA Griswold, Edelman RR, Sodickson DK. AUTO-SMASH: A self calibrating technique for SMASH imaging. Magn Reson Mater in Physics, Biology and Medicine 1998;7: 42–54.

23. Heidemann RM, Griswold MA, Haase A, Jakob PM. VD-AUTO-SMASH imaging. Magn Reson Med 2001;45: 1066–1074.

24. Griswold MA, Jakob PM, Heidemann RM, Nittka M, Jellus V, Wang J, Kiefer B, Haase A. Generalized autocalibrating partially parallel acquisitions. Magn Reson Med 2002;47: 1202–1210.

25. Ji JX, Bum Son J, Rane SD. PULSAR: A Matlab toolbox for parallel magnetic resonance imaging using array coils and multiple channel receivers. Magn Reson Med 2007;31B: 24-36.

26. Suga M, Matsuda T, Komori M, Minato K, Takahashi T. Keyhole method for high-speed human cardiac cine MR imaging. J Magn Reson Imag 1999;10:778–783.

27. Gao JH, Xiong J, Lai S. Improving the temporal resolution of functional MR imaging using keyhole techniques. Magn Reson Med 1996;35:854–860.

28. Oesterle C, Strohschein R, Kohler M, Schnell M, Hennig J. Benefits and pitfalls of keyhole imaging, especially in first-pass perfusion studies. J Magn Reson Imag 2000;11:312–323.

Chapter 4
Development of a Method for Rapid In-Plane Motion Estimation for MR Images

4.1 Introduction

Patient motion results in a significant reduction of image quality and diagnostic information. Rigid body motion can be predominantly due to rotation and translation of the patient's head in response to pain, discomfort, or tremor, for instance. Motion affected k-space data produce artefacts in the reconstructed image. Applying retrospective correction schemes [1], [2] or determining the magnitude and direction of motion during scanning and reacquiring the data accordingly [3] are possible approaches to correct for rigid body motion.

In this work, a technique is proposed for in-plane, rigid body motion estimation by registering low-resolution images, termed implicit navigator images, that are inherent to the acquired MR images. Most MR image registration techniques are applied either in the Fourier domain or in the spatial domain. Fourier domain methods are based on phase correlation for translation estimation and the log-polar Fourier transform for rotation estimation [4]. Another method is based on using the pseudo-log-polar Fourier Transform for image registration [5]. On the other hand, spatial domain techniques are based on an iterative method where correlations between images for every possible angle are calculated followed by an optimisation procedure [6]. Although Fourier-based methods are robust to noise, image intensity variations, and have low computational complexity, the interpolation errors in calculating the log-polar Fourier transform are problematic. Generally, the phase correlation technique in the log-polar Fourier domain is used to calculate the rotation between the reference navigator image and the remaining navigator images. In such a Fourier transform dependent scheme, rotations are reduced to translations on the polar grid and can be recovered by phase correlation.

Mathematically, the polar grid computation uses the FFT algorithm whereas interpolation for computing the polar FFT is inaccurate. In this work, in-plane rotation estimation is performed by applying the PPFT (Pseudo-Polar Fourier Transform) to the navigator images. This technique, introduced in [7], is advantageous because it requires neither interpolation nor iterative correlations to calculate rigid body rotation. For the first time, in the present work, the proposed method has been applied to the MR images acquired at the high magnetic field. It is elegant because the imaging data themselves act as navigators.

Additionally, in this work, the translation estimation is performed using singular value decomposition of the phase correlation matrix, which is a robust and rapid method. In general, the in-plane displacement values can be determined by finding the peak of the inverse Fourier transform of the phase correlation matrix. The method employed in this work is based on the fact that the phase correlation matrix, computed from shifted replicas of the same image, is a separable rank-one matrix. In the case of the phase correlation matrix, computed from consecutive images of a time-series, the translation estimation problem is stated as finding the rank-one approximation to that matrix. This can be achieved by using singular value decomposition (SVD) followed by the identification of the left and right singular vectors. Hence, the linear phase coefficients corresponding to the vertical and horizontal displacements are identified in the left and right vectors, respectively [8].

In some applications of EPI, such as fMRI, each radiofrequency excitation has to be repeated several times to reacquire the same image in order to satisfy some statistical constraints and therefore motion between different radiofrequency excitations can be source of serious artefacts. Since the central k-space region i.e., keyhole, mainly influences SNR and contrast, its utilisation has long been the focus for functional and cardiac MRI methods. Sequences that acquire data from the centre to the periphery of the k-space in multiple-shot acquisitions, such as projection reconstruction, spiral and PROPELLER (Periodically Rotated Overlapping Parallel Lines with Enhanced Reconstruction), reduce motion artefacts by utilising the oversampled non-Cartesian central k-space region. The central non-Cartesian region of k-space is acquired in each shot and can be used to obtain a low-resolution navigator image [9]. Registering the

low-resolution images acquired in each acquisition allows estimation of the in-plane rotation and translation between the images.

The rapid motion estimation technique proposed has been applied to the images acquired using the EPI sequence on a 3T Trio system (Siemens Medical Systems, Erlangen, Germany). Simulations were employed to determine the accuracy and precision of the method. In this work, only the method to determine the magnitude and direction of motion is presented; methods to fully compensate the artefacts, for example, rotation generated local undersampling, non-equidistant data and ill-conditioning of the reconstruction problem, are not considered.

4.2 Theory

Involuntary rigid body motion during the MRI scan may cause two main types of artefacts; the artefacts that arise as a result of tissue displacement during the quiescent period between each data sampling period and the following RF excitation (inter-view effect), and the artefacts that arise as a result of the phase induced by motion during the readout (intra-view effect). Single shot or multi-shot techniques, which traverse the whole k-space after a single or a few radiofrequency excitations, respectively, are especially vulnerable to motion. In cases where data acquisition is fast enough to freeze inter-shot motion, the motion corrupted k-space data can be corrected by some retrospective techniques or at the least severity of the artefact can be measured and depending on that, corrupted data can be reacquired, rejected or corrected.

Simple rigid body motion can be analysed in two forms. Translational motion produces a linear phase shift in k-space along the direction of motion. A rotation in image space produces same rotation in k-space. In this section, first the rotation estimation technique that computes the pseudo-polar Fourier transform and then calculates a function, termed ADF (Angular Difference Function), is explained. The ADF is defined as the integral, along the radial axis, of the spectral difference of the navigator images [7]. It is important to note that the spectral difference is the difference

between the pseudo-polar Fourier transforms of the navigator images. Thereafter, subspace analysis of the phase correlation matrix to estimate the in-plane translation is explained.

4.2.1 In-Plane Rotation Estimation

Due to the rotational motion, the k-space data on the sampling grid are rotated by the same angle resulting in a rotated image. In order to compensate for rigid-body rotation effects, the acquired k-space data must be counter-rotated by an angle estimated before alignment. Specifically, if the rotation occurred predominantly in the image plane, then the reconstructed image should be the rotated replica of the reference image. This relationship can be represented as:

$$F_1\left(k_x, k_y\right) = F_2\left(k_x \cos \theta_0 + k_y \sin \theta_0, -k_x \sin \theta_0 + k_y \cos \theta_0\right) \tag{4.1}$$

where F_1 is magnitude of the reference k-space, F_2 is the magnitude of the rotated k-space and θ_0 is the angle by which it is rotated.

According to traditional Fourier-based rotation estimation schemes, the Fourier magnitude data of each image are interpolated on the polar grid and the rotation angle is calculated using one dimensional phase correlation between the polar Fourier values of images to be registered along the angular axis. The accuracy of the rotation angle calculation is dependent on the Fourier values resampled on the polar grid, which are approximated by interpolation. In contrast, the pseudo-polar Fourier transform is immune to such approximation errors. Mathematically, discretisation in the polar coordinates can be represented by the following relation:

$$P\left(m, n\right) = F\left(r_m \cos \theta_n, \, r_n \sin \theta_n\right) \tag{4.2}$$

where P represents the k-space data F sampled on a polar grid and $r_m=0,\ldots,M$-1, $r_n=0,\ldots,N$-1, $\theta_n=2\pi n/N$, M and N represents the number of samples on the radial and angular axes, respectively. Instead of polar coordinates, a transition from Cartesian coordinates to the pseudo-polar coordinates can be performed according to:

$$P_a\left(m,n\right)= F'\left(\frac{-2mn}{N},n\right) \tag{4.3}$$

$$P_b\left(m,n\right)= F'\left(n,\frac{-2mn}{N}\right) \tag{4.4}$$

where F' is the Cartesian k-space representation whose coordinates are linearly transformed to the pseudo-polar coordinates, $m=-N,\ldots,N$, $n=-N/2,\ldots,N/2$, P_a depicts the vertical coordinates and P_b denotes the horizontal coordinates. In terms of a radial and angular representation:

$$P_a\left(r_{m_a},\theta_{n_a}\right)= P_a\left(m,n\right) \tag{4.5}$$

$$P_b\left(r_{m_b},\theta_{n_b}\right)= P_b\left(m,n\right) \tag{4.6}$$

where the variables are given as:

$$r_{m_a} = r_{m_b} = m\sqrt{\left(\frac{2n}{N}\right)^2+1} \tag{4.7}$$

$$\theta_{n_a} = \frac{\pi}{2}-\arctan\left(\frac{2n}{N}\right) \tag{4.8}$$

$$\theta_{n_b} = \arctan\left(\frac{2n}{N}\right) \tag{4.9}$$
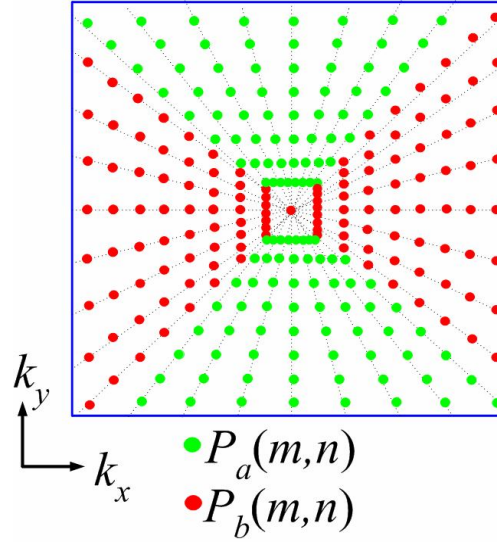
FIG. 4.1. The pseudo-polar k-space domain, where P_a denotes the vertical coordinates and P_b denotes the horizontal coordinates.

It is evident from Figure 4.1 that the samples on each ray in the pseudo-polar domain are equally spaced but this spacing is different for different angles. Another important fact is that this grid is unequally spaced in the angular direction but has equally spaced slopes. Further details regarding computation of the pseudo-polar Fourier transform are given in [10].

Given that a reference and a rotated navigator image are transformed to the pseudo-polar Fourier domain and are represented by P_2 and P_1, respectively, the in-plane rotation relationship can be given as:

$$P_1(r,\theta) = P_2(r,\theta+\Delta\theta) \tag{4.10}$$

A difference function using $P_1(r,\theta)$ and $P_2(r,\theta)$ is defined as:

$$\Delta P'(\theta) = \int_0^\infty \left| P_1(r,\theta) - P_2(r,-\theta) \right| dr \tag{4.11}$$

The radial variable r can be integrated out and thus a difference function is discretised as:

$$\Delta P(\theta_i) = \sum_{-N \leq m \leq N} |P_1(r_m, \theta_i) - P_2(r_m, \theta_i)| \Delta r_m \qquad (4.12)$$

where the range of θ_i is $[0, \pi]$ and Δr_m is the step size. The normalised form of this equation can be written as:

$$\Delta P(\theta_i) = \frac{\sum_{-N \leq m \leq N} \left(P_1'(r_m, \theta_i) - P_2'(r_m, \theta_i)\right)^2}{\sigma_{P_1} \sigma_{P_2}} \qquad (4.13)$$

where P_1' and P_2' are defined according to:

$$P'(r_m, \theta_i) = P(r_m, \theta_i) - \frac{\sum_{-N \leq k \leq N} P(r_k, \theta_i)}{2N} \qquad (4.14)$$

Moreover, the standard deviations, σ_{P_1} and σ_{P_2} in equation (4.13) are defined as:

$$\sigma_{P'} = \sqrt{\frac{\sum_{-N \leq m \leq N} \left(P(r_m, \theta_i) - P'(r_m, \theta_i)\right)^2}{2N}} \qquad (4.15)$$

where $P' = P_1$ or $P' = P_2$. It is important to note that ΔP is a minimum if one of the following two cases is valid:

$$\theta_i + \Delta \theta = -\theta_i \qquad (4.16)$$

$$\theta_i + \Delta \theta = -\theta_i + \pi \qquad (4.17)$$

Hereafter, an angular difference function is defined as:

$$\Omega(\theta_i) = \Delta P(\theta_i) + \Delta P(\theta_{i+2N+1}) \qquad (4.18)$$

where $2N+1$ is size of the pseudo-polar grid and image is of size N x N. Hence, the angle of rotation can be computed from the angle corresponding to the minimum of Ω:

$$\Delta\theta = 2\theta_i \qquad\qquad (4.19)$$

The complete procedure of navigator image registration is shown in Figure 4.2.
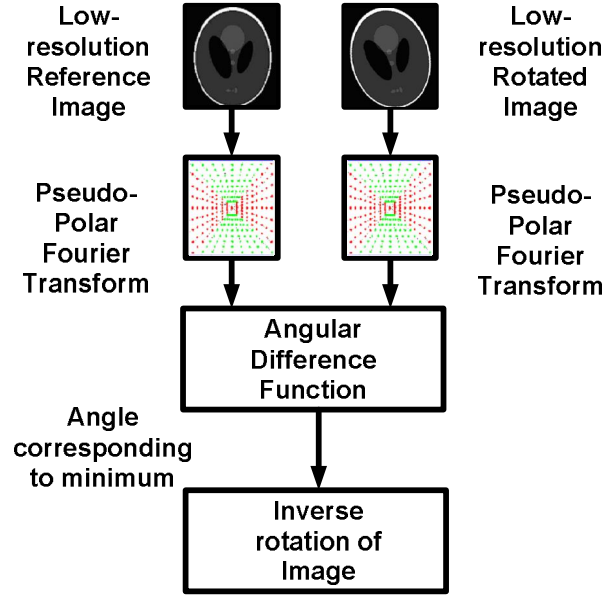
FIG. 4.2. Processing scheme for the pseudo-polar *k*-space domain based rapid in-plane rotation estimation process is depicted.

4.2.2 In-Plane Translation Estimation

According to Fourier transform theory, a linear phase shift in the *k*-space produces a translation in the image space. Mathematically, translation produced in the image can be represented as:

$$d(x-\Delta x, y-\Delta y) \Leftrightarrow D(k_x, k_y)\, e^{i2\pi(k_x \Delta x + k_y \Delta y)} \qquad\qquad (4.20)$$

where $d(x$-$\Delta x, y$-$\Delta y)$ represents the translation affected image, $D(k_x, k_y)$ is the *k*-space of the reference image, whilst Δx and Δy are the displacements to be estimated in the horizontal and vertical directions, respectively. In the literature, several phase

correlation methods are given [11], [12] to estimate the relative translation between images. The phase correlation matrix is realised by calculating the normalized cross power spectrum of a reference *k*-space and a translation-affected *k*-space. Let the normalised cross power spectrum be represented as *M*:

$$M = \frac{D(k_x, k_y) \cdot [\ D(k_x, k_y)\ e^{i2\pi(k_x \Delta x + k_y \Delta y)}\ ]^*}{|\ D(k_x, k_y) \cdot [\ D(k_x, k_y)\ e^{i2\pi(k_x \Delta x + k_y \Delta y)}\ ]^*\ |} \tag{4.21}$$

where $D(k_x, k_y)$ is the *k*-space of the reference navigator image and $D(k_x, k_y)\ e^{i2\pi(k_x \Delta x + k_y \Delta y)}$ is the *k*-space of the translated navigator image. Thus, the phase of the normalized cross power spectrum forms a plane in k_x and k_x :

$$\sphericalangle M = \Delta x\, k_x + \Delta y \cdot k_y \tag{4.22}$$

where $\sphericalangle M$ is the phase of the normalized cross power spectrum. The coefficients Δx and Δy, representing integer or non-integer shifts, can be estimated by fitting a plane using the linear least-squares method [13]. It is important to emphasize here that, as cited in [11], regular least-squares fitting is difficult in such a translation estimation approach because it requires fitting a plane to the noisy phase difference data. Another method proposed in [8] suggests that the dimensionality of the least-squares fitting can be reduced through a subspace identification of the phase correlation matrix *M* defined earlier. According to the proposed method, let the two vectors be defined as:

$$p(k_x) = e^{i\Delta x k_x} \tag{4.23}$$

$$q(k_y) = e^{-i\Delta y k_y} \tag{4.24}$$

Using the vectors given above, the problem of finding the integer or non-integer displacements between two images can be formulated as finding the rank-one approximation of the normalized phase correlation matrix *M*. The rank-one subspace of *M* can be obtained through the singular value decomposition (SVD) method. Consequently, the linear phase coefficients, Δx and Δy, can be identified independently in the left and right singular vectors of *M*, respectively. Using a given singular vector, *v*,

and the unwrapped phase of the singular vector, Φ, the set of normal equations are given as:

$$R\,[\mu\;c]^{T} = \Phi \qquad\qquad (4.25)$$

where the rows of R are equal to $[r,1]$, $r=\{0,1, 2, . . ., (s-1)\}$, s=length of v, μ and c are the slope and abscissa of the fitted line, respectively. The solution of the set of normal equations can be found by applying the linear least-squares method to the unwrapped phase of v, i.e., Φ:

$$[\mu\;c]^{T} = (R^{T}R)^{-1}R^{T}\Phi \qquad\qquad (4.26)$$

The slope of the fitted line, μ, maps to the translational shift. In the case of $v=p(k_x)$, μ equals Δx and in the case of $v=p(k_y)$, μ equals Δy. The identification of one-dimensional singular vectors of M is an implicit eigen-filtering approach. Furthermore, the one-dimensional phase unwrapping employed in this method is relatively less complicated than a two-dimensional phase unwrapping of the matrix M. Nevertheless, the fitting accuracy depends on the linearity of the unwrapped phase vector. The complete process is depicted in Figure 4.3.
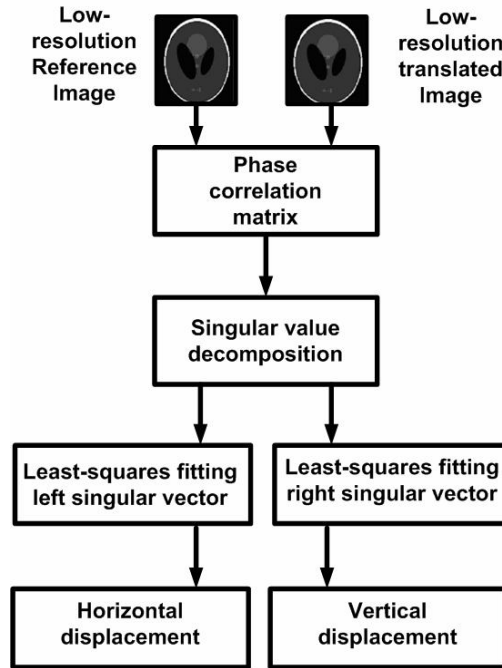
FIG. 4.3. A schematic representation of the extended phase correlation matrix approach used to estimate translation between the navigator images.

4.3 Methods

4.3.1 Simulations

An image was selected among the EPI images obtained from a human volunteer. Synthetic motion affected image data were generated with the use of inverse rigid body motion operations on the selected reference image. These images were generated by means of the built-in image rotation function in MATLAB and a Fourier-based image shift operation. The rotation function used here is based on a bicubic convolution method to resample the rotated voxel on the Cartesian grid. The translation operation employed the Fourier shift theorem. Thereafter, the reference image and the motion-affected image underwent 2D FFT and the simulated motion affected k-space data were generated. The main advantage of in-plane motion estimation as described here is that the low-resolution navigator images can be reconstructed using keyhole. To validate the proposed motion estimation approach, the square region around the centre of the keyhole was selected from the simulated reference k-space and the motion corrupted k-space. A low-resolution image was obtained from the reference keyhole termed the

reference navigator image. Thereafter, rotation and translation estimations were performed using the navigator images. Finally, inverse rotation and inverse translation operations were performed on the simulated images using the estimated motion parameters.

Registration accuracy depicts the overall positional mismatch between the registered (motion-corrected) image and the original image. Precision determines the deviation of the calculated rotation and translation parameters from the original ones. In order to estimate the registration accuracy and precision as a function of navigator resolution, navigator images were rotated and translated along the horizontal and vertical directions with different values. A total number of 121 equi-spaced angles were selected over a range of $\pm15°$ to simulate rotation. The 128x128 pixel image had a FOV of 23.7x23.7 cm^2. Thus, the extent of each pixel was 1.8x1.8 mm^2. A total number of 87 equi-spaced points were selected over a range of ±8.75 pixels, in both x- and y-directions, to simulate translation. An EPI image, free of any rotation or translation, served as a reference image. Random noise generated in MATLAB was added to the images such that the signal-to-noise ratio (SNR) was 5 dB, 10 dB, and 15 dB. Thereafter, motion estimation was performed and the estimated in-plane motion parameters were compared with the true motion parameters applied by linear regression. Here, the correlation coefficient and the standard deviation of the rotation and translation calculated from the regression line are used to represent the accuracy and precision of the in-plane navigator registration, respectively.

4.3.2 *In Vivo* Experiments

Time-series of images of a single healthy volunteer were obtained on a 3T whole-body system (Siemens, Erlagen, Germany) using the EPI sequence. The sequence parameters for scan were as follows: TR=3000 ms, TE=54 ms, BW=2170 Hz/Px, slice thickness 5 mm, FOV=237 mm x 237 mm, NEX=15 and matrix size 128x 128. The volunteer was asked to not move at the start of the experiment and to perform in-plane movement of his head during the course of later measurements. Both large and small-scale rigid body motion of the volunteer affected the resulting images.

At the post-processing stage, the corresponding *k*-spaces were obtained by applying the inverse Fourier transform to the images. For the selected slices, the low-resolution navigator images were obtained by using the central 32 x 32 phase-encode lines of the *k*-spaces. Due to in-plane motion, the navigator images were also rotated or translated accordingly. The third navigator image was selected as a reference and the others were aligned to it. The pseudo-polar Fourier transform of each of the navigator images was obtained by using the MATLAB toolbox provided in [10]. Computation of the pseudo-polar Fourier Transform is based on the Chirp Z-transform and that method is described in detail in [10]. The angular resolution in the pseudo-polar coordinates was 4x256 and the resolution of a single ray was also 4x256. The angular difference function defined earlier was implemented in MATLAB and the minimum of the angular difference function, that corresponds to the angle of rotation, was calculated. Thereafter, the translation estimation method was applied as outlined in the theory section. All calculations were performed using MATLAB.

4.4 Results

Table 4.1 depicts the simulation results to assess the navigator resolution effects on the accuracy and precision of the in-plane motion estimation. It is worth noting that the correlation coefficient, R, remains between 0.75 and 0.95 in all cases. This result provides evidence that the simulated motion is estimated with high accuracy. The precision of the method is evaluated through the standard deviation, σ, of the differences between the detected rotations and translations and the corresponding regression line; this is within an acceptable range (less than 1.5 pixels). In the case of rotation estimation, it is evident from the simulation results that an increase in the SNR improves the accuracy and precision of the method.

A time-series of images of a slice through the human brain is shown in Figure. 4.4 a-n. In each figure, the reference image and the motion-affected image are shown in first row; the registered image and the difference between the reference image and the registered image are shown in the bottom row. The corresponding estimated in-plane motion parameter values are shown in Figure 4.5.

Table 4.1. Correlation between the simulated and estimated rotations and translations is given. Standard deviation of the differences calculated through linear regression is also given. The correlation is represented as R and standard deviation is represented as σ. The standard deviation of the differences (measured-regression) of the translations are given in units of pixels and the standard deviation of the differences (measured-regression) of the rotations are given in degrees. X and Y are translations in the *x*-axis and *y*-axis direction, respectively. Θ is the rotation and is given in degrees.

	SNR [dB]		Keyhole 16x16 [pixels]	Keyhole 32x32 [pixels]	Keyhole 64x64 [pixels]
X	5	R	0.9854	0.7495	0.8325
		σ	0.1127	1.5652	1.3326
	10	R	0.9965	0.9962	0.8505
		σ	0.0461	0.0432	1.2777
	15	R	0.9995	0.9999	0.9486
		σ	0.0183	0.0003	0.8066
Y	5	R	0.9606	0.7900	0.9045
		σ	0.4849	1.4667	0.9988
	10	R	0.9992	0.9679	0.9308
		σ	0.0340	0.1542	0.8398
	15	R	0.9998	0.9990	0.9789
		σ	0.0083	0.0238	0.4593
Θ	5	R	0.9648	0.9788	0.9752
		σ	0.8242	0.6237	0.7065
	10	R	0.9970	0.9979	0.9993
		σ	0.0444	0.0276	0.0121
	15	R	0.9997	0.9997	0.9997
		σ	0.0997	0.0398	0.0270

(a)

(b)

(c)

(d)

(e)

(f)

(g)

(h)

(i)

(j) (k) (l)

(m) (n)
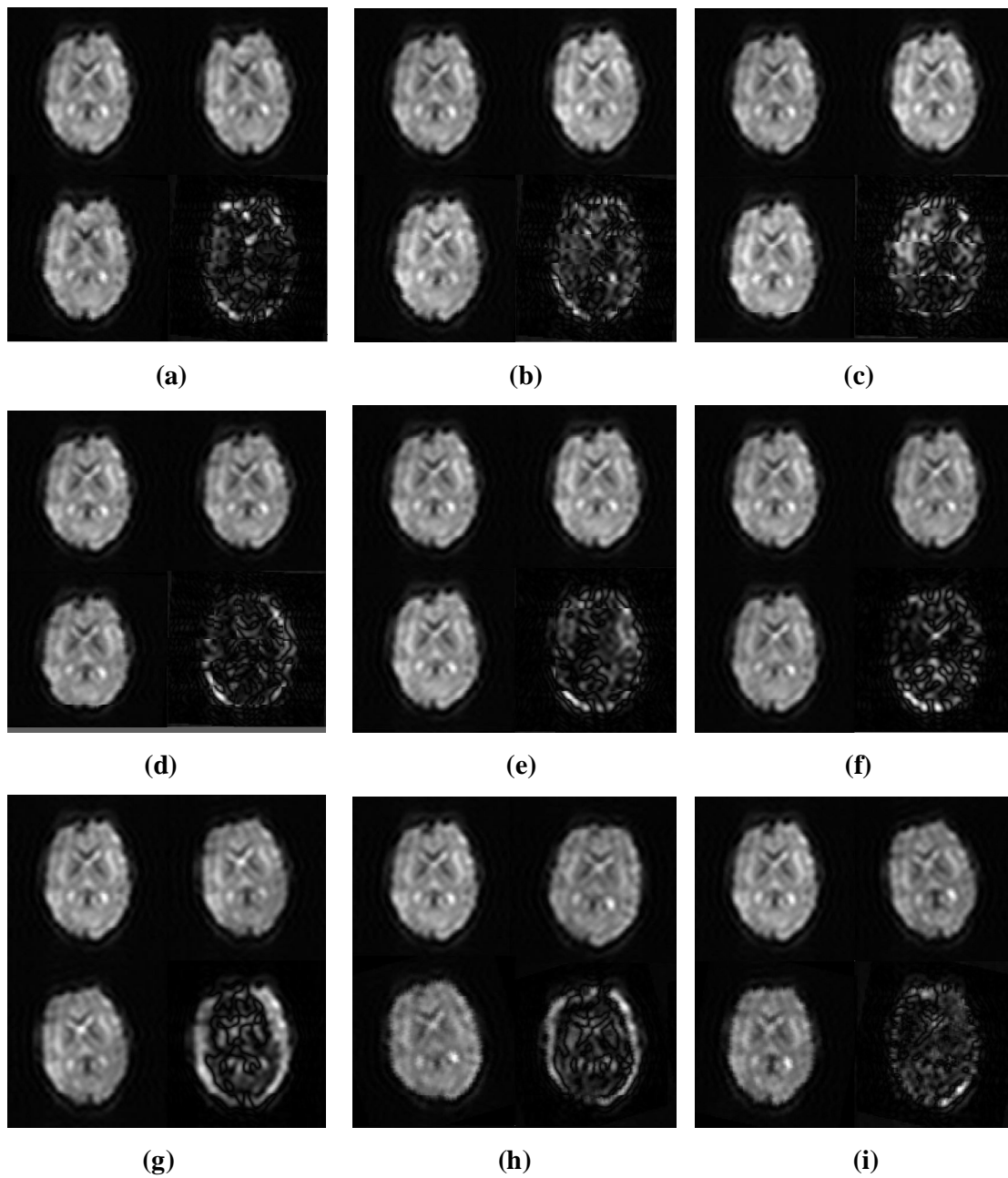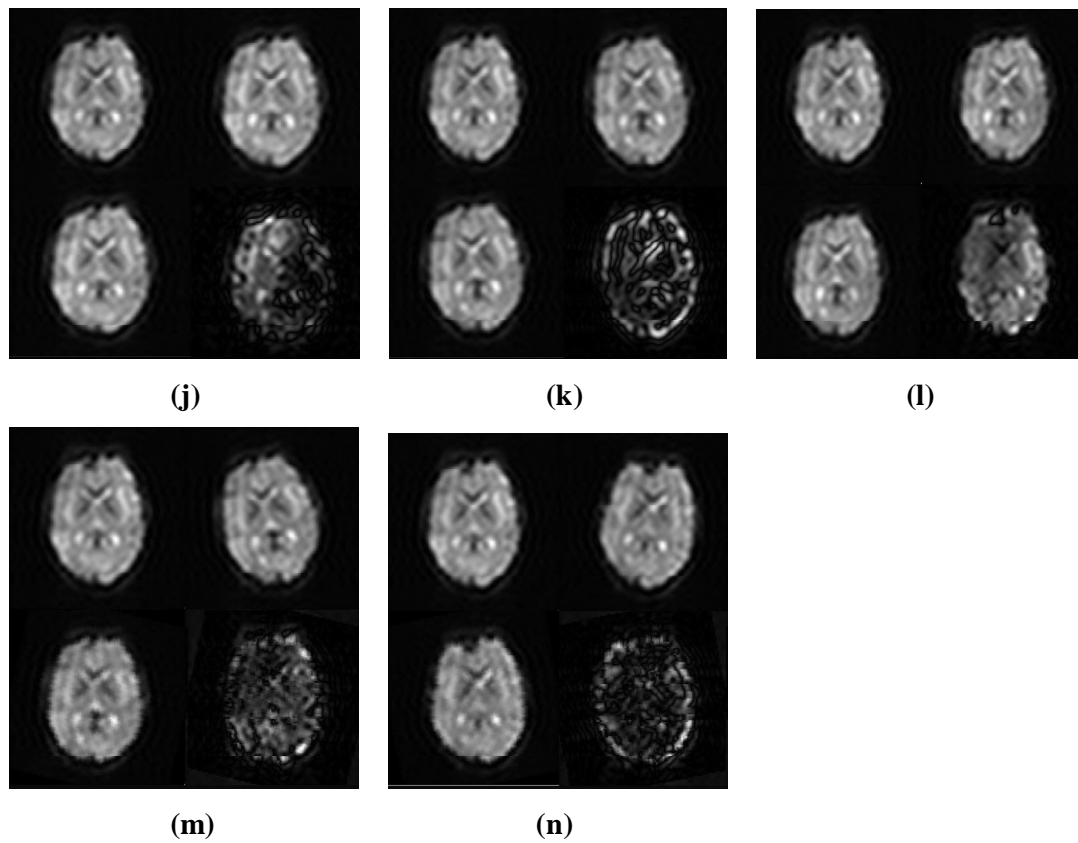
FIG. 4.4. (a)-(n). The rotated images, reference images, registered images and the corresponding angular difference functions of a representative slice obtained during the multiple EPI acquisitions in the same scan. In each figure, the reference image and rotated image are shown in the first row, whilst the registered image and the difference between the reference image and the registered image are shown in the second row.
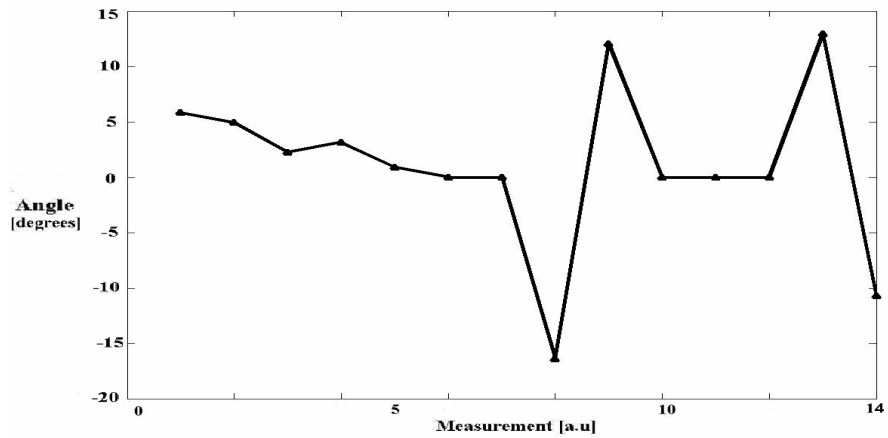
(a)
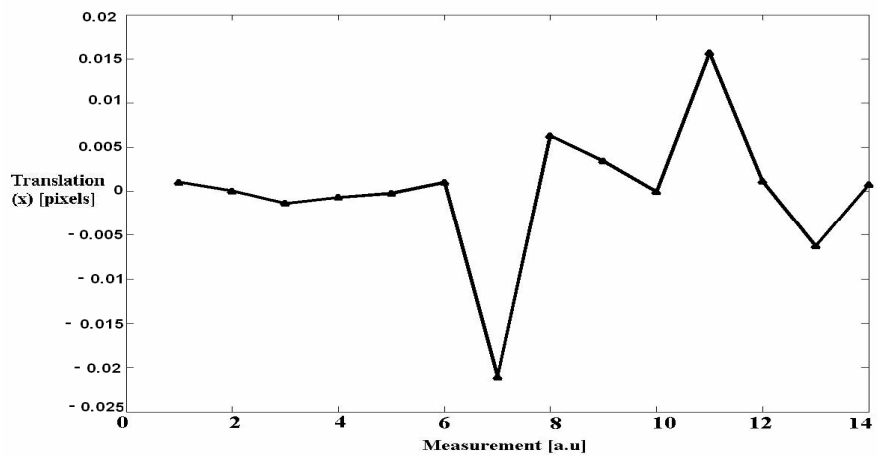
(b)
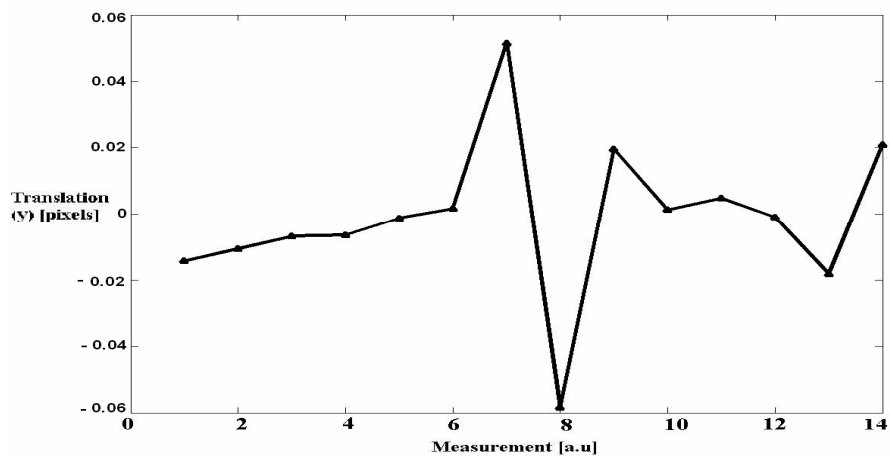
(c)

FIG. 4.5. (a). In-plane rotation angle values estimated using the described approach are shown, corresponding to Figure 4.4. Estimated In-plane translation values in the direction of x-axis and y-axis are shown in **(b)-(c)**, respectively. The estimated pixel values are normalised by the image size in single dimension i.e., 128.

4.5 Discussion

During the course of long MRI scans, the possibility of patient movement due to discomfort inside the scanner is not negligible. Sometimes, such a problem leads to repeat performance of the scan again to obtain artefact free data. Repeated examinations are not desired due to the inevitable increase in scanning costs and scan time, which in turn create further discomfort for the patient. Therefore, motion correction is a fundamental tool to perform scans to obtain artefact-free images without creating unnecessary patient discomfort. In real-time applications, time is a crucial factor for selection of a method for motion correction among the several methods proposed in past. The whole process of motion correction can be decomposed in two stages: estimation and correction. Accelerated motion estimation can further reduce the time required for the whole motion correction process.

This work provides a framework to extract the motion parameters from navigator images. In this study, a rapid method was applied to obtain the rotational and translational in-plane motion parameters. Performance of the method to estimate rigid body motion parameters with different noise levels and different experimental conditions was evaluated using computer simulations. EPI acquired data were used to test the method *in vivo*. Low-resolution, two-dimensional navigator images were used to estimate the motion.

To estimate the rotation, the presented method relies on the pattern matching between the the reference navigator image and the time-series images in the pseudo-polar Fourier domain. Such a pattern matching is performed using the angular difference function defined earlier. The efficacy of the method is dependent on the fast Fourier transform of the navigator image on a pseudo-polar grid that is independent of interpolation. The computation of the pseudo-polar grid is accurate. In addition, because calculation of ADF is non-iterative, this enhances the angle estimation speed further. Although computation of the ADF is rapid, estimation robustness is dependent on the size of the pseudo-polar grid. The accuracy of the rotation estimation method is of the order of the angular sampling resolution. As noise and differences between the navigator image and the image to be registered increases, the shape of ADF is prone to change. In comparison, the robustness of the spatial domain co-registration approaches

is based on a parameter search using cost function optimisation, which is a time consuming procedure. In the case of translation estimation, a low-complexity subspace identification technique was applied to the phase correlation matrix of the navigator images by exploiting the fact that the phase correlation matrix is of rank one. As manifested in the results, this method is robust due to the dependence on the identification of the dominant singular vectors of the phase correlation matrix and one-dimensional phase unwrapping of the vectors. Besides rapid co-registration, the advantage of the low-resolution navigator images is their robustness as most of the signal is encoded in the low-frequency region of k-space from which the navigator images are reconstructed.

The advantages of the image registration approach proposed here are two-fold. First, the suitability of the method for the real-time implementation is facilitate by the fact that the so-called keyhole data, which are acquired anyway, are utilised. Second, the proposed techniques can also be employed to perform image alignment at the off-line post-processing stage after acquiring data.

The particular strength of the pseudo-polar domain based angle estimation scheme is that it is less sensitive to noise as compared to the polar coordinates based scheme. Similarly, for the translation estimation method, the advantage is that noise filtering is inclusive in the process of determining the dominant rank-one subspace of the phase correlation matrix.

A potential difficulty for the motion estimation scheme described here is the extent of through-plane motion that affects the image intensity and structure resulting in the differences between the navigator images. In this case, the effects can be observed in the poor performance of the ADF. In particular, spin history effects can reduce the motion parameters estimation quality. However, it was observed that the scheme proposed in this work is not perfectly resilient to through-plane motion effects. This is manifest in the results where the reference navigator image and the motion affected navigator image are not exactly similar due to through-plane motion. It has been shown in Figure. 4.4. g, h and k that through-plane motion deleteriously affects in-plane motion estimation. The reason is that the navigator images are no longer rotated or translated replicas of each other in the case of significant through-plane motion.

Therefore, in the case of higher degrees of through-plane motion, the in-plane motion estimation techniques are not able to detect the motion parameters accurately. Nevertheless, the proposed motion estimation techniques have potential for improvement to deal with such adverse affects to some extent. For example, the ADF can be low-pass filtered in order to detect the angle of rotation between non-similar images. Similarly, the phase correlation matrix can be masked first, and then the singular value decomposition approach can be applied on the matrix to identify the translation parameters.

4.6 Conclusions

A rapid in-plane motion parameters estimation method was presented that utilises low-resolution navigator images. The presented method estimates the in-plane rotation by computing an angular difference function in the pseudo-polar Fourier domain using the navigator images. The method has the same complexity as the Fourier transform and therefore it has great potential for real-time implementations. Application of the pseudo-polar Fourier transform and the angular difference function for rotation correction in MRI is a useful approach. This scheme is well designed because it is based on the Cartesian data set used to reconstruct the low-resolution images. This enables better motion estimation as compared to the radial or spiral data sets that are sensitive to interpolation errors and off-resonance effects. MR sequences that traverse a Cartesian trajectory in multiple shots are suited for such a scheme because each low-resolution image from a single shot can be used as a quick snapshot that saves the motion information. fMRI is another application where rapid in-plane rotation detection is crucial. It is important to mention that in the EPI acquisitions, severe movements of head can disturb the slice positioning and therefore the images to be registered are not the pure rotated replicas of each other. Consequently, the images might have different intensities and might have some non-common parts. In such a situation the angular difference function does not compute the exact rotation angles. This function has to be extended to mitigate for such effects; this is currently being investigated. The amount of motion-induced sub-pixel image translation is estimated by means of singular value decomposition of the phase correlation matrix of the navigator images. The proposed scheme has low computational complexity and is therefore suited for the real-time applications.

4.7 References

1. Atkinson D, Hill DL. Reconstruction after rotational motion. Magn Reson Med 2003;49:183–187.

2. Bydder M, Atkinson D, Larkman DJ, Hill DL, Hajnal JV. SMASH navigators. Magn Reson Med 2003;49:493–500.

3. Thesen S, Heid O, Mueller E, Schad LR. Prospective acquisition correction for head motion with image-based tracking for real-time fMRI. Magn Reson Med 2000;44:457–465.

4. Reddy BS, Chatterji BN. An FFT-based technique for translation, rotation, and scale-invariant image registeration. IEEE Transactions On Image Processing 1996;Vol. 5.:No. 8.

5. Liu H, Guo B, Feng Z. Pseudo-log-polar Fourier transform for image registration. IEEE Signal Processing Letters 2003;Vol. 13.:No. 1.

6. Bammer R, Aksoy M, Liu C. Augmented generalized SENSE reconstruction to correct for rigid body motion. Magn Reson Med 2007;57:90–102.

7. Keller Y, Shkolnisky Y, Averbuch A. The angular difference function and its application to image registration. IEEE Transactions On Pattern Analysis and Machine Intelligence 2005;27:969–976.

8. Hoge WS. A subspace identification extension to the phase correlation method. IEEE Transactions On Medical Imaging 2003;22:277–280.

9. Pipe JG. Motion correction with PROPELLER MRI: application to head motion and free-breathing cardiac imaging. Magn Reson Med 1999;42:963–969.

10. Averbuch A, Coifman RR, Donoho DL, Elad M, Israeli M. Fast and accurate polar Fourier transform. Applied and Computational Harmonic Analysis. 2006;21:145–167.

11. Foroosh H, Zerubia JB, Berthod M. Extension of phase correlation to subpixel registration. IEEE Transactions On Image Processing 2002;11:188–200.

12. Kuglin CD, Hines DC. The phase correlation image alignment method. Proc. IEEE Conf. Cybernatics Society;Sept. 1975:163–165.

13. Maas LC, Frederick B, Renshaw P. Decoupled automated rotational and translational registration for functional MRI time series data: the DART registration algorithm. Magn Reson Med 1997;37:131-139.

Chapter 5
A Method for Processing Phased-Array Line-Shared Data for Rapid Relaxation Rate Mapping

5.1 Introduction

Application of phased arrays in MRI has not only improved the SNR but has also led to the emergence of numerous rapid image acquisition strategies. Phased-array systems are advantageous because a large volume can be imaged with a higher SNR. In addition, the number of coils employed in the phased-array determines an incremental factor for the acquisition speed. Roemer et al. [1] have described the first so-called phased-array coil to acquire MR images. Other ideas proposed to employ multiple detectors for MRI are summarised in [2], [3], [10].

Parallel imaging techniques have emerged as the main applications of phased-array systems. Owing to the advent of new phase encoding methods together with the improved gradient coil systems, several parallel imaging techniques have been proposed in past, such as SENSE (Sensitivity Encoding for Fast MRI) [4] and the so-called SMASH (Simultaneous Acquisition of Spatial Harmonics) imaging [5]. Nowadays, phased-array MR imaging has become a major focus of research and phased-arrays with up to 128 elements have been manufactured and used for MRI experiments.

Among the several proposed methods for image combining, the so-called "sum-of-square" (SOS) method is the most common. It has been shown in [6] that the SOS method results asymptotically in the same SNR as in maximum ratio combining (known as optimal linear combining), which can only be used when the coil sensitivities are perfectly known. In [1], spatial matched filtering was used to combine multi-coil images. According to an adaptive phased-array combining method, proposed in [7], the weights for each coil are derived using data correlation estimates from each coil based

on a stochastic signal model. This method can be used to reduce image artefacts such as ghosting, for example. Specifically, 'noise' statistics near the source of artefact can be used to null the ghost artefacts through the adaptive phased-array combining method. Although, the range of the spatial null is rather broad in this method i.e., the ghost spacing is relatively large as compared to the effective width of the individual coil sensitivity profile [8].

In the case of the line-sharing method explained in Chapter 3 and applied to the mapping of a T_1 recovery curve, the phase and amplitude errors between the line-shared and acquired echoes at each time-point may generate FOV/2 ghost artefacts in the reconstructed images. The phased-array combining method is advantageous because it is immune to ghost artefacts, despite the fact that it depends on the extent of the spatial null. In the case where the spatial null is not so broad, i.e., ghosts are closely spaced and the sensitivities of individual coils overlap, a method known as sensitivity encoding (SENSE) can be applied to diminish the ghost artefacts [8]. However, this technique utilises the full FOV images. In particular, the conventional parallel imaging method, SENSE, mitigates the FOV/2 ghosts in the aliased and reduced FOV images. However, in the method employed here, "SENSE" is applied directly to the full FOV images. Application of full FOV SENSE is based on constrained optimisation, which optimises the SNR subject to the constraint of nulling the ghost artefacts at the known locations. Phased-array combining that optimises SNR, subject to nulling constraints, is also known as the generalized side-lobe canceller. Originally, that method was shown to be beneficial for noninterleaved multishot EPI for the elimination of in-plane flow problems, off-resonance distortions, and delay misalignment and in addition to that, it can replace echo-time-shifting [8]. In the work presented here, this method is applied to eliminate the possible FOV/2 ghosts in the line-shared time-point images used for T_1 mapping.

5.2 Theory

According to the method proposed in [1] to combine the multi-coil images, spatial matched filtering is the optimal method (a method is termed optimal when it maximises the SNR of the composite image). Let the noise correlation matrix be

represented as $\mathbf{R}_n^{-1}$, a matched filter for a given pixel location in a coil, c, is computed as:

$$\mathbf{a}_c = \mathbf{R}_n^{-1} \mathbf{m}_{xy} \tag{5.1}$$

where the magnitude and phase of the transverse magnetic field, created by each coil at a given pixel location, is represented by a complex valued vector $\mathbf{m}_{xy}$. Spatial matched filtering can be performed by applying a filter vector $\mathbf{a}_c$ to combine the N complex coil images, $\mathbf{I}_c(x, y)$, into a single image $\mathbf{I}(x, y)$:

$$\mathbf{I}(x, y) = \sum_{c=1}^{N} \mathbf{a}_c^* \mathbf{I}_c(x, y) \tag{5.2}$$

It is important to emphasize that the filter vector $\mathbf{a}_c$ can vary as a function of the spatial coordinates (x, y). It is difficult to obtain *a priori* knowledge of the complex near-field sensitivity for each coil to calculate the vector $\mathbf{m}_{xy}$ in clinically acceptable times. Therefore, the coil sensitivity vector $\mathbf{m}_{xy}$ is estimated by the complex individual coil image values at each pixel. Hence, the practical matched filter formulation consists of the square root of the sum of the squared individual coil magnitude images, the sum-of-squares, and can be written as:

$$\mathbf{I}(x, y) = \sqrt{\sum_{c=1}^{N} \left(\mathbf{I}_c(x, y) \right)^2} \tag{5.3}$$

It is evident from above that noise correlations are ignored in the SOS approach. Therefore, the filtered estimate $\mathbf{I}(x, y)$ is biased by noise as the SNR decreases.

Another reconstruction technique based upon the stochastic formulation of the matched filter, where both signal and noise processes are represented in terms of their second-order coil correlation statistics, is given in [7]. In this method, an optimisation formula calculates a filter vector that produces the maximum expected SNR for the

corresponding signal and noise statistics. A phased-array receiver j samples a stochastic signal process, denoted by $p(t)$, and a stochastic noise process, denoted by $n(t)$. Let the coil correlation matrices for the signal and noise processes be represented by $\mathbf{R}_s$ and $\mathbf{R}_n$, respectively:

$$\mathbf{R}_s(i, j) = E[p_i(t)p_j^*(t)] \tag{5.4}$$

$$\mathbf{R}_n(i, j) = E[n_i(t)n_j^*(t)] \tag{5.5}$$

where $i = 1 \dots N$ and $j = 1 \dots N$ represent the coil indices in the phased-array, N is the total number of coils, t is time and E is the mathematical expectation operator. Consider the following matrix product:

$$\mathbf{K} = \mathbf{R}_n^{-1}\mathbf{R}_s \tag{5.6}$$

The proof of this equation is given in [9]. The eigenvector corresponding to the maximum eigenvalue of the matrix product $\mathbf{K}$ is the filter vector that produces the maximum SNR. Practically, the expectation values given in the equations (5.4) and (5.5) are evaluated over two-dimensional image spaces instead of time. These expectation values are calculated by averaging cross products of the coil images over a region-of-interest in FOV, the correlation statistics can be derived as:

$$\hat{\mathbf{R}}_s(i, j) = \sum_{ROI}\mathbf{I}_i(x, y)\mathbf{I}_j^*(x, y) \tag{5.7}$$

where $\hat{\mathbf{R}}_s$ is the estimate of $\mathbf{R}_s$ and ROI denotes the set of pixel coordinates used for estimation. In case where $\mathbf{R}_s$ is estimated over a single pixel only and $\mathbf{R}_n$ is assumed to be equal to identity matrix, the matched filter converges to the standard sum-of-squares defined in equation (5.3).

The phased-array method provides a general model to represent the effect of the ghost artefacts on each pixel [8]. In the experimental set-up of the phased-array as a

receiver coil, let the sensitivity map of the i-th coil be represented as $s_i(x, y)$ and the desired alias-free image be represented as $f(x, y)$. The ghosts can be considered as the superimposed images i.e., if an image contains N_g ghosts, it corresponds to N_g+1 superimposed images, spatially spaced by a distance denoted as D. In this case, the point spread function, $h_n(x, y)$, is the complex weight of the n-th ghost arising from the signal at (x, y). Assuming that the FOV/2 ghosts in the images may be caused due to the amplitude and phase errors between the phase-encode lines, the following equation may be used to model the method:

$$\begin{bmatrix} r_1(x,y) \\ r_2(x,y) \\ \vdots \\ r_N(x,y) \end{bmatrix} = \begin{bmatrix} s_1(x,y) & \cdots & s_1(x,y-N_gD) \\ s_2(x,y) & \cdots & s_2(x,y-N_gD) \\ \vdots & & \\ s_N(x,y) & \cdots & s_N(x,y-N_gD) \end{bmatrix} \times \begin{bmatrix} h_0(x,y)f(x,y) \\ \vdots \\ h_{N_g}(x,y-N_gD)f(x,y-N_gD) \end{bmatrix} + \begin{bmatrix} n_1(x,y) \\ n_2(x,y) \\ \vdots \\ n_N(x,y) \end{bmatrix} \qquad (5.8)$$

where $r_i(x, y)$ is the reconstructed pixel value for i-th coil, $i=1,\ldots,N$ and $n_i(x, y)$ is the observation noise. Although this equation is valid for N coils, eight receiver coils are used in the work presented here. In the matrix notation:

$$\mathbf{r}(x, y) = \mathbf{S}(x, y)\,\mathbf{f}(x, y) + \mathbf{n}(x, y) \qquad (5.9)$$

where the matrix $\mathbf{S}(x, y)$ and vectors $\mathbf{r}(x, y)$, $\mathbf{f}(x, y)$ and $\mathbf{n}(x, y)$ in equation (5.9) are in direct correspondence with equation (5.8). Considering the case where the number of coils is greater than the number of ghosts, N_g, and the ghost spacing D and the complex coil sensitivities (B_1 maps) $s_i(x, y)$ are known, the least-squares estimate of $\mathbf{f}(x, y)$ can be written as:

$$\hat{\mathbf{f}}(x, y) = [\mathbf{S}(x, y)^{\mathbf{H}}\,\mathbf{R}_n\,\mathbf{S}(x, y)]^{-1}\,\mathbf{S}(x, y)^{\mathbf{H}}\,\mathbf{R}_n^{-1}\,\mathbf{r}(x, y) \qquad (5.10)$$

where $\mathbf{R}_n$ is the noise covariance matrix, the superscript $\mathbf{H}$ denotes the conjugate transpose. The values of the vector $\hat{\mathbf{f}}(x, y)$ i.e. $h_{N_g}(x, y - N_gD)\,f(x, y - N_gD)$ are weighted and shifted values of the original image $\mathbf{f}(x, y)$. It is important to note here

that the individual values of the vector $\hat{\mathbf{f}}(x, y)$ are point spread function weighted. Assuming that the ghost spacing D is known, spatially aligning and combining the values of $\hat{\mathbf{f}}(x, y)$ from all coils can provide an improved estimate of the original image and ghost interference can be suppressed.

It is evident from equation (5.10) that estimation of the coil sensitivity matrix $\mathbf{S}$ is an important factor. Although, the coil sensitivities can be estimated by a pre-scan calibration, such an approach may potentially increases the total acquisition time. Therefore, in order to estimate the sensitivities of the individual coils, coil correlation matrices are computed from the individual low-resolution coil images by averaging cross products of the complex low-resolution image over the FOV. It is important to note that the low-resolution coil images are obtained from the keyhole data. Correlation statistics can be computed according to the relationship described in equation (5.4). Evaluated at a single point in space, the signal correlation matrix can be written as

$$\hat{\mathbf{R}}_s = \mathbf{m}_{xy}\mathbf{m}_{xy}^{\mathbf{H}} \tag{5.11}$$

where $\hat{\mathbf{R}}_s$ is a rank-one projection whose eigen decomposition yields a single eigenvector with an associated non-zero eigenvalue. This single, nontrivial solution is a scaled version of $\mathbf{m}_{xy}$, the coil sensitivity at a given point in space.

In this work, the SOS method and phased-array ghost artefact elimination method explained above were applied to the T_1-weighted, line-shared images from which T_1 maps were subsequently reconstructed.

5.3 Methods

In order to compare the T_1 values delivered by the line-sharing scheme applied to the k-space of each coil and the combined k-space, imaging of a phantom containing water was performed. Five experiments were performed using the water phantom, initially distilled and afterwards doped with Gd-DTPA (Diethylenetriaminepentaacetic

Acid). The T_1 maps were calculated in each experiment. The concentration of Gd-DTPA was gradually increased to decrease T_1 in each experiment. The TAPIR sequence was used and the measurement parameters were: TR=150 ms, TE=2.5 ms, BW=700 Hz/Px, α=30°, slice=1, slice thickness=2 mm, matrix size=256 x 256, EPI factor=1. The line-sharing scheme was applied to each k-space obtained from the 8-channel receiver and to the k-space corresponding to the single image, separately. As the T_1 decreased, the periodic phase and amplitude errors between k-space lines increase and this resulted in visible ghost artefacts in the time-point images. SOS was used to combine images from the different coils. Additionally, the phased-array ghost elimination method described in the theory section was applied to minimise the ghost artefact distortions in the line-shared images obtained using the TAPIR sequence. It is important to mention that the noise correlation matrix was assumed to be identity matrix, i.e. $\mathbf{R}_n^{-1} = \mathbf{I}$.

After obtaining the T_1 maps, the mean of three different regions-of-interest in the same range of T_1 values was calculated for each experiment. The reproducibility of the T_1 values delivered by the line-sharing method using multi-coil k-spaces, single k-space and phased-array processing was compared.

Phased-array processing was applied to line-shared TAPIR data acquired on a 4T system with parameters: TR=20 ms, TE=2.5 ms, BW=700 Hz/Px, τ=2000 ms, α=26°, TI=10 ms, 500% slice gap, slice thickness=2 mm, FOV=256 mm x 256 mm, EPI factor=1 and time-points=20, matrix size=256x256, 5 slices. The phased-array processing method was applied to the individual time-points of the first slice followed by the T_1 mapping procedure.

5.4 Results

The line-shared T_1 maps, using single k-space, multi-coil k-space and phased-array   processed k-space are shown in Figure 5.1a-e, where the T_1 maps shown in Figure 5.1a depicts the slowest T_1 relaxation rates and T_1 maps shown in Figure 5.1e depicts the fastest T_1 relaxation rates used in the experiments. The relative errors between the original T_1 maps and line-shared T_1 maps, using multi-coil k-space, single k-space and phased-array processed k-space are shown in Figure 5.2. An average T_1 value

of three different region-of-interests in each T_1 map was calculated and then the relative error was obtained, as shown in Figure 5.2.

The phased-array processed T_1 map of the first slices through the brain of a healthy volunteer is depicted in Figure 5.3. Three different regions-of-interest are depicted in red (ROI 1), yellow (ROI 2) and green (ROI 3) in the T_1 map. Each ROI is composed of 4x4 pixels. The original mean T_1 values were: 755 ms in ROI 1, 873.68 ms in ROI 2 and 1347.62 ms in ROI 3. In the case of phased-array processed T_1 values were: 762.87 ms in ROI 1, 886.87 ms in ROI 2 and 1360.5 ms in ROI 3. Hence, the relative error in ROI 1 was 1.04%, in ROI 2 was 1.5% and in ROI 3 was 0.95%.
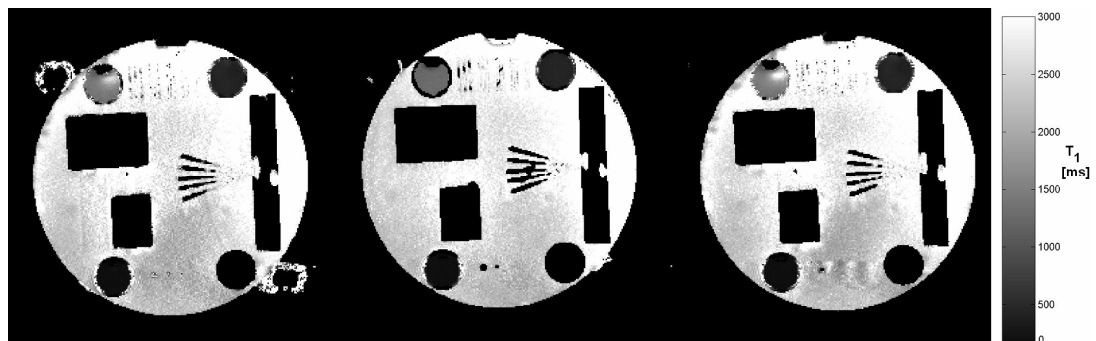
(a)
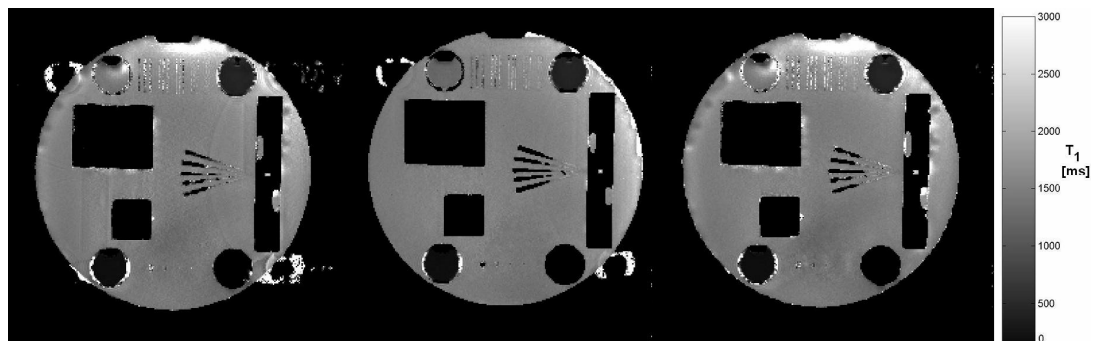
(b)

(Figure continued on next page....)
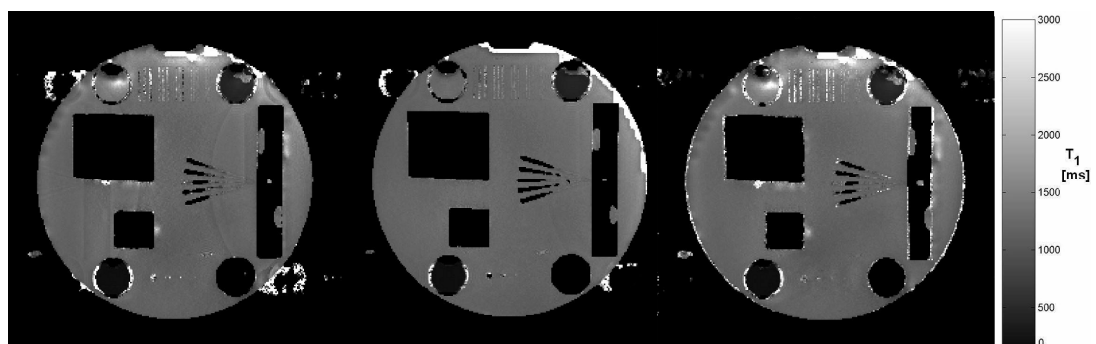
(c)
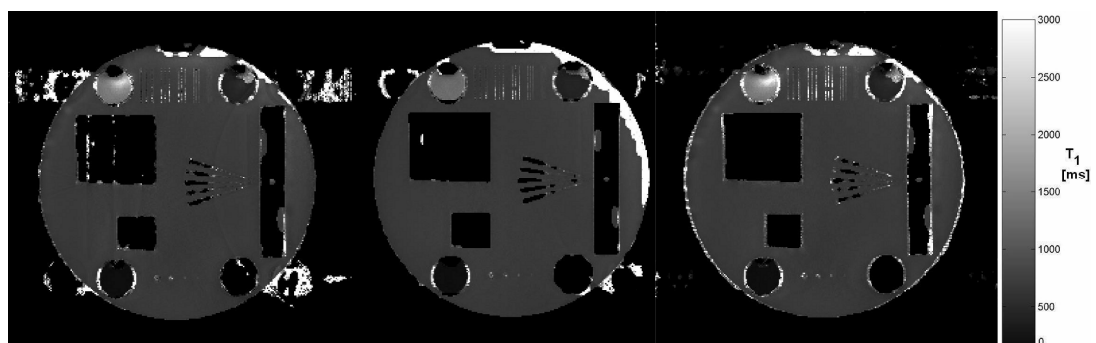
(d)
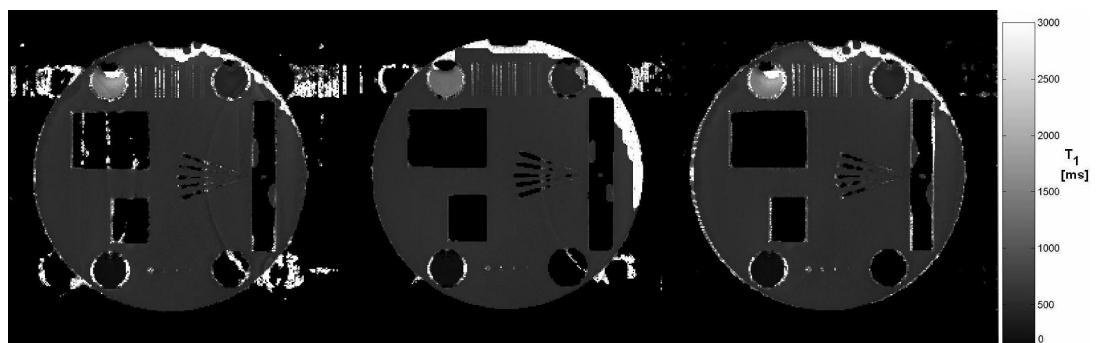
(e)

FIG. 5.1. Line-shared T_1 maps using single k-space (shown in the first column), the SOS method (shown in the second column) and the phased-array processing method (shown in the third column) are depicted in **(a)-(e)**. The slowest relaxation rate is depicted in **(a),** whereas fastest relaxation rate is shown in **(e)**. The exact ranges of relaxation rates used are shown in Figure 5.2.
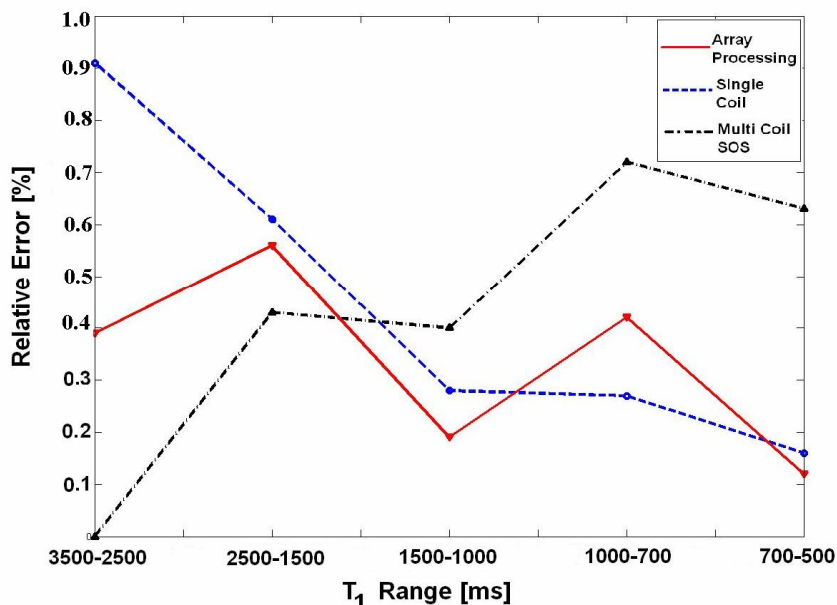
FIG. 5.2. Comparison of the relative errors in line-shared T_1 maps obtained by using the single k-space (shown by the blue line), multi-coil k-space (shown by the black line) and phased-array processing (shown by the red line).
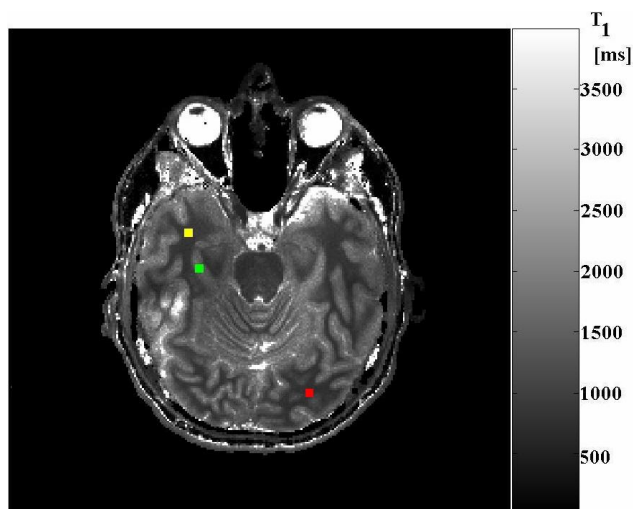
FIG. 5.3. Phased-array processing applied to line-shared TAPIR data acquired on a 4T system with parameters: TR=20 ms, TE=2.5 ms, BW=700 Hz/Px, τ=2000 ms, α=26°, TI=10 ms, 500% slice gap, slice thickness=2 mm, FOV=256 mm x 256 mm, EPI factor=1 and time-points=20, matrix size=256x256, 5 slices (single slice result is shown). T_1 map of the first slices through the brain of a healthy volunteer is depicted. Three different regions-of-interest are depicted in red (ROI 1), yellow (ROI 2) and green (ROI 3) in the T_1 map.

5.5 Discussion

The results described above compare the utility of phased-array processing of multi-coil k-space and single-coil k-space for line-shared T_1 mapping. The calculations show that the performance of multi-coil line-sharing is better than that of single k-space line-sharing for the T_1 ranges above 1500 ms. The relative error in the case of multi-coil line-sharing increases with the decreasing T_1 values. In comparison, however, the relative error in the case of phased-array processing remains lower than the single-coil k-space line-sharing for the T_1 ranges above 1000 ms. The difference between the relative errors is not significant for the T_1 ranges between 1000 ms and 2000 ms.

The efficacy of the phased-array processing method is limited by certain factors such as the number of coils, sensitivity maps and the loss in SNR due to ill-conditioning of the inverse solution in equation (5.10). In particular, noise amplification of inverse solution in equation (5.10) causes significant loss in SNR. Instead of the assumption $\mathbf{R}_n^{-1} = \mathbf{I}$ used in this work, the measurement of actual noise statistics can bring further improvement in the results, but such an approach increases the total scan time. Instead of the coil sensitivity estimation using the low-resolution images obtained from the keyhole data, reference images without distortions can be obtained in a separate scan and then coil sensitivities can be derived. The improved sensitivity estimation method can increase the suppression of artefacts. Other limiting factors are the number and spacing of nonzero point spread values that may be nulled by the phased-array processing method [8]. Closely spaced point spread function values produces ill-conditioned inverse solution of equation (5.10) and the solution has better conditioning in the case of relatively few widely spaced point spread values, since the relative coil sensitivities vary considerably at wider distances [8]. The phased-array processing method peforms well in the case of *in vivo* T_1 mapping as the relative errors remain below 2%.

5.6 Conclusions

Image reconstruction following the line-sharing method may exhibit FOV/2 ghost artefacts in the case of rapidly changing inversion recovery curves. SOS provides a degree of suppression of such spatial distortions and artefacts. Therefore, a phased-array processing method is employed to provide resilience to remove the possible ghost artefacts. Application of the phased-array ghost cancellation method to suppress artefacts in the line-shared images used for T_1 mapping was demonstrated experimentally with phantom imaging and *in vivo*.

5.7 References

1. Roemer PB, Edelstein WA, Hayes CE, Souza SP, Mueller OM. The NMR phased array. Magn Reson Med 1990;16:192–225.

2. Wright SM, Wald LL. Theory and application of array coils in MR spectroscopy. NMR in Biomedicine 1997;10:394–410.

3. Debbins JP, Felmlee JP, Riederer SJ. Phase alignment of multiple surface coil data for reduced bandwidth and reconstruction requirements. Magn Reson Med 1997;38:1003–1011.

4. Pruessmann KP, Weiger M, Scheidegger MB, Boesiger P. SENSE: sensitivity encoding for fast MRI. Magn Reson Med 1999;42:952–962.

5. Sodickson DK, Griswold MA, Jakob PM. SMASH imaging. Magn Reson Med 1999; Clin North Am 7(2):237–254.

6. Larsson EG, Erdogmus D, Yan R, Principe JC, Fitzsimmons JR. SNR-optimality of sum-of-squares reconstruction for phased-array magnetic resonance imaging. J Magn Reson 2003;163:121-123.

7. Walsh DO, Gmitro AF, Marcellin MW. Adaptive reconstruction of phased array MR imagery. Magn Reson Med 2000;43:682–690.

8. Kellman P, McVeigh ER. Phased array ghost elimination. NMR in Biomedicine 2006;19:352–361.

9. Verbout SM, Netishen CM, Novak LM. Polarimetric techniques for enhancing SAR imagery. Synthetic Aperture Radar SPIE 1992;1630.

10. Bydder M, Larkman DJ, Hajnal JV. Combination of signals from array coils using image-based estimation of coil sensitivity profiles. Magn Reson Med 2002;47:539–548.

Chapter 6
Outlook

The work described in this thesis constitutes a contribution to the trend of developing fast imaging methods for relaxation rate mapping. Extensions to rapidly traversing k-space for each time-point along the T_1 relaxation curve as well as rapid motion estimation techniques were developed in the work presented in this thesis. It was shown that acquisition time savings of up to 40% are achievable through line-sharing with a tolerable loss of around 3-5% in accuracy. The motion estimation algorithm presented here utilised the actual image data acquired and thus is not based on the explicit acquisition of additional data such as is the case with navigator-based techniques. Possible future developments for each method described in this thesis are given in the following.

6.1 Combining Rapid Acquisition Techniques and Rapid Motion Estimation Techniques

Reducing the number of time-points is one possible way to reduce acquisition time but it leads to a loss in the temporal resolution in the sampling of the T_1 relaxation curve. In order to achieve a higher temporal resolution, motion between time-points needs to be compensated. Despite the incorporation of rapid sampling schemes such as line-sharing and GRAPPA in T_1 relaxation rate mapping methods, motion remains a hindrance in the acquisition of artefact-free images along the T_1 relaxation curve. This leads to the second main topic of this thesis; how to rapidly determine in-plane motion estimation parameters. For the first time, a rapid method is introduced to estimate in-plane rotation based on the pseudo-polar Fourier transforms of the images, whereas in-plane translation is estimated by employing singular value decomposition of the phase correlation matrix of the images. Keyhole acquisition plays a central role in the rapid

imaging techniques proposed in this work. Since the rapid motion estimation strategies are also based on the images reconstructed from the keyhole data, the combination of rapid acquisition methods and motion estimation methods are ideally suited to each other. The results are of high relevance in the current motion compensation debate and conform well to the trends in the literature of calculating image-based motion parameters .

A strategy to combine the rapid sampling techniques with the rapid motion correction method can determine the future direction of research that may be based on this work. Although in ppm (parts per million) various sources of artefacts are field independent by definition, in absolute terms (Hertz) these are much bigger. Probably inter-scan and intra-scan strategies will have to be developed to counter the deleterious effects of motion artefacts. One possible strategy would be to employ rapid motion estimation techniques to adapt MR scan parameters in real-time.

In conclusion, the combined rapid acquisition and motion estimation approach offers a fast and reliable way to perform rapid relaxation rate mapping in a clinical environment but without image artefacts. This approach may prove critical for identification and tracking of changes in pathologies of the human brain such multiple sclerosis, hepatic encephalopathy, etc.

6.2 Extension to Rapid Acquisition Techniques

The line-sharing algorithm is well suited for use at field strengths above 3T since the T_1 relaxation rate decreases and hence the linear interpolation based line-sharing technique is expected to perform better, as explained in chapter 3. The proposed rapid k-space sampling schemes showed that combining line-sharing and GRAPPA is a win-win strategy that may facilitate even faster high-resolution imaging at high field strength.

6.3 Extension to Rapid Motion Estimation Techniques

In-plane rotation is estimated using the special patterns made by the navigator images in the pseudo-polar Fourier domain, which are effectively detected and analysed using the angular difference function (ADF). This function measures the difference between the images in the angular direction in the pseudo-polar Fourier domain. Through-plane motion remains a problem to solve as it affects the accuracy and precision of in-plane motion estimation using ADF. One possible approach to minimise such effects is to apply a low-pass filter to ADF before calculating the rotation angle.

Although parallel imaging is expected to perform better at higher field strength, inter-scan or intra-scan motion can degrade the reconstruction quality of images. Therefore, combining the motion estimation scheme with GRAPPA, for example, would be advantageous for higher field strengths.

Another possible extension of the rapid motion estimation method presented in this thesis is volume registration. Using the three-dimensional extension of the pseudo-polar Fourier transform and calculating the three-dimensional ADF, a rapid rotation estimation of MR volumes can be performed. Volume size can play an influential role in the development of a fast algorithm for the registration of rotated and translated MR volumes using the three-dimensional pseudo-polar Fourier transform, which accurately computes the Fourier transform of the registered MR volumes on a near-spherical three-dimensional domain without using interpolation. One possible procedure to calculate the motion parameters through volume registration is explained in the following. First, the rotational axis is estimated. Second, the rotational angle relative to the rotational axis is calculated followed by the translation parameter calculation. The axis of rotation is accurately recovered by the three-dimensional pseudo-polar Fourier transform using radial integration. The rotational angle can be computed by a three-dimensional extension of the angular difference function. Similarly, for translation estimation, an extension of the phase correlation method to three-dimensional data sets is possible. According to the Fourier shift theorem, the motion model for translation between three-dimensional volumes is represented as a rank-one tensor. The phase correlation between two MRI volumes is decomposed by using a high-order singular value decomposition

method to independently recover translation parameters along each dimension. Based on the performance of the algorithm in the case of two-dimensional MR images, the three-dimensional extension of the algorithm is expected to be accurate and robust to noise.

Contributions to Conferences, Workshops, and Research Reports Arising from this Work

The research work presented in this thesis gave rise to the following:

<u>Conferences :</u>

1. N. J. Shah, I. A. Gilani, H. Neeb, A. M. Oros-Peusquens, "Multi-Channel Line-Sharing for Rapid T_1 Mapping: Application to TAPIR" , Proc. ISMRM 16th International Conference, Toronto, May 2008.

2. I. A. Gilani, N. J. Shah, "Application of the Pseudo-Polar Fourier Transform for In-Plane Rotation Correction of MR Images", Proc. ISMRM 16th International Conference, Toronto, May 2008.

<u>Research Reports :</u>

3. "Simulation of Rapid MR Data Acquisition Scheme for Fast T_1 Mapping", Research Report to the Deutscher Akademischer Austausch Dienst (DAAD), August 2006, Germany.

4. "In-Plane Motion Estimation Strategies for MR Images", Research Report to the Deutscher Akademischer Austausch Dienst (DAAD), July 2007, Germany.

<u>Workshops :</u>

5. "Line-Sharing in TAPIR for Rapid T_1 Mapping", MRI in NRW Workshop, November 2007, Juelich, Germany.

6. "Fast T_1 Mapping, Echo Planar Imaging with Keyhole and Motion Correction", MRI Research Progress in Research Centre Juelich and University of La'Aquila, March 2007, Italy.